

Effects of confinement and conservation in nature's toolbox of pattern formation

Von der Universität Bayreuth
zur Erlangung des Grades eines
Doktors der Naturwissenschaften (Dr. rer. nat.)
genehmigte Abhandlung

von

Lisa Rapp

geboren in Pfullendorf

1. Gutachter: Prof. Dr. Walter Zimmermann
2. Gutachter: Prof. Dr. Markus Bär

Tag der Einreichung: 4. April 2019
Tag des Kolloquiums: 9. August 2019

Kurzzusammenfassung

Unter Musterbildung versteht man einen dynamischen Prozess, bei dem durch eine Instabilität des Ausgangszustandes selbstorganisiert räumliche oder zeitliche Strukturen entstehen. Die vorliegende Dissertation beschäftigt sich mit generischen Aspekten der Musterbildung und ihren Funktionen in biologischen, chemischen und aktiven Systemen. Die erste Hälfte der Arbeit konzentriert sich dabei auf verschiedene Auswirkungen räumlicher Beschränkung. In der zweiten Hälfte der Dissertation werden die Effekte von Erhaltungsgrößen thematisiert, die zu einem Nichtgleichgewichts-Entmischungsphänomen namens "aktive Phasenseparation" führen können.

Auf dem Themengebiet der räumlichen Beschränkungen wird zunächst gezeigt, wie man mit Hilfe einer räumlichen Kontrollparametervariation von super- zu subkritischen Werten endliche musterbildende Bereiche schaffen kann, ohne spezifische Randbedingungen annehmen zu müssen. Anhand eines prototypischen Reaktions-Diffusions-Modells, das einen Übergang zu periodischen Streifenmustern zeigt, lässt sich feststellen, dass die Steilheit der Kontrollparametervariation maßgeblich die Orientierung der Streifen beeinflusst. So findet sich ein Orientierungsübergang von senkrechten zu parallelen Streifen bezüglich des Randes, wenn die Kontrollparameterstufe hinreichend steil wird. Wir liefern generische Argumente auf der Basis von Funktionalbetrachtungen, um diesen Orientierungswechsel zu erklären.

Ein zweites Projekt beschäftigt sich mit den Auswirkungen starker räumlicher Einschränkung auf nichtlineare Wanderwellen. Anhand eines generischen Modells zeigen wir, dass Wanderwellen unweigerlich in stehende Wellen übergehen, wenn das System hinreichend klein wird. Reflexionseffekte am Rand übertreffen in diesem Fall den nichtlinearen Wettbewerb von links- und rechtslaufenden Wellen, der in ausgedehnten Systemen zur Auslöschung einer Wellenart führt und eine Überlagerung zu stehenden Wellen verhindert. Mit Hilfe einer linearen Stabilitätsanalyse ermitteln wir das so genannte Eckhausstabilitätsband der stehenden Wellen, das deren Anpassung an die Systemgröße zulässt. Übergänge zwischen stehenden Wellen mit verschiedener Knotenanzahl, sowie Übergänge zu Wanderwellen in Abhängigkeit der Systemgröße werden analytisch vorhergesagt und in numerischen Simulationen bestätigt. Die generischen Eigenschaften nichtlinearer Wellenmuster in stark eingeschränkten Systemen können Aspekte robuster Selbstorganisation in biologischen Systemen erklären, etwa Pol-zu-Pol-Oszillationen der Min-Proteine in *E. coli* Bakterien, die für die zuverlässige Zellteilung in der Zellmitte

verantwortlich sind.

Schließlich erarbeiten wir auch generische Aspekte von bevorzugter Polarität stationärer periodischer Lösungen in räumlich stark eingeschränkten Systemen. Diese liefern erste Erklärungsansätze für Beobachtungen in einem Modell für Protein-Clustering in Zellen. In diesem sammeln sich Proteine überwiegend in der Zellmitte an, obwohl eine Anhäufung am Rand des Systems ebenfalls mit Symmetrie und Randbedingungen des Systems vereinbar wäre. Durch die Analyse eines Minimalmodells können wir zeigen, dass starke räumliche Einschränkung in Kombination mit einer gebrochenen \pm -Symmetrie die generische Grundlage einer solchen Polaritäts-Bevorzugung ist.

Der zweite Themenkomplex der vorliegenden Dissertation beschäftigt sich mit der so genannten aktiven Phasenseparation – einem Entmischungsphänomen fernab des thermodynamischen Gleichgewichts. Wir führen ein auf Störungstheorie basiertes, systematisches Schema ein, das aktive Phasenseparation als neue generische Klasse der Musterbildung fern vom Gleichgewicht definiert. In einer Reihe von Publikationen wenden wir das Schema auf verschiedene Beispiele lebender und aktiver Materie an: Zellpolarisation, Ansammlungen chemotaktisch kommunizierender Zellen, sowie aktive Brownsche Teilchen. Mit unserer Vorgehensweise lassen sich die Kontinuums-Modelle dieser verschiedenen Beispiele in der Nähe des Einsatzpunktes der Phasenseparation auf eine gemeinsame universelle Gleichung reduzieren. Diese universelle Gleichung ist die Cahn-Hilliard-Gleichung. Sie wurde ursprünglich zur Beschreibung klassischer Phasenseparation, also der Entmischung zweier Substanzen zum Erreichen eines neuen thermodynamisches Gleichgewichtes, eingeführt. Mit dem Cahn-Hilliard-Modell als gemeinsamer Gleichung für den erhaltenen Ordnungsparameter können wir also erstmals einen systematischen Zusammenhang zwischen Entmischungsphänomenen im und fern vom Gleichgewicht herstellen. Eine Erweiterung unseres Ansatzes lässt auch die systematische Herleitung höherer Nichtlinearitäten zu. Die daraus resultierende erweiterte Cahn-Hilliard-Gleichung bildet Aspekte aktiver Phasenseparation bis weiter über ihren Einsatzpunkt hinaus ab. Eine erste Erforschung der Effekte, die jenseits der aktiven Phasenseparation auftreten können, zeigt einen sekundären Übergang von Phasenseparation zu räumlich periodischen Lösungen. Die Arbeiten auf diesem Themengebiet bilden die Grundlage für die weitere Erforschung dieser generischen Musterbildungsklasse mit erhaltenem Ordnungsparameter. Gleichzeitig eröffnen sich Einblicke in die Art und Weise wie die Natur Musterbildung als Werkzeug verwendet, um essentielle Funktionen zu erfüllen und die Maschinerie des Lebens zu erhalten.

Abstract

Pattern formation is a dynamic process in which instabilities of an initial state lead to the self-organized formation of spatial or temporal structures. In this thesis, we explore generic aspects of pattern formation and their function in biological, chemical and active systems. The first half of the thesis focuses on different effects of spatial confinement. The second half deals with conservation constraints and a resulting nonequilibrium demixing phenomenon called active phase separation.

In exploring the effects of confinement, we first show how spatial control parameter variations from super- to subcritical values create finite regions of pattern formation without imposing specific boundary conditions. Using a prototypical reaction-diffusion model with a transition to stripe patterns, we show that the steepness of these so-called control parameter drops significantly influences the stripe orientation. Increasing drop steepness triggers an orientational transition from perpendicular to parallel stripes. We are able to explain this orientational transition using fundamental principles of pattern formation theory.

A second project addresses the effects of strong spatial confinement on nonlinear wave patterns. Using a generic model, we show that traveling waves inevitably change into standing waves if the system becomes sufficiently short. In this case, reflexion effects at the boundaries exceed the nonlinear competition of counter-propagating waves that lead to the selection of a single wave type in extended systems. Using linear stability analysis, we calculate the so-called Eckhaus stability band of standing waves which allows them to adapt to different system lengths. We are also able to predict analytically and confirm in numerical simulations transitions between standing waves with different numbers of nodes, as well as transitions to traveling waves depending on the system length. These generic features of nonlinear waves in strongly confined systems shed light on aspects of robust self-organization in biological systems: Pole-to-pole oscillations of Min proteins in *E. coli* bacteria, for example, resemble boundary-induced one-node standing waves and are responsible for accurate cell division.

Finally, we establish generic aspects of polarity bias for spatially periodic patterns in strongly confined systems. These form the basis for an explanation of recent observations in a protein clustering model. In this model, proteins tend to cluster in the cell center even though protein aggregations near the cell boundary are equally compatible with the symmetry and the boundary conditions of the system. By analyzing an equiv-

alent minimal model, we show that the basis of this so-called polarity bias is strong spatial confinement in combination with a broken up-down-symmetry in the system.

The second part of the thesis deals with so-called active phase separation - a demixing phenomenon that take place far from thermodynamic equilibrium. We introduce a systematic perturbative scheme that defines active phase separation as a new class of nonequilibrium phase transitions. We apply this newly-developed scheme to several examples of living and active matter: cell polarization, chemotactic cell communities, as well as active Brownian particles. With our approach, the continuum models of these examples can be reduced to a universal equation near the onset of active phase separation. This universal equation is the Cahn-Hilliard equation. It was initially introduced to describe classic phase separation, i.e. the demixing of substances to reach a new thermodynamic equilibrium. With the Cahn-Hilliard model as the common equation for the conserved order parameter we can thus for the first time create a direct connection between demixing phenomena in and out of thermal equilibrium. By extending our perturbative approach, we can also include higher order nonlinearities. The resulting extended Cahn-Hilliard equation is able to reproduce aspects of active phase separation even farther from the onset of phase separation. In a first foray into effects occurring in the nonlinear regime beyond active phase separation, we found a secondary transition from phase separation to spatially periodic patterns. Our work on the topic of active phase separation are the basis for further research on this generic class of pattern formation with a conserved order parameter and gives us new exciting insights into the way nature uses the toolbox of pattern formation to fulfill essential functions and build the machinery of life.

Contents

Kurzzusammenfassung	I
Abstract	III
I. Extended abstract	1
1. Finite size effects on patterns	3
1.1. Self-organization in nature	3
1.2. Finite size effects	5
1.3. Patterns in finite domains without boundaries	5
1.4. Traveling waves in strong confinement	11
1.5. Polarity bias through strong confinement	15
2. Active phase separation	19
2.1. Active matter	19
2.2. Equilibrium phase separation	19
2.3. A universal approach to active phase separation	21
2.3.1. Introduction	21
2.3.2. Model systems	22
2.3.3. The Cahn-Hilliard model for active phase separation	24
2.3.4. The extended Cahn-Hilliard model	26
2.3.5. Behavior beyond active phase separation	28
2.3.6. Outlook	29
Bibliography	31
II. Publications	49
3. List of publications, preprints and drafts	51
4. Author's contributions	53
5. Attached publications	57
Pub1 - Pattern orientation in finite domains without boundaries	59

Pub2 - Size matters for nonlinear (protein) waves	67
Pub3 - Polarity bias in systems with broken up-down symmetry	79
Pub4 - Active phase separation: A universal approach	87
Pub5 - Universal aspects of collective behavior in chemotactic systems	97
Pub6 - Systematic extension of the Cahn-Hilliard model for motility-induced phase separation	109
Pub 7 - Spatially periodic patterns succeed active phase separation	121

Part I.

Extended abstract

1. Finite size effects on patterns

1.1. Self-organization in nature

The second law of thermodynamics states that any system strives towards a state of higher entropy, usually associated with a higher degree of disorder. In the 19th century, the so-called heat death theory built upon this idea, hypothesizing that the ultimate fate of the universe is a state of evenly distributed energy [1]. Clearly, this idea is in stark contrast to our everyday experience. Nature is full of remarkable examples of order and structure [2–4]. In fact, life itself is arguably the most striking form of order with every living creature made up of highly complex structures and precisely organized processes [5–8]. The important difference is that most systems in nature are not in and do not strive towards thermodynamic equilibrium. Instead, they are nonequilibrium systems constantly consuming energy - which gives rise to the organized structures we find all around us [9–11].

Examples of naturally occurring patterns are numerous [3, 4]: cloud streets [12, 13], patterns on fish skin [14–16], vegetation patterns in dry landscapes [17–22], thermal convection [23], nematic liquid crystals [24], nonlinear optical systems [25, 26], the wrinkled surface of the brain or our fingerprint [27, 28], the hexagonal cells of honeybee or wasp combs [29, 30], and sand ripples in the desert or on a beach [31, 32]. In two dimensions, possible spatial patterns include stripes or labyrinth-like structures, squares, hexagons or spot-like patterns [33, 34]. Oscillations can be viewed as patterns in time. Among them are chemical oscillators, often also called chemical clocks, such as the Belousov-Zhabotinsky reaction which periodically changes its color [35], or the circadian rhythms that govern biological life [36–38]. Combining both types of patterns gives rise to moving spatial patterns such as traveling waves. They can be found in systems ranging from binary fluid convection [39–42], electroconvection in liquid crystals [43] to (bio-)chemical reactions [44–47].

In nature, patterns often fulfill important functions: Animals use skin patterns for camouflage [48], patterns in the early embryo guide cell differentiation [49, 50], vegetation patterns allow for an optimized usage of scarce water resources in dry landscapes and thus prevent desertification [18, 21], and thermal convection generates increased heat transfer in temperature gradients [23].

Pattern formation as a research field in nonlinear physics first became popular in the 1970s with a series of experiments on Rayleigh-Bénard convection [33, 51, 52]. Rayleigh-

Bénard convection is often seen as a canonical example for pattern formation - both due to its experimental accessibility and the theoretical knowledge about the underlying hydrodynamic equations [33]. In the context of fluid convection in 1977, Swift and Hohenberg derived the equation that would later be named after them - the Swift-Hohenberg equation [53]. It later became one of the most popular minimal models for pattern formation and was used to study spatially periodic patterns far beyond the scope of fluid convection. This is very much in the spirit of pattern formation research which has finding and analyzing the generic system-spanning properties of patterns as one of its main objectives [33, 34]. As the many examples mentioned above show, patterns occur in a big variety of different systems. The details and specific mechanisms involved in all of these systems are certainly just as diverse as the systems in which they occur. The idea is to find the common features and the underlying basic principles of certain types of patterns regardless of the individual system-specific details.

One of the most powerful and often used tools to study patterns is the weakly nonlinear analysis via the amplitude equation formalism [33, 34]. The underlying conceptual idea is that even complicated pattern-forming systems can be reduced to the evolution equation of a single scalar field near the onset of pattern formation. It has been found, for example, that the slowly varying envelope $A(x, t)$ of spatially periodic patterns follows the so-called Ginzburg-Landau or Newell-Whitehead-Segel equation [33, 54–56] (first derived in the context of superconductivity and later for Rayleigh-Bénard convection):

$$\tau_0 \partial_t A = \varepsilon A + \xi_0^2 \partial_x^2 A - g |A|^2 A. \quad (1.1)$$

Interestingly, Eq. (1.1) can be written as $\tau_0 \partial_t A = -\delta \mathcal{F} / \delta A^*$, where

$$\mathcal{F} = \int dx \left(-\varepsilon |A|^2 + \xi_0^2 |\partial_x A|^2 + \frac{g}{2} |A|^4 \right) \quad (1.2)$$

behaves like a free energy potential [33]. The amplitude equation thus follows potential dynamics even though the original pattern-forming systems are usually dissipative. Minimal generic models, linear stability analysis, weakly nonlinear analysis, the amplitude equation formalism and considerations of the corresponding energy potentials are some of the pillars of pattern formation theory and widely used tools within this thesis [33, 34].

1.2. Finite size effects

Almost all patterns that occur in nature or any other experimental system emerge in confined areas or volumes. If the systems are large enough, an infinite system size or periodic boundary conditions can be assumed. This significantly simplifies mathematical approaches while in many cases still delivering good approximations of the observed patterns. In many other cases, however, finite size effects cannot be neglected. Boundaries are known to significantly influence pattern formation in finite systems. In one spatial dimension, boundaries lead to wavenumber selection, i.e. restrictions on the possible wavelengths of instabilities [33, 57–62]. As a result, confinement reduces the so-called Eckhaus band of stable spatially periodic patterns, for example. In strong spatial confinement, boundaries have also been found to influence the polarity of spatially periodic Turing patterns [63]. Wavenumber selection also occurs in systems with so-called “soft” boundaries [64–68]. In these systems, the control parameter, which triggers the transition from the homogeneous to a patterned state, is gradually ramped connecting a subcritical to a supercritical region. In two dimensions, boundaries break the symmetry in inherently isotropic systems. This can lead to orientational selection of stripe patterns. Thermal convection rolls, for example, align perpendicular to lateral boundaries [33, 69, 70]. Especially in the context of biological pattern formation, moving and/or curved boundaries mimicking the situation in living cells have been of interest and have shown to, among other things, profoundly influence the orientation and shape of stationary patterns [71–76]. In addition, boundaries also affect the dynamic behavior such as the time scale needed to reach stationary patterned states, or defect dynamics [70]. Traveling waves can be reflected at boundaries leading to intriguing spatiotemporal behavior [77, 78]. Finally, finite size effects can fundamentally change the types of patterns observed in the system, and influence the pattern onset, as well as transitions between different pattern types [79–82].

1.3. Patterns in finite domains without boundaries

Motivation and Background — As established previously in Chapter 1.2, boundaries can affect pattern formation in numerous significant ways. In some systems, boundaries are well-defined. However, we can imagine scenarios where this is not the case. In photosensitive chemical reactions such as the CDIMA reaction pattern formation can be controlled by illumination [83]. Spatially periodic patterns appear if the light intensity

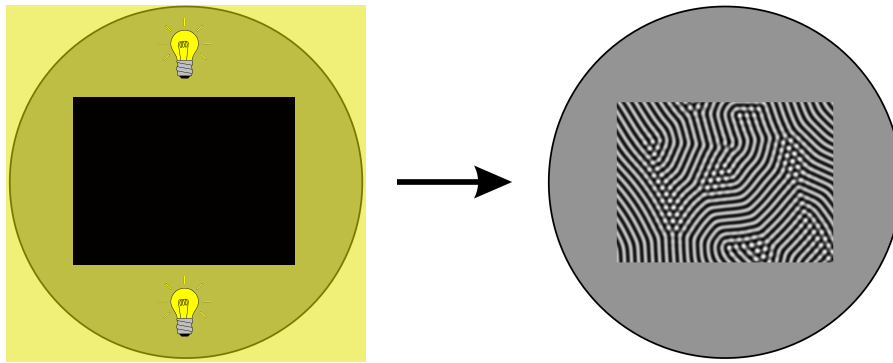


Fig. 1.1 – Principle idea of creating patterned subdomains with control parameter drops: The control parameter (in this example the light intensity) is only supercritical in some parts of the system. This restricts pattern formation to a finite subdomain without imposing specific boundary conditions.

is below a certain threshold, while the chemicals remain homogeneously mixed for high light intensities. Imagine now a scenario where only a part of the reaction cell is illuminated - or shaded in the example of the CDIMA reaction (see Fig. 1.1). This creates a pattern in a finite subdomain of the system without imposing any specific boundary conditions on the concentration fields involved in the pattern formation process.

A similar situation can be found in recent experiments with the pattern-forming Min protein system [84]. In this biochemical reaction stemming from E. Coli bacteria, Min proteins create wave patterns by binding to and detaching from the cell membrane in a coordinated fashion. In recent experiments, the pattern-forming Min protein reaction was restricted to membrane patches of designed geometry. These were created by micropatterning substrates with gold layers which prevent membrane formation. Since the biochemical Min reaction involves protein exchange between the membrane and the protein solution, this essentially restricts pattern formation to the membrane patches while no specific boundary conditions apply to the protein concentration in the solution

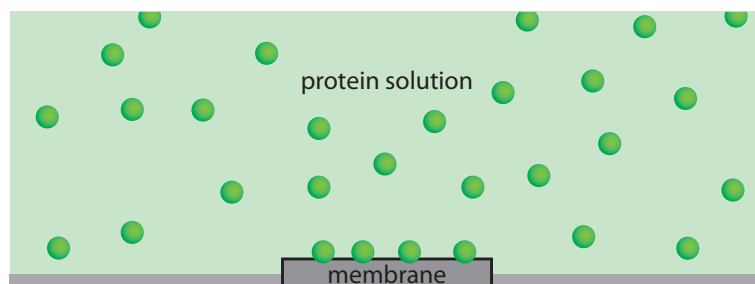


Fig. 1.2 – Schematic view of recent in vitro experiments with the Min protein system [84]. Pattern formation is restricted to membrane patches on the substrate.

above the membrane (see Fig. 1.2).

In [Pub1], we systematically analyzed the effects of these so-called control parameter drops on two-dimensional stripe patterns.

Model and Methods — In [Pub1], we analyzed the well-established Brusselator model as a prototype reaction-diffusion system with a transition to spatially periodic patterns (also known as Turing patterns) [85–87]. The evolution of the two concentration fields u and v in this model are described by

$$\partial_t u = \nabla^2 u + a - (b + 1)u + u^2 v, \quad (1.3a)$$

$$\partial_t v = D \nabla^2 v + bu - u^2 v, \quad (1.3b)$$

where a and D are constant parameters and b is the control parameter¹. Stripes² with a typical wavelength λ_c emerge if the control parameter exceeds the threshold b_c .

We model the control parameter drop in one dimension by spatially varying the control parameter in the following form:

$$\beta(x) := \beta_0 + \frac{M}{2} \left[\tanh\left(\frac{x - x_l}{\delta_x}\right) - \tanh\left(\frac{x - x_r}{\delta_x}\right) \right], \quad (1.4)$$

where β measures the distance from pattern onset, $b = b_c(1 + \beta)$, and δ_x is referred to as the drop width. For appropriate parameter choices, this creates a region of approximate size $L \approx x_r - x_l$ in which the control parameter is supercritical and pattern formation is enabled. This supercritical subregion is continuously connected to a subcritical control parameter range. The drop width δ_x controls the steepness of the transition from super- to subcritical control parameter values.

Main results — Since the Brusselator model itself is isotropic, stripes in this system do not a priori have a preferred orientation. Hence, in extended systems the pattern usually consists of domains of randomly oriented stripes (see Fig. 1.3a). Our simulations show that introducing a control parameter drop significantly influences stripe orientation. For shallow parameter drops (δ_x large), stripes favor a perpendicular orientation with respect to the domain boundary (Fig. 1.3b). Finite system size thus leads to an

¹In this model, the homogeneous basic solution (u_h, v_h) is a function of the control parameter b . This is actually an essential condition for the orientational selection by the control parameter drop. [Pub1] discusses this aspect in more detail.

²The Brusselator typically leads to hexagonal patterns directly above threshold. These can be avoided in favor of stripe patterns for suitable system parameter choices.

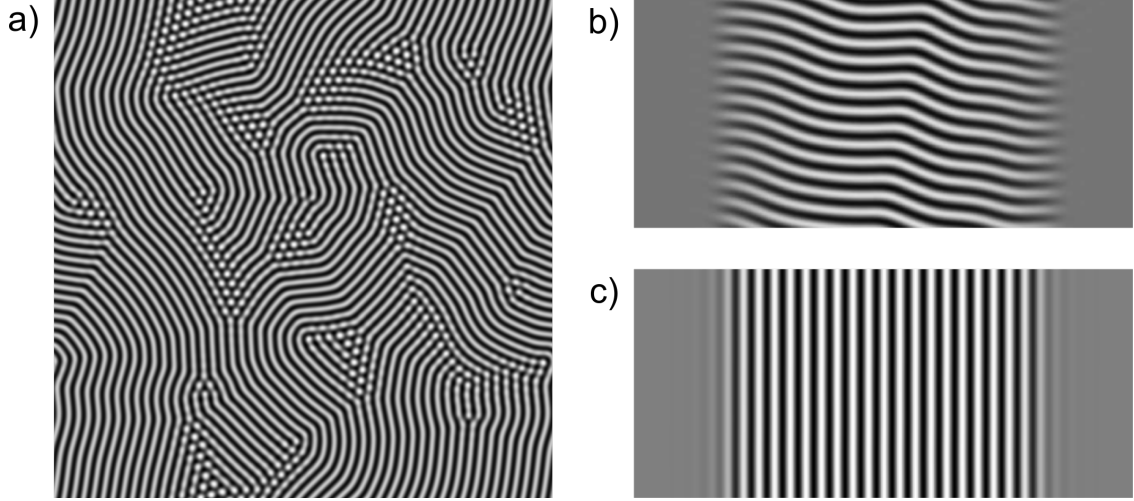


Fig. 1.3 – Control parameter drops cause orientation selection of stripe patterns. a) No preferred stripe orientation without control parameter drop. b) Stripes are perpendicular to the boundary for shallow control parameter drops ($\delta_x = 5\lambda_c$). c) Stripes are parallel for steep control parameter drops ($\delta_x = 0.5\lambda_c$). Figures b) and c) reproduced from [Pub1].

orientational selection for stripe patterns. Surprisingly, however, we found the preferred stripe orientation to change when the drop width is decreased. For steep control parameter drops, the preferred stripe orientation is parallel (Fig. 1.3c). We thus found an orientational transition from perpendicular to parallel stripes when the drop width is decreased, i.e. for steeper control parameter drops.

In [Pub1], we also present extended (semi-)analytical considerations to explain this phenomenon. A weakly nonlinear analysis as mentioned in Sec. 1.1 reduces the Brusselator model to a single amplitude equation for the slowly varying envelope $A(x, y, t)$ near the onset of pattern formation [33, 88]:

$$\partial_t A = \beta A + \mathcal{L}A - g|A|^2 A. \quad (1.5)$$

Depending on the stripe orientation, the linear operator \mathcal{L} is given by

$$\mathcal{L}_{\parallel} := \xi_0^2 \left(\partial_x - \frac{i}{2q_c} \partial_y^2 \right)^2, \quad (1.6a)$$

$$\mathcal{L}_{\perp} := \xi_0^2 \left(\partial_y - \frac{i}{2q_c} \partial_x^2 \right)^2, \quad (1.6b)$$

for parallel (i.e. pattern wavevector parallel to x -axis) or perpendicular stripes, respectively. In this equation, the control parameter β is assumed to be constant. The control

parameter drop, however, constitutes a spatial variation of the control parameter. When incorporating this into the amplitude equation, the separation of spatial scales between the envelope $A(x, t)$ and the underlying periodic pattern has to be considered. The control parameter drop includes both “slowly” varying parts in the constant regions of the step-like spatial variation, as well as “rapidly” varying local contributions near the control parameter drop. The slowly varying part is unproblematic, since it only results in small spatial changes of the control parameter β on the length scale of the envelope $A(x, t)$. A Fourier expansion of the rapidly varying part shows that it includes short-wavelength contributions $\propto \exp(inq_c x)$ (with $n = 1, 2, 3, \dots$). These contributions are in spatial resonance with the parallel stripes. Thus, the control parameter drop serves as a local resonant forcing - a short-scale resonant component localized around the rapidly varying section of the control parameter drop. Resonance effects have been investigated in the context of spatially periodic forcing in the past [89–93]. They cause additional resonant terms in the amplitude equation [89]. Thus, the amplitude equation for parallel stripes as given in Eq. (1.5) has to be expanded by, in our case, local resonant terms, while the amplitude equation for perpendicular stripes remains as given by Eq. (1.5). As a result, the transition from the homogeneous state to the stripe pattern is fundamentally different for parallel and perpendicular stripes if a control parameter drop is introduced. Since the resonant contributions are localized around the control parameter drop, their effect significantly depends on the drop width δ_x . Thus, the energy potential corresponding to the amplitude equation (cf. Sec. 1.1) also depends on δ_x . In the limit of large drop widths (shallow control parameter drops), the functional for parallel stripes is always higher than for perpendicular stripes. However, the functional for parallel stripes decreases significantly with decreasing drop width due to the local resonance effects. This allows for the orientational transition observed in simulations.

Outlook — The concept of control parameter drops can easily be implemented in experiments with photosensitive chemical reactions. Control parameter (in this case light intensity) variations using projection masks have already been studied in experiments before [94–96]. Experimentalists in these examples were interested in creating small-scale periodic variations of the control parameter to explore forcing mechanisms. The same experimental technique can of course be readily applied to create larger areas of illumination (or shading, respectively). Controlling the steepness of the control parameter drop may pose more difficult technical challenges. However, simple light intensity gradients have been successfully implemented in the past using neutral density filters

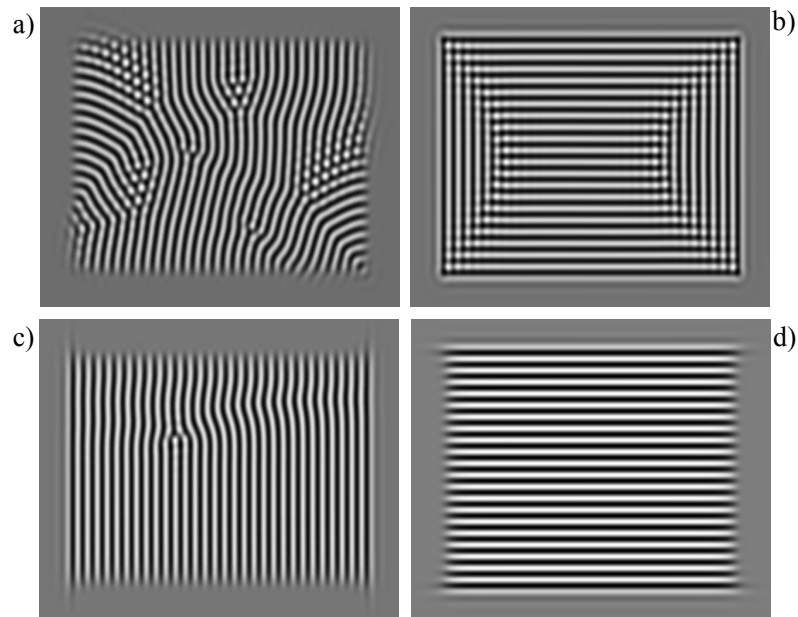


Fig. 1.4 – In two-dimensional systems, control parameter drops with tuned drop widths can be used to create highly controlled regular stripe patterns in rectangular domains. Reproduced from [Pub1].

(see e.g. [97]). Overcoming these technical challenges will grant scientists the possibility to create highly controlled patterns. This is especially the case in two-dimensional rectangular domains. Patterns become highly regular and defect-free when using suitable combinations of shallow and steep drops on the different edges of rectangular subdomains (see Fig. 1.4).

As mentioned in the introductory section above, experiments with the Min protein system on functional membrane patches are another strong candidate for further experimental exploration of control parameter drops [84]. The experiments by Schweizer et al showed that traveling protein waves orient perpendicular to the domain boundary. We could shed light on these observations by expanding our theoretical analysis to the effect of control parameter drops on two-dimensional traveling wave systems. More recent experiments also opened up the possibility for optical control of the Min system [98]. Very similar to the experiments with other photosensitive chemical reactions mentioned above, this would offer more flexibility in creating control parameter drops in the Min system.

1.4. Traveling waves in strong confinement

Motivation and Background — In recent years, the Min protein system has piqued the interest of researchers as a fascinating example of pattern formation in biology [99–101]. Due to its critical role in the life cycle of *E. coli* bacteria, a lot of effort has been put into understanding the underlying mechanisms and intricacies of this biochemical system. Overall, the system consists of the three proteins MinC, MinD and MinE [102]. MinD and MinE form the basis of a complex reaction-diffusion mechanism that gives rise to self-organized protein waves through coordinated binding to and detachment from the cell membrane. In the rod-like *E. coli* cell, the protein wave oscillates between the two cell poles [103]. These pole-to-pole oscillations essentially inhibit formation of the cell division site anywhere but in the center of the cell. This ensures the division into two daughter cells of roughly equal size with an astonishing precision [99].

In ground-breaking experimental work [47], the group of Petra Schwillle was first able to recreate the Min protein waves outside of the living cell. These *in vitro* experiments showed that on extended membranes, the Min system forms traveling waves with a distinct wavelength. This is in seeming contradiction to the observations of pole-to-pole oscillations in living *E. coli*.

Answering the questions raised by the Schwillle experiments is complicated by the fact that the exact biochemical reaction mechanisms behind the Min system are still a subject of discussion [99, 104–109]. The many potential players involved in the chemical reaction – MinD and MinE in both their membrane-bound and cytosolic form, as well as MinDE protein complexes – add another layer of complexity to the problem. Therefore, different mathematical models for the Min system have been proposed and extensively discussed in the past [47, 84, 106, 110, 111].

In [Pub2], we shed light on parts of these discussions by taking a more generic approach to the topic. In the living *E. coli* bacterium, the Min protein system is constricted to the small confined space of the cell volume. We therefore analyze the influence of strong spatial confinement on traveling wave patterns. We then show how these generic aspects of pattern formation can be applied to explain phenomena observed in the Min system.

Models and Methods — The complex Swift-Hohenberg (CSH) model is a minimal model for systems with a transition to traveling waves [112, 113]:

$$\partial_t u(x, t) = (\varepsilon + ia)u - \xi_0^2(1 + ib)(q_0^2 + \partial_x^2)^2 u + if\partial_x^2 u - \gamma(1 + ic)|u|^2 u. \quad (1.7)$$

Note that $u(x, t)$ is a complex field in this case. If the control parameter ε is larger than the critical value $\varepsilon_c = 0$, the system shows traveling waves with a distinct preferred wavelength $\lambda_0 = 2\pi/q_0$ in extended systems. We analyze the model in finite systems of length L assuming no-flux boundary conditions: $\partial_x u|_{x=0} = \partial_x u|_{x=L} = 0$. We are specifically interested in very strong confinement, i.e. in short systems with typical lengths in the order of the pattern wavelength.

[Pub2] includes both numerical simulations of Eq. (1.7), as well as linear stability analysis of nonlinear solutions. The latter involves solving linear differential equations with periodic coefficients. This can be done via a Fourier-type separation ansatz. Note, however, that to account for the no-flux boundary conditions, the Fourier series may only include cosine contributions. The resulting Eigenvalue problem can be solved numerically using standard linear algebra packages.

As a proof of principle, we also compared the generic results gained from the CSH model to two more specific examples of systems with traveling waves: an extended Brusselator model as a representative of a typical reaction-diffusion system with traveling waves [114], and one of the proposed models for the Min protein system [47].

Main results — In large extended systems the CSH model typically shows single traveling wave solutions moving in one direction [112]. In theory, due to the symmetry of the system, both left- and right-moving traveling waves are possible. Due to nonlinear interactions of the waves, however, one type of wave is suppressed. These observations are still true for moderately small finite systems (e.g. $L = 3\lambda_0$, see Fig. 1.5a, top). However, waves are also reflected at system boundaries. These reflection effects become more pronounced when the system length is further decreased. Beyond a critical system length, simulations show a transition from traveling to standing waves (Fig. 1.5a, middle and bottom). Depending on the system length, these standing waves can have different numbers of nodes.

We complemented these observations in numerical simulations with analytical calculations by studying the linear stability of standing wave solutions. Standing waves in Eq. (1.7) can be approximated by

$$u(x, t) = 2F e^{-i\Omega t} \cos(qx), \quad (1.8)$$

where F and Ω can be calculated from the system parameters and the wavenumber q depends on the system length L via $q = n\pi/L$ (where $n = 1, 2, 3, \dots$). We found

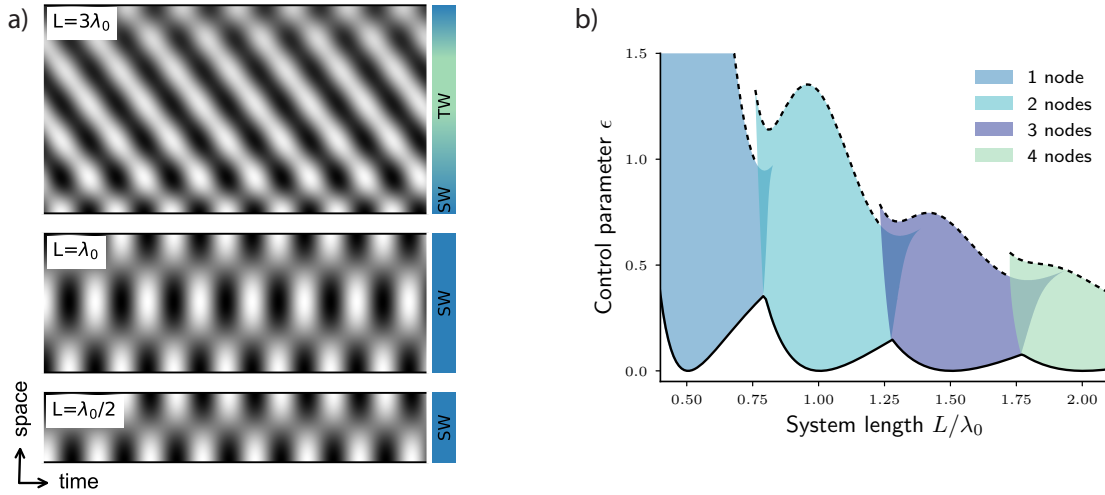


Fig. 1.5 – Effect of strong confinement on traveling wave patterns. a) Traveling waves (top) change into standing waves (middle and bottom) if the system length L is decreased. b) Linear stability of standing waves as a function of system length L and control parameter ε . Reproduced from [Pub2], published under CC-BY.

that standing waves with a certain number of nodes occupy a region of stability that depends mainly on the system length L and the control parameter ε (see Fig. 1.5b). Several generic features of nonlinear standing waves in strong confinement can be deduced from the results of the linear stability analysis: First, standing waves are able to adapt to the system length to a certain degree. This is a direct parallel to the well-known Eckhaus stability of periodic patterns, according to which stationary stripe patterns or traveling waves with wavenumbers from within the so-called Eckhaus band are stable above onset [33, 115–117]. Standing waves are stable within a large range of control parameter values if the wavelength of the standing wave corresponds to the preferred wavelength λ_0 . The stability region for standing waves with two nodes, for example, is thus centered around $L = \lambda_0$. However, the standing waves are able to adapt to deviations of this “optimal” system length, resulting in extensive regions of stability in the L - ε -plane (cf. the shaded regions in Fig. 1.5b). Second, the stability regions of standing waves with different numbers of nodes partially overlap. This gives rise to bistability of standing wave solutions. For parameters in this bistable region, two different solutions are thus simultaneously stable and the solution depends on the initial conditions. Third, transitions between different types of patterns are possible: If the control parameter ε exceeds a certain threshold, standing waves eventually transition to traveling waves. This is in agreement with the observations from simulations (Fig. 1.5a). Transitions between different types of patterns are another possibility to

adapt to system length variations. If the system length is increased, standing waves will first increase their number of nodes, before eventually changing into traveling wave patterns. For the CSH model, this transition from standing to traveling waves when either the system length or control parameter is increased is in the form of a supercritical bifurcation.

The results presented in [Pub2] are very robust. First, they do not significantly depend on any of the other system parameters in Eq. (1.7)³. Variations of other system parameters slightly change the exact shape of the stability regions shown in Fig. 1.5b. However, this does not change the qualitative picture described above. The transition from traveling to standing waves in sufficiently short systems is also not sensitive to the boundary conditions. Fixed boundaries ($u|_{x=0} = u|_{x=L} = 0$), for instance, only change the positioning of the standing wave nodes within the system. Finally, the qualitative results are also not system-specific. Comparisons to simulations of the so-called extended Brusselator [114] and one of the proposed models for the Min system [47] confirm the results obtained from the generic CSH model.

Outlook — With respect to the Min system, we hope that our research contributes to the ongoing discussions about the underlying biochemical mechanisms behind the Min protein waves. Our research explains the seemingly contradictory behavior of Min waves on extended membranes and in living bacteria: The nonlinear traveling Min waves inevitably change into standing waves if they are in the strong confinement of the cell body. Min traveling waves in vitro and pole-to-pole oscillations in vivo thus do not result from fundamentally different instability mechanisms. Since they result from generic features of nonlinear waves, they should be reproduced by any mathematical model of the Min system regardless of system details. Other results from [Pub2] can be qualitatively transferred to observations in the Min system as well: Pole-to-pole oscillations, for example, are robust even as the individual *E. coli* cells vary in length [103]. In fact, they need to be maintained even as the cell almost doubles in length prior to cell division. This corresponds to the Eckhaus stability range and resulting length adaptability of nonlinear standing waves. In experiments with elongated *E. coli* cells, standing waves with multiple nodes or even traveling waves have been found, as well as transitions and multistability between these different types of patterns [103, 107, 118, 119].

³A notable exception are parameter combinations in the Benjamin-Feir-unstable regime where traveling waves are convectively unstable and spatiotemporally chaotic states are possible [112].

An interesting next step would be an extension to two (or ultimately three) dimensions. The Min system has recently been investigated in controlled geometries by using shaped living bacteria [119, 120], two-dimensional membrane compartments [121] or three-dimensional confined micro chambers [122]. In many cases, our one-dimensional results can be qualitatively applied to explain the pattern types and orientations observed in these experiments. On rectangular domains, for example, standing waves seem to prefer orientations resulting in wavelengths closest to the intrinsic wavelength λ_0 . A second spatial dimension, however, offers the possibility of additional instabilities (e.g. zig zag instabilities) that could qualitatively change the picture [33, 112]. Another path of inquiry is to explore systems with subcritical bifurcations to traveling waves. This opens up a wealth of other dynamic solutions such as fronts and pulses [123].

1.5. Polarity bias through strong confinement

Motivation and Background — In a recent publication [124], Murray and Sourjik investigated the positioning of protein clusters inside cells. They present a simple three-component reaction-diffusion model for protein clustering on a membrane. Their study shows that in short confined systems (with no-flux boundary conditions), the proteins cluster to form a single concentration peak. In the vast majority of cases, this concentration peak is positioned in the center of the system with only few exceptions where the highest concentrations could be found near the system boundaries. Murray and Sourjik were able to explain aspects of this self-positioning within the scope of their specific model. In [Pub3], we approach the same question from a pattern formation point of view in order to investigate the possible generic aspects of protein-positioning.

Models and Methods — The model introduced in [124] has three distinctive characteristics: First, the system undergoes a transition to spatially periodic patterns (finite k-instability) when the total molecule concentration exceeds a critical threshold. Second, the up-down-symmetry in the system is broken resulting in solutions with pronounced asymmetric peaks as opposed to simple harmonic cosine-like solutions. Third, the total number of molecules in the system is conserved. A minimal model incorporating these three characteristics is the conserved Swift-Hohenberg model [125–128]:

$$\partial_t u(x, t) = -\partial_x^2 \left[\varepsilon u - (q_0^2 + \partial_x^2)^2 u + \alpha u^2 - u^3 \right]. \quad (1.9)$$

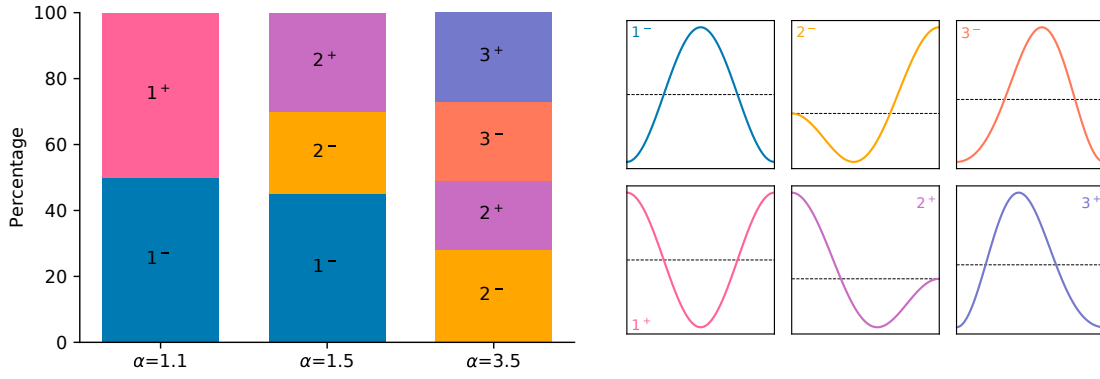


Fig. 1.6 – Solution types and rate of occurrence in simulations of the conserved SH equation, Eq. (1.9), in small confined systems ($L = \lambda_0$).

We assume small confined systems with no-flux boundary conditions and system lengths which are multiples of the preferred pattern wavelength: $L = n\lambda_c = n2\pi/q_0$. Linear stability analysis in these finite systems with no-flux boundaries requires the same methods as described in Sec. 1.4.

Main results — The symmetry-breaking parameter α significantly influences the types of solutions found in simulations of Eq. (1.9) in very small systems ($L = \lambda_0 = 2\pi/q_0$). Figure 1.6 is an overview of the typical concentration profiles found in simulations for different values of α . In general, solutions become more and more complex, i.e. are composed of more contributing Fourier modes, with increasing α . Of the different solution types, the 1^\pm -type is most closely related to the kinds of solutions found in the Murray/Sourjik protein clustering model. The solution with negative polarity, 1^- , has a single concentration peak located in the system center, while the positive polarity indicates highest concentrations near the boundaries. Simulation results reveal that for moderate values of the symmetry-breaking parameter ($\alpha = 1.1$), both of these solutions are equally likely to be found starting from random initial conditions. If α is increased to 1.5, however, the solution 1^+ vanishes. Thus, in this parameter region, there is a polarity bias towards the 1^- solution.

Semi-analytical calculations confirm this polarity bias in very small systems. The simplest approximate solution in the system is the dominating intrinsic mode q_0 with a small contribution of the higher harmonic $2q_0$ which is excited by the broken up-down symmetry:

$$u(x) = A \cos(q_0 x) + B \cos(2q_0 x). \quad (1.10)$$

Plugging this ansatz into Eq. (1.9) and projecting onto the two Fourier modes results in a coupled system of equations for the amplitudes A and B . The two different real-valued solutions, $[A, B]$ and $[-A, B]$ (where $A > B > 0$), suggest two solution types of different polarity: u_+ and u_- , respectively. u_+ is the solution with maxima at the system boundaries, while u_- suggests a peak in the center of the system. Due to the broken up-down symmetry, the linear stability of these solutions depends on the polarity of the solution. Our analysis shows that in very small systems ($L = \lambda_0$) depending on the symmetry-breaking parameter α , the solution with negative polarity can be stable, while the solution u_+ is already unstable. Thus, polarity bias occurs in a specific range of α . Polarity bias, however, also depends on the system length. The polarity bias vanishes if the system length is doubled to $L = 2\lambda_0$. In this case, both solutions u_{\pm} become simultaneously unstable at a critical value α_c . The linear stability of solutions in finite systems depends on the system length, since only perturbations with discrete wavenumbers $q = n\pi/L$ (where $n = 1, 2, 3, \dots$) fulfill the no-flux boundary conditions. Larger system sizes thus allow for more perturbative modes to be unstable and especially reduce the smallest possible wavenumber π/L of perturbations. In short, the polarity bias in the case $L = \lambda_0$ originates from the stabilization of the solution with negative polarity by the small system size even as the solution with positive polarity is already unstable.

Further considerations in [Pub3] show that conservation actually does not have an impact on the polarity bias. Polarity bias also appears in the classic Swift-Hohenberg model with an unconserved order parameter $u(x, t)$ [33, 53]:

$$\partial_t u = \varepsilon u - (q_0^2 + \partial_x^2)^2 u + \alpha u^2 - u^3. \quad (1.11)$$

In summary, the generic basis of polarity bias is the stabilizing effect of strong spatial confinement which affects solutions differently depending on their polarity due to the broken up-down symmetry.

Outlook — The results presented in [Pub3] are a first step towards understanding some of the observations in the cell clustering model [124]. However, further analysis is needed to get a clear picture of the polarity bias. Our simulations of the CSH model show, for example, a variety of different solution types - especially for strongly broken up-down symmetry (cf. Fig. 1.6). These other solutions do not exhibit a concentration peak in the system center and would thus not account for positioning of protein clusters

in the cell center. Thus, additional mechanisms seem to play a role in the protein model to avoid the asymmetric solutions found in the CSH model. Additionally, the protein clustering model shows polarity bias even in larger systems with multiple concentration peaks, while the polarity bias in our model vanishes if the system size is increased. Getting answers to some of these questions is a great starting point for further fruitful collaboration at the interface of pattern formation and biology.

2. Active phase separation

2.1. Active matter

Active matter has emerged as an exciting new research field in recent years [129–131]. Active matter systems consist of large numbers of components which locally consume energy and transform it into mechanical work, usually movement. This makes active matter an inherently nonequilibrium system. Interactions between the individual active components give rise to complex collective behavior such as flocking or clustering, oscillations and waves, order-disorder transitions and pattern formation [130, 132–136]. Prominent examples of active matter in nature are animal aggregations such as flocks of birds or schools of fish [137–139]. On a smaller scale, bacterial suspensions or colonies [140–143] or the cytoskeleton of living cells [144] can show active behavior. The most common example of synthetic active matter are suspensions of self-propelled colloids or nanoparticles. A variety of different techniques and mechanisms have been used to create these active particles [145, 146]. In many cases, propulsion is achieved by using phoretic forces due to gradients which can be - among others - chemical, electrostatic or thermal in nature [147]. Particles become self-propelled by creating their own local phoretic gradient in combination with asymmetric properties that determine the direction of motion [148]. Janus particles are often used in this context [149]. Particles can also become active by an external driving mechanism such as electric or magnetic fields or vibrating plates [150–152]. Other active matter systems studied in the lab are suspensions of microtubules and molecular motors which form so-called active nematics [153, 154], or on a macroscopic scale even systems of robots [155].

2.2. Equilibrium phase separation

Phase separation describes the thermodynamic process in which a homogeneous mixture separates into two coexisting phases [156–159]. One of the early examples where this phenomenon has been observed are binary alloys [160]. Other examples include binary fluid mixtures such as water and oil [161, 162] or polymer blends [163]. In all of these examples, phase separation is initiated by a temperature quench, usually to a lower temperature, which renders the homogeneous mixed state thermodynamically unstable. Once the distinct phases have started to form, the domains continuously grow in size in order to reduce the interfacial energy until the system has reached the new equilibrium

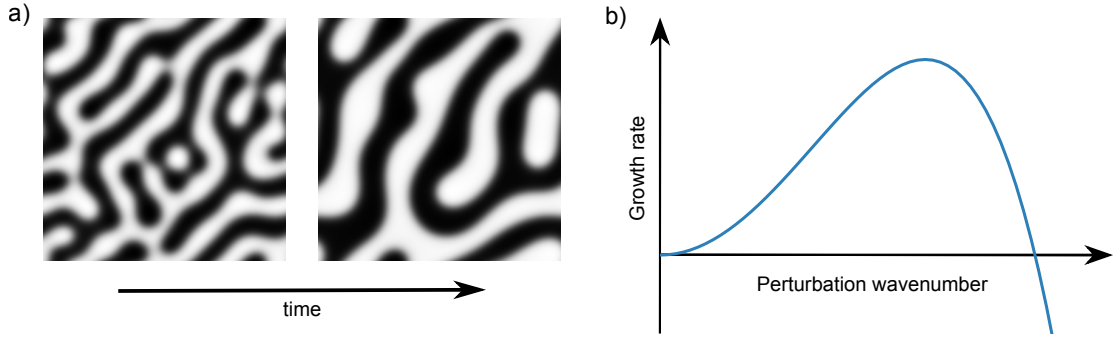


Fig. 2.1 – a) Typical coarsening behavior during phase separation processes. b) Characteristic growth rate of perturbations in systems showing phase separation.

state. This so-called coarsening process (see Fig. 2.1a) of increasing characteristic length scales over time often follows characteristic scaling laws [156].

The continuum description of phase separation dynamics is the so-called Cahn-Hilliard equation for the order parameter field $\psi(\mathbf{x}, t)$ [156, 164],

$$\partial_t \psi = -\nabla^2 [\nabla^2 \psi - V'(\psi)], \quad (2.1)$$

which is derived from a Ginzburg-Landau free energy functional via

$$\partial_t \psi = \nabla^2 \frac{\delta F}{\delta \psi}. \quad (2.2)$$

In this energy functional, $V(\psi)$ is a double-well potential representing the two equilibrium phases, while the other contribution accounts for the interface energy. The homogeneous state $\psi = 0$ in Eq. (2.1) is unstable towards perturbations with the typical growthrate dispersion relation as given in Fig. 2.1b. Note that there is a finite fastest-growing mode while the range of unstable perturbation wavenumbers extends down to $q \rightarrow 0$. This is the typical growth rate behavior for long-wavelength instabilities⁴. Note that the neutral growth rate at $q = 0$ indicates conservation of the order parameter field.

Recently, biologists have become increasingly interested in phase separation as a means to understand structural organization within the cell [165–168]. In this context, phase separation is also often referred to as dynamic compartmentalization. In these seminal works, the well-known concepts from equilibrium phase separation as described above

⁴In contrast, finite wavelength-instabilities as they are typical for Turing patterns, for instance, have a range of unstable modes at finite wavenumbers while long wavelength modes are damped.

have been the basis to tackle issues of self-organization in cell biology. It is important to note, however, that cells as living matter operate far from thermal equilibrium. It is thus not inherently clear whether the principles of equilibrium phase separation should apply to the conditions of living cells as well.

2.3. A universal approach to active phase separation

2.3.1. Introduction

Many of the active matter systems introduced in Sec. 2.1 show collective behavior such as clustering. On its face, the clustering in active matter systems is very reminiscent of equilibrium phase separation described in Sec. 2.2: In both cases, a homogeneous mixture separates into two distinct phases. In the clustering examples, the two phases are usually a dense fluid-like phase and a dilute gas-like phase. An important distinction though is that systems which undergo classic phase separation are only temporally driven out of thermal equilibrium and strive towards a new equilibrium state. In contrast, active systems that show clustering such as chemotactically communicating cells or active colloids are inherently, permanently far from thermal equilibrium. Cell polarization is another example of a nonequilibrium phenomenon that closely resembles classic equilibrium phase separation. In contrast to the clustering examples above, there are usually no active particles involved. Instead, aggregations of molecules in cells are achieved by chemical reactions inside the living cell – an environment far from thermal equilibrium.

In [Pub4]-[Pub7], we present seminal work on the phenomenon of active phase separation, i.e. phase separation processes in nonequilibrium systems. We establish active phase separation as a new class of nonequilibrium phase transitions. Our approach for this is a parallel to the amplitude equation formalism for spatially periodic patterns in nonequilibrium systems (cf. Sec. 1.1). This allows us to derive the universal model equation representing the generic properties of active phase separation and also indicate the connection to equilibrium phase separation. We present different examples from active and living matter which show active phase separation, and also take a first look at nonequilibrium phenomena occurring beyond the initial phase separation process.

2.3.2. Model systems

Throughout [Pub4]-[Pub6], we use a variety of model systems as examples for active phase separation. Among them, cell polarization refers to a broken spatial symmetry with respect to the morphology or the biochemical components of a cell [169–173]. The associated definition of a unique axis within the cell is the basis of important cell biological functions such as asymmetric cell division, cell differentiation, tissue formation, morphogenesis, or cell migration. In [Pub4], we examine a minimal model for cell polarization. The model assumes a single molecule species that exists in a cytosolic form or can be bound to a membrane, represented by concentration fields $u(x, t)$ and $v(x, t)$, respectively. Their dynamics are governed by reaction-diffusion equations given by

$$\partial_t u = D_u \partial_x^2 u + f(u, v), \quad (2.3a)$$

$$\partial_t v = D_v \partial_x^2 v - f(u, v), \quad (2.3b)$$

where $f(u, v)$ represents the nonlinear membrane-cytosol exchange. We choose

$$f(u, v) = -bu + (u + v)^2 - (u + v)^3, \quad (2.4)$$

thereby essentially using a simplified version of other established cell polarization models based on the reaction-diffusion mechanism [174]. The form of Eqs. (2.3) accounts for the fact that no molecules are produced or destroyed during the cell polarization process. Thus, the total amount of molecules $u + v$ in the system is conserved.

The second example analyzed in [Pub4] are chemotactic cell communities. Chemotaxis is the directed motion of cells along a chemical gradient [175, 176]. Chemotaxis plays an essential role in many aspects of biological life: Sperm cells swim towards chemical signals emitted from the egg, single organisms use chemotaxis to detect food sources, leukocytes in the body move towards sources of inflammation and the slime mold *Dictyostelium discoideum* relies on chemotactic signaling to form multicellular fruiting bodies in conditions of starvation. The latter example of slime mold aggregation was mathematically modeled by Keller and Segel [177, 178]. The resulting Keller-Segel model even today remains one of the cornerstone theoretical models for cell aggregation via chemotaxis. In [Pub4], we analyze a variant of the classic Keller-Segel model for

the cell density $\rho(x, t)$ and the signal concentration $c(x, t)$ [179]:

$$\partial_t \rho = \partial_x^2 \rho - s \partial_x \left(\frac{\rho}{1 + \alpha \rho} \partial_x c \right), \quad (2.5a)$$

$$\partial_t c = D_c \partial_x^2 c + \rho - c. \quad (2.5b)$$

The additional parameter α accounts for a density-dependent chemotactic sensitivity. For $\alpha = 0$, the set of equations reduces to the classic Keller-Segel model.

In [Pub5], we analyzed a different variant of the Keller-Segel model, given by

$$\partial_t \rho = \nabla^2 \rho - s \nabla \cdot \left(\frac{\rho}{(1 + \beta c)^2} \nabla c \right), \quad (2.6a)$$

$$\partial_t c = D_c \nabla^2 c + s \kappa \nabla \cdot (\rho \nabla c) + \frac{\rho}{1 + \gamma \rho} - c. \quad (2.6b)$$

This generalized, extended version includes several variations of the classic Keller-Segel model which account for different additional aspects of cell clustering: signal-dependent chemotactic sensitivity ($\beta \neq 0$) [179, 180], saturation of signal production for high cell densities ($\gamma \neq 0$) [179], as well as anisotropic production of the chemical signal ($\kappa \neq 0$) [181].

In [Pub6] we concentrate on the example of motility-induced phase separation (MIPS). MIPS describes the collective behavior of self-propelled particles with a density-dependent swimming speed which separate into a denser liquid-like phase and a dilute gas-like phase [182–187]. We analyzed a mean-field description for a suspension of active Brownian particles introduced by Speck et al [188, 189]:

$$\partial_t \rho = -\nabla \cdot [v(\rho) \mathbf{p} - D_e \nabla \rho], \quad (2.7a)$$

$$\partial_t \mathbf{p} = -\frac{1}{2} \nabla (v(\rho) \rho) + D_e \nabla^2 \mathbf{p} - \mathbf{p}, \quad (2.7b)$$

where $\rho(x, t)$ is the local particle density and $\mathbf{p}(x, t)$ the polarization (corresponding to the orientational order parameter of the particles). $v(\rho)$ is the density-dependent swimming speed given by

$$v(\rho) = v_0 - \rho \zeta + \lambda^2 \nabla^2 \rho, \quad (2.8)$$

with an additional non-local contribution for $\lambda \neq 0$ [190].

All these models have a number of characteristic similarities: As mentioned before, all of these systems are far from thermal equilibrium. They either involve actively moving particles or - in the case of cell polarization - take place in an inherently nonequilibrium

environment. Second, as described in Sec. 2.3.1, they all show behavior that is very reminiscent of equilibrium phase separation: Self-propelled particles or chemotactic cells aggregate to form dense clusters embedded in a dilute low-concentration phase. In polarized cells, molecules separate spatially to create regions of higher and lower concentration. Third, all of these examples include some kind of conservation constraint: the numbers of cells, active particles or molecules within a cell are conserved on the time scale of the phase separation. Finally, in each example a homogeneously mixed state is linearly unstable towards a spatially inhomogeneous state. The growth rate behavior of perturbations has the characteristic form of a long-wavelength instability as known from classic phase separation (cf. Fig. 2.1b).

2.3.3. The Cahn-Hilliard model for active phase separation

In [Pub4], we first introduce our concept of *Active Phase Separation*. We use this term to describe a new class of nonequilibrium phase transitions. This class consists of nonequilibrium demixing phenomena with certain characteristic generic properties. Our research published in [Pub4] reveals that these generic features are manifested in the existence of a universal model equation which describes active phase separation near onset. We show that this equation is the Cahn-Hilliard (CH) equation:

$$\partial_t u = -\partial_x^2 [\alpha_1 \varepsilon u + \alpha_2 \partial_x^2 u - \alpha_3 u^2 - \alpha_4 u^3]. \quad (2.9)$$

This equation is the same CH model which was initially introduced to describe demixing processes at thermal equilibrium (cf. Eq. (2.1) in Sec. 2.2). Our research shows, however, that it is also the leading order description of active phase separation in nonequilibrium systems. In addition to establishing the CH model as the universal equation for active phase separation near onset, our research thus also creates a fundamental link between demixing phenomena in and far from thermal equilibrium. Note that the CH equation, Eq. (2.9), can be derived from a free energy potential (see Sec. 2.2). Thus, the active phase separation behavior near onset follows potential dynamics even though the original mean-field models from which the CH model was derived are dissipative systems. While this may seem a surprising result, it is a well-known parallel to the amplitude equation of spatially periodic stripes (see Sec. 1.1).

In [Pub4], we introduce the systematic perturbative scheme that allows us to derive the CH equation directly from the mean-field models of active phase separation systems. This approach is similar to the derivation of the Ginzburg-Landau equation as the

evolution equation for the envelope of stationary periodic patterns [33, 34] (see Sec. 1.1). It involves a rescaling of space and time by the introduction of a new spatial scale $X = \sqrt{\varepsilon}x$ and two new time scales $T_3 = \varepsilon^{3/2}t$ and $T = \varepsilon^2t$, yielding the operator replacements

$$\partial_x \rightarrow \sqrt{\varepsilon}\partial_X \quad \text{and} \quad \partial_t \rightarrow \varepsilon^{3/2}\partial_{T_3} + \varepsilon^2\partial_T. \quad (2.10)$$

ε denotes the distance of the control parameter from its critical value, i.e. the value where the spatially homogeneous state becomes unstable and the phase separation process sets in. The growth of the instabilities is assumed to be saturated by cubic nonlinearities. This suggests an expansion of the involved fields in orders of $\sqrt{\varepsilon}$, e.g.

$$u = \sqrt{\varepsilon}u_1 + \varepsilon u_2 + \varepsilon^{3/2}u_3 + \dots \quad (2.11)$$

Sorting with respect to the different orders of ε leads to a set of hierarchical differential equations. Applying the Fredholm theorem then gives rise to solvability conditions for the contributions to the fields at different orders (u_i in the example above). At leading order, this results in the CH equation as introduced in the context of equilibrium phase separation in Sec. 2.2:

$$\partial_t \rho = -\partial_x^2 [\alpha_1 \rho + \alpha_2 \partial_x^2 \rho + \alpha_3 \rho^2 - \alpha_4 \rho^3]. \quad (2.12)$$

Note, however, that due to the systematic approach introduced in [Pub4], the coefficients α_i of the CH equation are directly linked to the parameters of the full mean-field models that were the starting point of the derivation. In this sense, the derived CH equation is not a purely phenomenological model but can be directly linked to the full system close to the onset of active phase separation.

Starting in [Pub4], and continuing the work in [Pub5] and [Pub6], we consider different examples of nonlinear demixing or clustering and prove that they belong to the class of active phase separation described above. These examples of active phase separation are represented by the models introduced in Sec. 2.3.2 and include cell polarization (using a generic model in [Pub4], as well as a more specific model in [191]), chemotactically communicating cells (as modeled by variants of the Keller-Segel model in [Pub4] and [Pub5]) and motility-induced phase separation by active Brownian particles (in [Pub6]). In addition to introducing the concept of active phase separation and presenting the perturbative scheme that classifies systems as active phase separation, [Pub4] also assesses the validity range of the reduction to the CH equation. Comparisons of numerical

simulations between the full cell polarization and the derived CH equation show that the CH model is generally able to reproduce the solutions obtained from the full model. Given that the perturbative scheme is a weakly nonlinear analysis near the onset of phase separation, the quantitative agreement increases closer to phase separation onset. The best quantitative agreement can be achieved in the case of symmetric phase separation, i.e. if the symmetry-breaking quadratic nonlinearity in the CH equation vanishes ($\alpha_2 = 0$ in Eq. (2.9)). Note also that the transition to phase separation is supercritical in this case, while it becomes discontinuous in the case of asymmetric phase separation – as has already been known from the CH model [192].

Our perturbative approach can be seen as a framework to classify systems as active phase separation. Many systems only fall into the category of active phase separation for certain parameter ranges. These restrictions on system parameters stem from the limitations on the coefficients α_i of the CH model, Eq. (2.9). Due to the direct mathematical link to the parameters of the full system, these limitations can be transferred to the system parameters. α_4 , for example, is the coefficient of the saturation term $\propto u^3$ and should thus be positive in order to ensure saturation of the field $u(x, t)$ (and also justify expansion of the amplitude in orders of $\sqrt{\varepsilon}$). These parameter limitations on active phase separation are particularly interesting in the case of chemotactic cell communities. They have been investigated as another example of active phase separation in [Pub4], as well as in more detail in [Pub5]. By applying the perturbative scheme introduced in [Pub4] to different variants of the Keller-Segel model (as introduced in Sec. 2.3.2), we found that chemotactic cell clustering belongs to the class of active phase separation only if the model contains some form of damping. Possible damping mechanisms include density-dependent chemotactic sensitivity (discussed in [Pub4]), signal-dependent chemotactic sensitivity or nonlinear signal saturation (both discussed in [Pub5]). Either of these damping coefficients need to be finite in order to ensure saturation of the phase separation solution via the cubic nonlinearity. In return, this also means that clustering as described by the classic Keller-Segel model (without any form of damping) does not belong to the class of active phase separation. These insights may be related to the so-called blow-up solutions in the classic Keller-Segel model in which the cell density can locally increase to form a δ -peak [179, 193].

2.3.4. The extended Cahn-Hilliard model

A third example of active phase separation is so-called motility-induced phase separation (MIPS), i.e. the clustering of self-propelled particles. In [Pub6], we show that

a mean-field model for MIPS (see Sec. 2.3.2) can in fact be reduced to the classic CH equation at phase separation onset. Similarities between MIPS and classic phase separation have been recognized in the past. Speck et al. [188, 189] have derived an effective Cahn-Hilliard equation by applying a standard procedure known from unconserved systems for two special cases but without using the required scaling introduced in [Pub4]. Others have recently proposed phenomenological extensions of the classic CH model for MIPS with the argument that higher nonlinearities are the significant nonequilibrium contribution [194, 195].

In [Pub6], we extended the perturbative scheme introduced in [Pub4] to include higher order nonlinearities. With this, we were able for the first time to systematically derive an extended generic CH model for active phase separation:

$$\partial_t \rho = -\partial_x^2 \left[(\alpha_1 + \beta_1) \rho + (\alpha_2 + \beta_2) \partial_x^2 \rho + (\alpha_3 + \beta_3) \rho^2 - \alpha_4 \rho^3 + \beta_5 (\partial_x \rho)^2 + \beta_6 \partial_x^2 \rho^2 + \beta_7 \rho^4 \right]. \quad (2.13)$$

In this equation, the coefficients α_i are the leading order contributions as described in Eq. (2.9). The coefficients β_i can be derived by continuing the perturbative scheme (see Sec. 2.3.3) to the next higher order of ε . The first three higher order contributions (β_1 , β_2 and β_3) are quantitative corrections to the leading order terms that form the classic CH model. The last three terms (β_5 , β_6 and β_7) in Eq. (2.13) are the generic higher order nonlinearities for active phase separation.

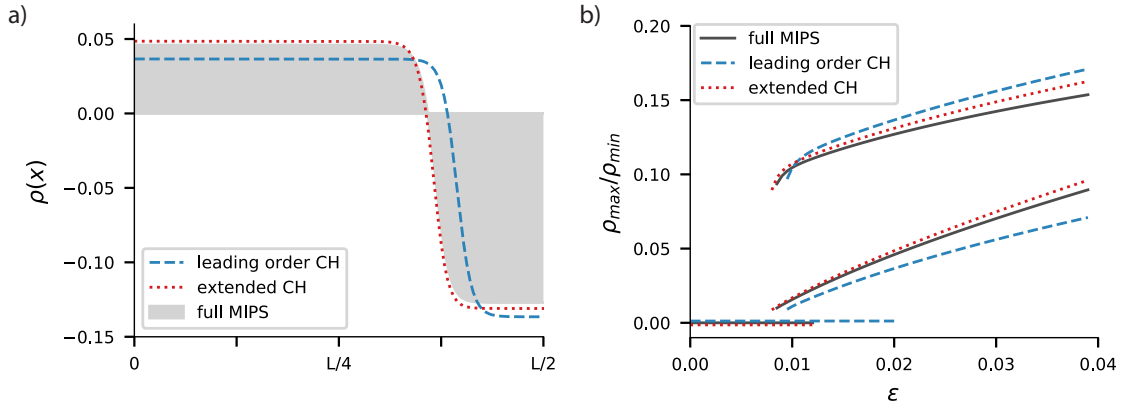


Fig. 2.2 – Comparison of leading order CH equation, extended CH equation and full MIPS model. a) Solution profiles in the asymmetric case for $\varepsilon = 0.02$. b) Plateau values as a function of the control parameter ε .

By rescaling space, time and ρ in the case of $\alpha_3 = 0$, Eq. (2.13) can be rewritten to

$$\begin{aligned} \partial_t \rho' &= -\partial_{x'}^2 [\rho' + \partial_{x'}^2 \rho' - \rho'^3] \\ &\quad -\sqrt{\varepsilon} \partial_{x'}^2 [\gamma_1 \rho'^2 + \gamma_2 \partial_{x'}^2 \rho'^2 + \gamma_3 (\partial_{x'} \rho')^2 + \gamma_4 \rho'^4]. \end{aligned} \quad (2.14)$$

The first part is the parameter-free version of the CH equation [196]. In this rescaled form it is easy to see that the higher order extensions (γ_1 - γ_4) vanish for $\varepsilon \rightarrow 0$, i.e. when approaching the onset of phase separation. This reiterates the fact that the classic CH model is the leading order description of active phase separation. Thus, the CH model in its classic equilibrium form is already sufficient to describe nonequilibrium behavior. The higher order extensions are useful to describe effects that occur further from phase separation onset. The extended CH model is, for example, able to reproduce the full MIPS model with high accuracy even when the leading order CH model already shows significant quantitative deviations (see Fig. 2.2).

2.3.5. Behavior beyond active phase separation

In [Pub4] and [Pub5], we mainly focused on the surprising similarities between phase separation in and out of equilibrium. The extension to higher nonlinearities in [Pub6] is a first indication that the dynamics of active phase separation can go beyond what has been known from equilibrium phase separation. [Pub7] is a first step to explore possible nonequilibrium phenomena that occur beyond the onset of active phase separation. We study a variation of the extended CH model derived in [Pub6] that includes an additional sixth derivative term, as well as one of the symmetry-breaking higher nonlinearities:

$$\partial_t \psi = -\partial_x^2 [\varepsilon \psi + D_4 \partial_x^2 \psi - D_6 \partial_x^4 \psi - \psi^3 + \beta_2 \psi \partial_x^2 \psi]. \quad (2.15)$$

This model thus includes as special cases both the extended CH model introduced in Sec. 2.3.4 (for $D_6 = 0$), as well as the conserved Swift-Hohenberg model introduced earlier in Sec. 1.5 (for $\beta_2 = 0$). For $D_4 > 0$, the homogeneous state $\psi = 0$ first undergoes a long-wavelength instability leading to active phase separation for $\varepsilon > 0$. Further from threshold, however, we find for certain parameter combinations a secondary instability triggering a transition to spatially periodic patterns (see Fig. 2.3). We explore the phase diagrams of phase separation and periodic solutions in more detail in [Pub7]. We also show that there is a region of bistability in which both phase-separated and periodic solutions may exist.

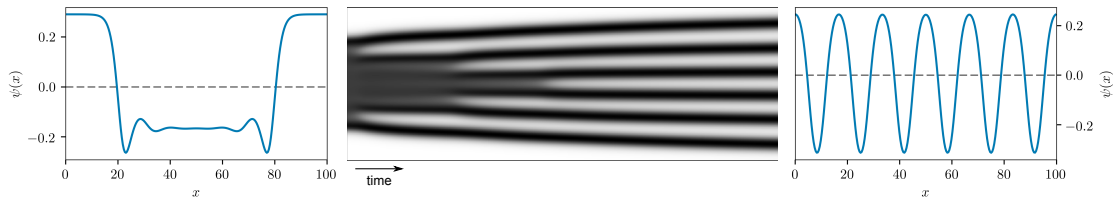


Fig. 2.3 – Transition from a phase-separated state (left) to a spatially periodic pattern (right) beyond a secondary bifurcation in a generic active phase separation model.

The existence of spatially periodic patterns in active phase separation systems is intriguing. This is a potential further parallel to phenomena known from equilibrium phase separation processes: Diblock copolymers are known to show a behavior called microphase separation [198–200]. Here, the covalent binding of two thermodynamically incompatible polymer blocks prevents phase separation on a macroscopic scale. Instead, the coarsening process in these systems is arrested on the length scale defined by the polymer sizes creating micro-scale spatial structures. The results presented in [Pub7] show that periodic patterns are also possible in active phase separation systems. Importantly, however, the periodic patterns in [Pub7] arise from a secondary instability while the classic microphase separation described above is the primary instability in the system. Examples of periodic patterns in nonequilibrium demixing systems include MIPS clusters which have been found to not always grow to the largest possible size but instead saturate to form a steady state of “arrested phase separation” [195]. Periodic patterns have also been found in colonies of reproducing bacteria [201], in the Vicsek flocking model [202], in simulations of self-propelled particles with long-range interactions [203] for chemorepulsive active colloids [181], and in mixtures of active and passive particles [204].

2.3.6. Outlook

The work presented in [Pub4]-[Pub7] introduced active phase separation as a new class of pattern formation and the Cahn-Hilliard model as the universal amplitude equation for the conserved order parameter near active phase separation onset. This lays the foundation for further investigation of nonequilibrium phase separation phenomena. With cell polarization, chemotactically communicating cells and motility-induced phase separation we already introduced multiple examples of active phase separation. There are, however, many other systems that could potentially be categorized into this new class of pattern formation. With our systematic perturbative scheme introduced in

[Pub4], we present a recipe to expand the class of active phase separation in the future. In the work presented here, we mainly focused on the stationary long-term behavior of active phase separation systems. Analyzing their coarsening dynamics in more detail is an interesting task to be tackled in the future as well. However, coarsening in the CH model scales logarithmically in one spatial dimension in the absence of additional noise [197]. In order to avoid these slow dynamics, our considerations should thus be expanded to two dimensions prior to detailed investigation of dynamics. Some first studies on the coarsening behavior in cell polarization models have been performed within our group [191].

In [Pub6] and sources referenced therein, we have already established that higher order nonlinearities are believed to play an important role in the dynamic behavior of active phase separation, especially in the context of MIPS. This aspect is thus worth analyzing in more detail in the future.

In [Pub7], we found that periodic patterns can arise from a secondary instability further from active phase separation onset. This is a first indication of a whole world of complex dynamic behavior and patterns that could lie beyond active phase separation and has yet to be explored. An interesting question in the context of spatially periodic patterns is whether a form of active microphase separation also exists immediately at onset. Several examples of active matter systems which suggest that this could be the case were referenced in Sec. 2.3.5. A similar perturbative approach as introduced in [Pub4] could generate a universal equation for active microphase separation.

Finally, the work presented here could be expanded to include oscillatory instabilities. For unconserved order parameters, we already know that the Ginzburg-Landau equation as the amplitude equation for spatially periodic patterns has a complex-valued counterpart: the complex Ginzburg-Landau equation describes the amplitude dynamics of patterns arising from an oscillatory finite-wavelength instability [112]. This raises the question what an oscillatory counterpart to the CH model would look like and which spatiotemporal dynamics arise from such an instability. Some preliminary work on this topic suggests rich spatiotemporal behavior such as coarsening traveling waves or bimodal solutions that is worth exploring in more detail in the future.

Bibliography

- [1] S. Frautschi. *Entropy in an Expanding Universe*. Science **217**, 593 (1982)
- [2] D. W. Thompson. *On Growth and Form*. Cambridge University Press, Cambridge, 1917.
- [3] P. Ball. *The Self-Made Tapestry: Pattern Formation in Nature*. Oxford University Press, New York, 2001.
- [4] P. Ball. *Patterns in Nature. Why the natural world looks the way it does*. University of Chicago Press, Chicago, 2016.
- [5] S. A. Kauffman. *At Home in the Universe: The Search for Laws of Self-organization and Complexity*. Oxford University Press, Oxford, 1995.
- [6] R. Lewin. *Complexity: life at the edge of chaos (2nd edition)* University of Chicago Press, Chicago, 1999.
- [7] R. Solé and B. Goodwin. *Signs of life: How complexity pervades biology*. Basic Books, New York, 2000.
- [8] T. R. J. Bossomaier and D. G. Green (Eds.). *Complex Systems*. Cambridge University Press, Cambridge, 2000.
- [9] E. Schrödinger. *What is life? The Physical Aspect of the Living Cell*. Cambridge University Press, Cambridge, 1944.
- [10] J.-F. Rupprecht and J. Prost. *A fresh eye on nonequilibrium systems*. Science **352**, 514 (2016)
- [11] S. Ornes. *How nonequilibrium thermodynamics speaks to the mystery of life*. PNAS **114**, 423 (2017)
- [12] D. Etling and R. A. Brown. *Roll vortices in the planetary boundary layer: A review*. Boundary-Layer Meteorol. **65**, 215 (1993)
- [13] G. Pretor-Pinney. *The Cloud Collector's Handbook*. Chronicle Books, San Francisco, 2011.

- [14] S. Kondo, M. Iwashita and M. Yamaguchi. *How animals get their skin patterns: fish pigment pattern as a live Turing wave*. Int. J. Dev. Biol. **53**, 851 (2009)
- [15] S. Kondo, and T. Miura. *Reaction-diffusion model as a framework for understanding biological pattern formation*. Science **329**, 1616 (2010)
- [16] A. P. Singh and C. Nüsslein-Volhard. *Zebrafish stripes as a model for vertebrate colour pattern formation*. Curr. Biol. **25**, R81 (2015)
- [17] C. A. Klausmeier. *Regular and Irregular Patterns in Semiarid Vegetation*. Science **284**, 1826 (1999)
- [18] E. Meron. *Modeling Dryland Landscapes*. Math. Model. Nat. Pheno. **6**, 163 (2011)
- [19] S. Getzin, H. Yizhaq, B. Bell, T. E. Erickson, A. C. Postle, I. Katra, O. Tzuk, Y. R. Zelnik, K. Wiegand, T. Wiegand, and E. Meron. *Discovery of fairy circles in Australia supports self-organization theory*. PNAS **113**, 3551 (2016)
- [20] C. E. Tarnita, J. A. Bonachela, E. Sheffer, J. A. Guyton, T. C. Coverdale, R. A. Long, and R. M. Pringle. *A theoretical foundation for multi-scale regular vegetation patterns*. Nature **541**, 398 (2017)
- [21] E. Meron. *From Patterns to Function in Living Systems: Dryland Ecosystems as a Case Study*. Annu. Rev. Condens. Matter Phys. **9**, 79 (2018)
- [22] R. Bastiaansen, O. Jaïbi, V. Deblauwe, M. B. Eppinga, K. Siteur, E. Siero, S. Mermoz, A. Bouvet, A. Doelman, and M. Rietkirk. *Multistability of model and real dryland ecosystems through spatial self-organization*. PNAS **115**, 11256 (2018)
- [23] M. Lappa. *Thermal Convection: Patterns, Evolution and Stability*. Wiley, Chichester, 2009.
- [24] Á. Buka and L. Kramer (Eds.). *Pattern Formation in Liquid Crystals*. Springer, New York, 1996.
- [25] L. A. Lugiato and R. Lefever. *Spatial Dissipative Structures in Passive Optical Systems*. Phys. Rev. Lett. **58**, 2209 (1987)
- [26] F. T. Arecchi, S. Boccaletti, and P. Ramazza. *Pattern formation and competition in nonlinear optics*. Phys. Rep. **318**, 1 (1999)

- [27] T. Tallinen, J. Y. Chung, F. Rousseau, N. Girard, J. Lefèvre, and L. Mahadevan. *On the growth and form of cortical convolutions*. Nat. Phys. **12**, 588 (2016)
- [28] M. Kücken and A. C. Newell. *A model for fingerprint formation*. EPL **68**, 141 (2004)
- [29] B. L. Karihaloo, K. Zhang, and J. Wang. *Honeybee combs: how the circular cells transform into rounded hexagons*. J. Roy. Soc. Interface **10**, 20130299 (2013)
- [30] T. Rätz. *The silent hexagon: explaining comb structures*. Synthese **194**, 1703 (2017)
- [31] R. A. Bagnold. *The Physics of Blown Sand and Desert Dunes*. Methuen, London, 1941.
- [32] M. Lämmel, A. Meiwald, H. Yizhaq, H. Tsoar, I. Katra, and K. Kroy. *Aeolian sand sorting and megaripple formation*. Nat. Phys. **14**, 759 (2018)
- [33] M. C. Cross and P. C. Hohenberg. *Pattern formation outside of equilibrium*. Rev. Mod. Phys. **65**, 851 (1993)
- [34] M. Cross and H. Greenside. *Pattern formation and dynamics in nonequilibrium systems*. Cambridge University Press, Cambridge, 2009.
- [35] I. R. Epstein and K. Showalter. *Nonlinear Chemical Dynamics: Oscillations, Patterns, and Chaos*. J. Phys. Chem. **100**, 13132 (1996)
- [36] A. T. Winfree. *The Geometry of Biological Time. Biomathematics Vol. 8*. Springer, New York, 1980.
- [37] L. Glass and M. C. Mackey. *From Clocks to Chaos: The Rhythms of Life*. Princeton University Press, Princeton, 1988.
- [38] R. G. Foster and L. Kreitzman. *Rhythms of Life: The Biological Clocks that Control the Daily Lives of Every Living Thing*. Profile Books Ltd, London, 2005.
- [39] E. Moses and V. Steinberg. *Flow patterns and nonlinear behavior of traveling waves in a convective binary fluid*. Phys. Rev. A **34**, 693(R) (1986)
- [40] E. Moses, J. Fineberg, and V. Steinberg. *Multistability and confined traveling-wave patterns in a convecting binary mixtures*. Phys. Rev. A **35**, 2757 (1987)

- [41] R. Heinrichs, G. Ahlers, and D. S. Cannell. *Traveling waves and spatial variations in the convection of a binary mixture*. Phys. Rev. A **35**, 2761 (1987)
- [42] P. Kolodner, C. M. Surko, and H. Williams. *Dynamics of traveling waves near the onset of convection in binary fluid mixtures*. Physica D **37**, 319 (1989)
- [43] L. Kramer and W. Pesch. *Convection instabilities in nematic liquid crystals*. Annu. Rev. Fluid Mech. **27**, 515 (1995)
- [44] A. T. Winfree. *Spiral Waves of Chemical Activity*. Science **175**, 634 (1972)
- [45] R. Kapral and K. Showalter (Eds.). *Chemical waves and patterns*. Springer Science+Business Media, Dordrecht, 1995.
- [46] I. R. Epstein and J. A. Pojman. *An introduction to nonlinear chemical dynamics: Oscillations, Waves, Patterns, and Chaos*. Oxford University Press, New York, 1998.
- [47] M. Loose, E. Fischer-Friedrich, J. Ries, K. Kruse, and P. Schwille. *Spatial regulators for bacterial cell division self-organize into surface waves in vitro*. Science **320**, 789 (2008)
- [48] D. M. Parichy. *Pigment patterns: fish in stripes and spots*. Curr. Biol. **13**, R947 (2003)
- [49] T. Gregor, W. Bialek, R. R. de Ruyter van Steveninck, D. W. Tank, and E. F. Wieschaus. *Diffusion and scaling during early embryonic pattern formation*. PNAS **102**, 18403 (2005)
- [50] M. V. Staller, C. C. Fowlkes, M. D. J. Bragdon, Z. Wunderlich, J. Estrada, and A. H. DePace. *A gene expression atlas of a bicoid-depleted Drosophila embryo reveals early canalization of cell fate*. Development **142**, 587 (2015)
- [51] J. Wesfreid, Y. Pomeau, M. Dubois, C. Normand, and P. Bergé. *Critical effects in Rayleigh-Bénard convection*. J. Phys. France **39**, 725 (1978)
- [52] A. V. Getling. *Rayleigh-Bénard Convection: Structures and Dynamics*. World Scientific, Singapore, 1998.

- [53] J. Swift and P. C. Hohenberg. *Hydrodynamic fluctuations at the convective instability*. Phys. Rev. A **15**, 319 (1977)
- [54] E. M. Lifshitz and L. P. Pitaevskii. *Statistical Physics, Part 2 (Course of Theoretical Physics, Vol. 9)* Butterworth-Heinemann, Oxford, 1980.
- [55] A. C. Newell and J. A. Whitehead. *Finite bandwidth, finite amplitude convection*. J. Fluid Mech. **38**, 279 (1969)
- [56] L. A. Segel. *Distant side-walls cause slow amplitude modulation of cellular convection*. J. Fluid Mech. **38**, 203 (1969)
- [57] Y. Pomeau and P. Manneville. *Wavelength selection in cellular flows*. Phys. Lett. A **75**, 296 (1980)
- [58] Y. Pomeau and S. Zaleski. *Wavelength selection in one-dimensional cellular structures*. J. Phys. France **42**, 515 (1981)
- [59] M. C. Cross, P. C. Hohenberg, and S. A. Safran. *Wave number selection in Rayleigh-Bénard convection: A numerical study*. Physica D **5**, 75 (1982)
- [60] M. C. Cross, P. G. Daniels, P. C. Hohenberg, and E. D. Siggia. *Phase-winding solutions in a finite container above the convective threshold*. J. Fluid. Mech. **127**, 155 (1983)
- [61] R. Heinrichs, G. Ahlers, and D. S. Cannell. *Effects of Finite Geometry on the Wave Number of Taylor-Vortex Flow*. Phys. Rev. Lett. **56**, 1794 (1986)
- [62] G. Ahlers, D. S. Cannell, M. A. Dominguez-Lerma, and R. Heinrichs. *Wavenumber selection and Eckhaus instability in Couette-Taylor flow*. Physica D **23**, 202 (1986)
- [63] P. Arcuri and J. D. Murray. *Pattern sensitivity to boundary and initial conditions in reaction-diffusion models*. J. Math. Biol. **24**, 141 (1986)
- [64] L. Kramer, E. Ben-Jacob, H. Brand, and M. C. Cross. *Wavelength Selection in Systems Far from Equilibrium*. Phys. Rev. Lett. **49**, 1891 (1982)
- [65] Y. Pomeau and S. Zaleski. *Pattern selection in slowly varying environment*. J. Physique Lett. **44**, 135 (1983)
- [66] D. S. Cannell, M. A. Dominguez-Lerma, and G. Ahlers. *Experiments on Wave*

- Number Selection in Rotating Couette-Taylor Flow.* Phys. Rev. Lett. **50**, 1365 (1983)
- [67] M. C. Cross. *Wave-number selection by soft boundaries near threshold.* Phys. Rev. A **29**, 391 (1984)
- [68] H. Riecke. *Pattern Selection by Weakly Pinning Ramps.* EPL **2**, 1 (1986)
- [69] M. C. Cross. *Boundary conditions on the envelope function of convective rolls close to onset.* Phys. Fluids **25**, 936 (1982)
- [70] H. S. Greenside and W. M. Coughran, Jr. *Nonlinear pattern formation near the onset of Rayleigh-Bénard convection.* Phys. Rev. A **30**, 398 (1984)
- [71] C. Varea, J. L. Aragón, and R. A. Barrio. *Confined Turing patterns in growing systems.* Phys. Rev. E **56**, 1250 (1997)
- [72] E. J. Crampin, E. A. Gaffney, and P. K. Maini. *Reaction and Diffusion on Growing Domains: Scenarios for Robust Pattern Formation.* Bull. Math. Biol. **61**, 1093 (1999)
- [73] C. Varea, J. L. Aragón, and R. A. Barrio. *Turing patterns on a sphere.* Phys. Rev. E **60**, 4588 (1999)
- [74] R. G. Plaza, F. Sánchez-Garduño, P. Padilla, R. A. Barrio, and P. K. Maini. *The Effect of Growth and Curvature on Pattern Formation.* J. Dyn. Differ. Equ. **16**, 1093 (2004)
- [75] D. G. Míguez, M. Dolnik, A. P. Muñuzuri, and L. Kramer. *Effect of Axial Growth on Turing Pattern Formation.* Phys. Rev. Lett. **96**, 048304 (2006)
- [76] N. Stoop, R. Lagrange, D. Terwagne, P. M. Reis, and J. Dunkel. *Curvature-induced symmetry breaking determines elastic surface patterns.* Nat. Mater. **14**, 337 (2015)
- [77] M. C. Cross. *Traveling and standing waves in binary-fluid convection in finite geometries.* Phys. Rev. Lett. **57**, 2935 (1986)
- [78] M. C. Cross. *Structure of nonlinear traveling-wave states in finite geometries.* Phys. Rev. A **38**, 3593 (1988)

- [79] C. Pérez-García, E. Pampaloni, and S. Ciliberto. *Finite-Size Effects in the Transition from Hexagons to Rolls in Convective Systems*. EPL **12**, 51 (1990)
- [80] E. Kaplan and V. Steinberg. *Transition from confined to extended traveling waves in a convective binary mixture*. Phys. Rev. A **46**, R2996(R) (1992)
- [81] V. M. Eguíluz, E. Hernández-García, and O. Piro. *Boundary effects in extended dynamical systems*. Physica A **283**, 48 (2000)
- [82] T. Kohsokabe and K. Kaneko. *Boundary-induced pattern formation from temporal oscillation: Spatial map analysis*. EPL **116**, 48005 (2016)
- [83] A. P. Muñuzuri, M. Dolnik, A. M. Zhabotinsky, and I. R. Epstein. *Control of the Chlorine Dioxide-Iodine-Malonic Acid Oscillating Reaction by Illumination*. J. Am. Chem. Soc. **121**, 8065 (1999)
- [84] J. Schweizer, M. Loose, M. Bonny, K. Kruse, I. Mönch, and P. Schwille. *Geometry sensing by self-organized protein patterns*. PNAS **109**, 15283 (2012)
- [85] A. M. Turing. *The Chemical Basis of Morphogenesis*. Phil. Trans. Roy. Soc. B **237**, 37 (1952)
- [86] I. Prigogine and R. Lefever. *Symmetry Breaking Instabilities in Dissipative Systems. II*. J. Chem. Phys. **48**, 1695 (1968)
- [87] G. Nicolis and I. Prigogine. *Self-Organization in Nonequilibrium Systems: From Dissipative Structures to Order through Fluctuations*. Wiley, New York, 1977.
- [88] B. Peña and C. Pérez-García. *Stability of Turing patterns in the Brusselator model*. Phys. Rev. E **64**, 056213 (2001)
- [89] P. Coullet. *Commensurate-incommensurate transition in nonequilibrium systems*. Phys. Rev. Lett. **56**, 724 (1986)
- [90] S. Rüdiger, D. G. Míguez, A. P. Muñuzuri, F. Sagués, and J. Casademunt. *Dynamics of Turing Patterns under Spatiotemporal Forcing*. Phys. Rev. Lett. **90**, 128301 (2003)
- [91] R. Manor, A. Hagberg, and E. Meron. *Wave-number locking in spatially forced pattern-forming systems*. EPL **83**, 10005 (2008)

- [92] S. Weiss, G. Seiden, and E. Bodenschatz. *Pattern formation in spatially forced thermal convection*. *New J. Phys.* **14**, 053010 (2012)
- [93] Y. Mau, L. Haim, A. Hagberg, and E. Meron. *Competing resonances in spatially forced pattern-forming systems*. *Phys. Rev. E* **88**, 032917 (2013)
- [94] M. Dolnik, I. Berenstein, A. M. Zhabotinsky, and I. R. Epstein. *Spatial Periodic Forcing of Turing Structures*. *Phys. Rev. Lett.* **87**, 238301 (2001)
- [95] D. G. Míguez, V. Pérez-Villar, and A. P. Muñuzuri. *Turing instability controlled by spatiotemporal imposed dynamics*. *Phys. Rev. E* **71**, 066217 (2005)
- [96] L. Yang, M. Dolnik, A. M. Zhabotinsky, and I. R. Epstein. *Turing patterns beyond hexagons and stripes*. *Chaos* **16**, 037114 (2006)
- [97] H. Nishioka, K. Kida, O. Yano, and Q. Tran-Cong. *Phase Separation of a Polymer Mixture Driven by a Gradient of Light Intensity*. *Macromolecules* **33**, 4301 (2000)
- [98] P. Glock, J. Broichhagen, S. Kretschmer, P. Blumhardt, J. Mücksch, D. Trauner, and P. Schwille. *Optical Control of a Biological Reaction-Diffusion System*. *Angew. Chem. Int. Ed.* **57**, 2362 (2018)
- [99] M. Loose, K. Kruse, and P. Schwille. *Protein self-organization: Lessons from the Min system*. *Annu. Rev. Biophys.* **40**, 315 (2011)
- [100] V. Wells Rowlett and W. Margolin. *The bacterial Min system*. *Curr. Biol.* **23**, R553 (2013)
- [101] L. Wettmann and K. Kruse. *The Min-protein oscillations in Escherichia coli: an example of self-organized cellular protein waves*. *Phil. Trans. R. Soc. B* **373**, 20170111 (2018)
- [102] J. Lutkenhaus. *Assembly dynamics of the bacterial MinCDE system and spatial regulation of the Z ring*. *Annu. Rev. Biochem.* **76**, 539 (2007)
- [103] D. M. Raskin and P. A. J. de Boer. *Rapid pole-to-pole oscillation of a protein required for directing division to the middle of Escherichia coli*. *PNAS* **96**, 4971 (1999)
- [104] M. Loose, E. Fischer-Friedrich, C. Herold, K. Kruse, and P. Schwille. *Min protein*

- patterns emerge from rapid rebinding and membrane interaction of MinE.* Nat. Struct. Mol. Biol. **18**, 577 (2011)
- [105] K. Park, W. Wu, K. P. Battaile, S. Lovell, T. Holyoak, and J. Lutkenhaus. *The Min Oscillator uses MinD-dependent Conformational Changes in MinE to Spatially Regulate Cytokinesis.* Cell **146**, 396 (2011)
- [106] J. Halatek and E. Frey. *Highly canalized MinD transfer and MinE sequestration explain the origin of robust MinCDE-protein dynamics.* Cell Rep. **1**, 741 (2012)
- [107] M. Bonny, E. Fischer-Friedrich, M. Loose, P. Schwille, and K. Kruse. *Membrane Binding of MinE allows for a comprehensive description of Min-Protein Pattern Formation.* PLoS Comput. Biol. **9**, e1003347 (2013)
- [108] J. Halatek and E. Frey. *Effective 2D model does not account for geometry sensing by self-organized protein patterns.* PNAS **111**, E1817 (2014)
- [109] J. Denk, S. Kretschmer, J. Halatek, C. Hartl, P. Schwille, and E. Frey. *MinE conformational switching confers robustness on self-organized Min protein patterns.* PNAS **115**, 4553 (2018)
- [110] M. Howard, A. D. Rutenberg, S. de Vet. *Dynamic compartmentalization of bacteria: Accurate cell vision in E. coli.* Phys. Rev. Lett. **87**, 278102 (2001)
- [111] H. Meinhardt and P. A. J. de Boer. *Pattern formation in Escherichia coli: A model for the pole-to-pole oscillations of Min proteins and the localization of the division site.* PNAS **98**, 14202 (2001)
- [112] I. Aranson and L. Kramer. *The world of the complex Ginzburg-Landau equation.* Rev. Mod. Phys. **74**, 99 (2002)
- [113] L. Gelens and E. Knobloch. *Traveling waves and defects in the complex Swift-Hohenberg equation.* Phys. Rev. E **84**, 056203 (2011)
- [114] L. Yang, M. Dolnik, A. M. Zhabotinsky, and I. R. Epstein. *Pattern formation arising from interactions between Turing and wave instabilities.* J. Chem. Phys. **117**, 7259 (2002)
- [115] M. Lowe and J. P. Gollub. *Pattern selection near the onset of convection: the Eckhaus instability.* Phys. Rev. Lett. **55**, 2575 (1985)

- [116] L. Kramer and W. Zimmermann. *On the Eckhaus instability for spatially periodic patterns*. Physica D **16**, 221 (1985)
- [117] B. Janiaud, A. Pumir, D. Bensimon, V. Croquette, H. Richter, and L. Kramer. *The Eckhaus instability for traveling waves*. Physica D **55**, 269 (1992)
- [118] E. Fischer-Friedrich, G. Meacci, J. Lutkenhaus, H. Chaté, and K. Kruse. *Intra- and intercellular fluctuations in Min-protein dynamics decrease with cell length*. PNAS **107**, 6134 (2010)
- [119] F. Wu, J. Halatek, M. Reiter, E. Kingma, E. Frey, and C. Dekker. *Multistability and dynamic transitions of intracellular Min protein patterns*. Mol. Sys. Biol. **12**, 873 (2016)
- [120] F. Wu, B. G. C. van Schie, J. E. Keymer, and C. Dekker. *Symmetry and scale orient Min protein patterns in shaped bacterial sculptures*. Nat. Nanotechnol. **10**, 719 (2015)
- [121] K. Zieske and P. Schwille. *Reconstitution of self-organizing protein gradients as spatial cues in cell-free systems*. eLife **3**, e03949 (2014)
- [122] Y. Caspi and C. Dekker. *Mapping out Min protein patterns in fully confined fluidic chambers*. eLife **5**, e19271 (2016)
- [123] W. van Saarloos and P. C. Hohenberg. *Fronts, pulses, sources and sinks in generalized complex Ginzburg-Landau equations*. Physica D **56**, 303 (1992)
- [124] S. M. Murray and V. Sourjik. *Self-organization and positioning of bacterial protein clusters*. Nat. Phys. **13**, 1006 (2017)
- [125] E. Knobloch. *Pattern selection in binary-fluid convection at positive separation ratios*. Phys. Rev. A **40**, 1549 (1989)
- [126] P. C. Matthews and S. M. Cox. *Pattern formation with a conservation law*. Nonlinearity **13**, 1293 (2000)
- [127] H. Emmerich, H. Löwen, R. Wittkowski, T. Gruhn, G. I. Tóth, G. Tegze, and L. Gránásy. *Phase-field-crystal models for condensed matter dynamics on atomic length and diffusive time scales: an overview*. Adv. Phys. **61**, 665 (2012)

- [128] U. Thiele, A. J. Archer, M. J. Robbins, H. Gomez, and E. Knobloch. *Localized states in the conserved Swift-Hohenberg equation with cubic nonlinearity*. Phys. Rev. E **87**, 042915 (2013)
- [129] S. Ramaswamy. *The Mechanics and Statistics of Active Matter*. Annu. Rev. Condens. Matter Phys. **1**, 323 (2010)
- [130] M. C. Marchetti, J. F. Joanny, S. Ramaswamy, T. B. Liverpool, J. Prost, M. Rao, and R. Aditi Simha. *Hydrodynamics of soft active matter*. Rev. Mod. Phys. **85**, 1143 (2013)
- [131] G. Popkin. *The physics of life*. Nature **529**, 16 (2016)
- [132] G. Grégoire and H. Chaté. *Onset of Collective and Cohesive Motion*. Phys. Rev. Lett. **92**, 025702 (2004)
- [133] D. Saintillan and M. J. Shelley. *Instabilities, pattern formation, and mixing in active suspensions*. Phys. Fluids **20**, 123304 (2008)
- [134] T. Vicsek and A. Zafeiris. *Collective motion*. Phys. Rep. **517**, 71 (2012)
- [135] S. Saha, R. Golestanian, and S. Ramaswamy. *Clusters, asters, and collective oscillations in chemotactic colloids*. Phys. Rev. E **89**, 062316 (2014)
- [136] A. Zöttl and H. Stark. *Hydrodynamics Determines Collective Motion and Phase Behavior of Active Colloids in Quasi-Two-Dimensional Confinement*. Phys. Rev. Lett. **112**, 118101 (2014)
- [137] J. K. Parrish and L. Edelstein-Keshet. *Complexity, Pattern, and Evolutionary Trade-Offs in Animal Aggregation*. Science **284**, 99 (1999)
- [138] J. Buhl, D. J. T. Sumpter, I. D. Couzin, J. J. Hale, E. Despland, E. R. Miller, and S. J. Simpson. *From Disorder to Order in Marching Locusts*. Science **312**, 1402 (2006)
- [139] A. Cavagna and I. Giardina. *Bird flocks as condensed matter*. Annu. Rev. Condens. Matter Phys. **5**, 183 (2014)
- [140] C. Dombrowski, L. Cisneros, S. Chatkaew, R. E. Goldstein, and J. O. Kessler.

- Self-Concentration and Large-Scale Coherence in Bacterial Dynamics*. Phys. Rev. Lett. **93**, 098103 (2004)
- [141] A. Sokolov, I. S. Aranson, J. O. Kessler, and R. E. Goldstein. *Concentration dependence of the collective dynamics of swimming bacteria*. Phys. Rev. Lett. **98**, 158102 (2007)
- [142] H. P. Zhang, A. Be'er, E.-L. Florin, and H. L. Swinney. *Collective motion and density fluctuations in bacterial colonies*. PNAS **107**, 13626 (2010)
- [143] E. Ben-Jacob, I. Cohen, and H. Levine. *Cooperative self-organization of microorganisms*. Adv. Phys. **49**, 395 (2010)
- [144] F. Jülicher, K. Kruse, J. Prost, and J. F. Joanny. *Active behavior of the Cytoskeleton*. Phys. Rep. **449**, 3 (2007)
- [145] S. Sánchez, L. Soler, and J. Katuri. *Chemically Powered Micro- and Nanomotors*. Angew. Chem. Int. Ed. **54**, 1414 (2015)
- [146] C. Bechinger, R. Di Leonardo, H. Löwen, C. Reichhardt, G. Volpe, and G. Volpe. *Active particles in complex and crowded environments*. Rev. Mod. Phys. **88**, 045006 (2016)
- [147] J. L. Anderson. *Colloid Transport by Interfacial Forces*. Ann. Rev. Fluid Mech. **21**, 61 (1989)
- [148] R. Golestanian, T. B. Liverpool, and A. Ajdari. *Designing phoretic micro- and nano-swimmers*. New. J. Phys. **9**, 126 (2007)
- [149] M. N. Popescu, W. E. Uspal, C. Bechinger, and P. Fischer. *Chemotaxis of Active Janus Nanoparticles*. Nano Lett. **18**, 5345 (2018)
- [150] D. Yamada, T. Hondou, and M. Sano. *Coherent dynamics of an asymmetric particle in a vertically vibrating bed*. Phys. Rev. E **67**, 040301(R) (2003)
- [151] J. Deseigne, O. Dauchot, and H. Chaté. *Collective Motion of Vibrated Polar Disks*. Phys. Rev. Lett. **105**, 098001 (2010)
- [152] J. Palacci, S. Sacanna, A. P. Steinberg, D. J. Pine, and P. M. Chaikin. *Living Crystals of Light-Activated Colloidal Surfers*. Science **339**, 936 (2013)

- [153] T. Sanchez, D. T. N. Chen, S. J. DeCamp, M. Heymann, and Z. Dogic. *Spontaneous motion in hierarchically assembled active matter*. *Nature* **491**, 431 (2012)
- [154] A. Doostmohammadi, J. Ignés-Mullol, J. M. Yeomans, and F. Sagués. *Active nematics*. *Nat. Commun.* **9**, 3246 (2018)
- [155] L. Giomi, N. Hawley-Weld, and L. Mahadevan. *Swarming, swirling and stasis in sequestered bristle-bots*. *Proc. R. Soc. A* **469**, 20120637 (2013)
- [156] A. J. Bray. *Theory of phase-ordering kinetics*. *Adv. Phys.* **43**, 357 (1994)
- [157] P. M. Chaikin and T. C. Lubensky. *Principles of Condensed Matter Physics*. Cambridge University Press, Cambridge, 1995.
- [158] R. A. L. Jones. *Soft Condensed Matter*. Oxford University Press, Oxford, 2002.
- [159] A. Onuki. *Phase Transition Dynamics*. Cambridge University Press, Cambridge, 2004.
- [160] J. S. Langer. *Theory of spinodal decomposition in alloys*. *Ann. Phys.* **65**, 53 (1971)
- [161] R. Mauri, R. Shinnar, and G. Triantafyllou. *Spinodal decomposition in binary mixtures*. *Phys. Rev. E* **53**, 2613 (1996)
- [162] M. E. Cates and E. Tjhung. *Theories of binary fluid mixtures: from phase-separation kinetics to active emulsions*. *J. Fluid Mech.* **836**, P1 (2018)
- [163] P. G. de Gennes. *Dynamics of fluctuations and spinodal decomposition in polymer blends*. *J. Chem. Phys.* **72**, 4756 (1980)
- [164] J. W. Cahn and J. E. Hilliard. *Free Energy of a Nonuniform System. I. Interfacial Free Energy*. *J. Chem. Phys.* **28**, 258 (1958)
- [165] A. A. Hyman, C. A. Weber, and F. Jülicher. *Liquid-Liquid Phase Separation in Biology*. *Annu. Rev. Cell Dev. Biol.* **30**, 39 (2014)
- [166] D. W. Gerlich. *Cell organization by liquid phase separation*. *Nat. Rev. Mol. Cell Bio.* **18**, 593 (2017)
- [167] S. Boeynaems, S. Alberti, N. L. Fawzi, T. Mittag, M. Polymenidou, F. Rousseau,

- J. Schymkowitz, J. Shorter, B. Wolozin, L. Van Den Bosch, P. Tompa, M. Fuxreiter. *Protein Phase Separation: A New Phase in Cell Biology*. Trends Cell Biol. **28**, 420 (2018)
- [168] C. L. Cuevas-Velazquez and J. R. Dinneny. *Organization out of disorder: liquid-liquid phase separation in plants*. Curr. Opin. Plant. Biol. **45**, 68 (2018)
- [169] B. Alberts et al. *Molecular biology of the cell, 4th edition*. Garland Science, New York, 2002.
- [170] A. Wodarz. *Establishing cell polarity in development*. Nat. Cell Biol. **4**, E39 (2002)
- [171] B. J. Thompson. *Cell polarity: models and mechanisms from yeast, worms and flies*. Development **140**, 13 (2013)
- [172] J. P. Campanale, T. Y. Sun, and D. J. Montell. *Development and dynamics of cell polarity at a glance*. J. Cell. Sci. **130**, 1201 (2017)
- [173] W.-J. Rappel and L. Edelstein-Keshet. *Mechanisms of cell polarization*. Curr. Opin. Syst. Biol. **3**, 43 (2017)
- [174] L. Edelstein-Keshet, W. R. Holmes, M. Zajac, and M. Dutot. *From simple to detailed models for cell polarization*. Phil. Trans. R. Soc. B **368**, 20130003 (2013)
- [175] M. Eisenbach. *Chemotaxis*. Imperial College Press, London, 2004.
- [176] G. H. Wadhams and J. P. Armitage. *Making sense of it all: bacterial chemotaxis*. Nat. Rev. Mol. Cell Biol. **5**, 1024 (2004)
- [177] E. F. Keller and L. A. Segel. *Initiation of Slime Mold Aggregation as an Instability*. J. Theor. Biol. **26**, 399 (1970)
- [178] E. F. Keller and L. A. Segel. *Model for Chemotaxis*. J. Theor. Biol. **30**, 225 (1971)
- [179] T. Hillen and K. J. Painter. *A user's guide to PDE models for chemotaxis*. J. Math. Biol. **58**, 183 (2009)
- [180] M. Meyer, L. Schimansky-Geier, and P. Romanczuk. *Active Brownian agents with concentration-dependent chemotactic sensitivity*. Phys. Rev. E **89**, 022711 (2014)

- [181] B. Liebchen, D. Marenduzzo, I. Pagonabarraga, and M. E. Cates. *Clustering and Pattern Formation in Chemorepulsive Active Colloids*. Phys. Rev. Lett. **115**, 258301 (2015)
- [182] J. Tailleur and M. E. Cates. *Statistical Mechanics of Interacting Run-and-Tumble Bacteria*. Phys. Rev. Lett. **100**, 218103 (2008)
- [183] F. D. C. Farrell, M. C. Marchetti, D. Marenduzzo, and J. Tailleur. *Pattern Formation in Self-Propelled Particles with Density-Dependent Motility*. Phys. Rev. Lett. **108**, 248101 (2012)
- [184] G. S. Redner, M. F. Hagan, and A. Baskaran. *Structure and Dynamics of a Phase-Separating Active Colloidal Fluid*. Phys. Rev. Lett. **110**, 055701 (2013)
- [185] J. Bialké, H. Löwen, and T. Speck. *Microscopic theory for the phase separation of self-propelled repulsive disks*. EPL **103**, 30008 (2013)
- [186] I. Buttinoni, J. Bialké, F. Kümmel, H. Löwen, C. Bechinger, and T. Speck. *Dynamical Clustering and Phase Separation in Suspensions of Self-Propelled Colloidal Particles*. Phys. Rev. Lett. **110**, 238301 (2013)
- [187] M. E. Cates and J. Tailleur. *Motility-Induced Phase Separation*. Annu. Rev. Condens. Matter Phys. **6**, 219 (2015)
- [188] T. Speck, J. Bialké, A. M. Menzel, and H. Löwen. *Effective Cahn-Hilliard Equation for the Phase Separation of Active Brownian Particles*. Phys. Rev. Lett. **112**, 218304 (2014)
- [189] T. Speck, A. M. Menzel, J. Bialké, and H. Löwen. *Dynamical mean-field theory and weakly non-linear analysis for the phase separation of active Brownian particles*. J. Chem. Phys. **142**, 224109 (2015)
- [190] J. Stenhammer, A. Tiribocchi, R. J. Allen, D. Marenduzzo, and M. E. Cates. *Continuum Theory of Phase Separation Kinetics for Active Brownian Particles*. Phys. Rev. Lett. **111**, 145702 (2013)
- [191] F. Bergmann and W. Zimmermann. *On systems-spanning demixing properties of cell-polarization*. Submitted to PLoS One (2018)

- [192] A. Novick-Cohen. *The nonlinear Cahn-Hilliard equation: Transition from spinodal decomposition to nucleation behavior*. J. Stat. Phys. **38**, 707 (1985)
- [193] V. Nanjundiah. *Chemotaxis, signal relaying and aggregation morphology*. J. Theor. Biol. **42**, 63 (1973)
- [194] R. Wittkowski, A. Tiribocchi, J. Stenhammer, R. J. Allen, D. Marenduzzo, and M. E. Cates. *Scalar ϕ^4 field theory for active-particle phase separation*. Nat. Comm. **5**, 4351 (2014)
- [195] E. Tjhung, C. Nardini, and M. E. Cates. *Cluster phases and bubbly phase separation in active fluids: Reversal of the Ostwald process*. Phys. Rev. X **8**, 031080 (2018)
- [196] R. C. Desai and R. Kapral. *Dynamics of Self-Organized and Self-Assembled Structures*. Cambridge Univ. Press, Cambridge, 2009
- [197] P. Politi and C. Misbah. *Nonlinear dynamics in one dimension: A criterion for coarsening and its temporal law*. Phys. Rev. E **73**, 036133 (2006)
- [198] F. S. Bates. *Polymer-Polymer Phase Behavior*. Science **251**, 898 (1991)
- [199] Y. Mai and A. Eisenberg. *Self-assembly of block copolymers*. Chem. Soc. Rev. **41**, 5969 (2012)
- [200] H. Feng, X. Lu, W. Wang, N.-G. Kang, and J. W. Mays. *Block Copolymers: Synthesis, Self-Assembly, and Applications*. Polymers **9**, 494 (2017)
- [201] M. E. Cates, D. Marenduzzo, I. Pagonabarraga, and J. Tailleur. *Arrested phase separation in reproducing bacteria creates a generic route to pattern formation*. PNAS **107**, 11715 (2010)
- [202] A. P. Solon, H. Chaté, and J. Tailleur. *From Phase to Microphase Separation in Flocking Models: The Essential Role of Nonequilibrium Fluctuations*. Phys. Rev. Lett. **114**, 068101 (2015)
- [203] C. Tung, J. Harder, C. Valeriani, and A. Cacciuto. *Micro-phase separation in two dimensional suspensions of self-propelled spheres and dumbbells*. Soft Matter **12**, 555 (2016)

[204] C. Reichhardt and C. J. O. Reichhardt. *Reversibility, pattern formation, and edge transport in active chiral and passive disk mixtures*. J. Chem. Phys. **150**, 064905 (2019)

Part II.

Publications

3. List of publications, preprints and drafts

- [Pub1] *Pattern orientation in finite domains without boundaries*
Lisa Rapp, Fabian Bergmann, and Walter Zimmermann
EPL **113**, 28006 (2016)
- [Pub2] *Size matters for nonlinear (protein) waves*
Fabian Bergmann, Lisa Rapp, and Walter Zimmermann
New. J. Phys. **20**, 072001 (2018)
- [Pub3] *Polarity bias in systems with broken up-down symmetry*
Lisa Rapp, Fabian Bergmann, and Walter Zimmermann
- [Pub4] *Active phase separation: a universal approach*
Fabian Bergmann, Lisa Rapp, and Walter Zimmermann
Phys. Rev. E **98**, 020603(R) (2018)
- [Pub5] *Universal aspects of collective behavior in chemotactic systems*
Lisa Rapp and Walter Zimmermann
submitted to Phys. Rev. E (04/2019)
- [Pub6] *Systematic extension of the Cahn-Hilliard model
for motility-induced phase separation*
Lisa Rapp, Fabian Bergmann, and Walter Zimmermann
Eur. Phys. J. E **42**, 57 (2019)
- [Pub7] *Spatially periodic patterns succeed active phase separation*
Lisa Rapp and Walter Zimmermann

4. Author's contributions

The following overview breaks down the contributions of the individual authors to the publications listed in Sec. 3. The following abbreviations are used: LR = Lisa Rapp, FB = Fabian Bergmann, WZ = Walter Zimmermann.

- [Pub1] LR performed numerical simulations. FB developed and implemented the expansion of the control parameter drop. All authors designed the project, contributed to the discussion and interpretation of the results and co-wrote the manuscript.
- [Pub2] FB and LR contributed equally to this publication. LR performed linear stability analysis. FB performed numerical simulations and developed concepts for the analytical calculations. All authors designed the project, contributed to the discussion and interpretation of the results and co-wrote the manuscript.
- [Pub3] LR performed (semi-)analytical calculations and interpreted the results. FB provided numerical simulations. All authors contributed to discussion and interpretation of results. LR wrote the manuscript.
- [Pub4] All authors contributed to the development of the perturbative scheme. FB performed analytical calculations and numerical simulations for the cell polarization model. LR performed analytical calculations and numerical simulations for the model of chemotactically communicating cells. All authors designed the project, contributed to the discussion and interpretation of the results and co-wrote the manuscript.
- [Pub5] LR performed analytical calculations and numerical simulations. All authors designed the project, contributed to the discussion and interpretation of the results and co-wrote the manuscript.

- [Pub6] All authors contributed to the extension of the perturbative scheme and interpretations of the results. LR and FB both performed analytical calculations. LR performed numerical simulations. LR wrote the manuscript with participation by FB and WZ.
- [Pub7] All authors designed the project, and contributed to the discussion and interpretation of the results. LR performed analytical calculations and numerical simulations, and wrote the manuscript.

During her doctorate, Lisa Rapp presented the research described in this thesis at the following scientific conferences and workshops:

- WEH Physics School “Model systems for understanding biological processes”
February 22-27, 2015 in Bad Honnef, Germany (Poster)
- DPG Spring Meeting
March 15-20, 2015 in Berlin, Germany (Poster)
- DPG Spring Meeting
March 6-11, 2016 in Regensburg, Germany (Talk)
- WEH Seminar “Patterns in Nature - Functions, Variations and Control”
October 9-12, 2016 in Bayreuth, Germany (Talk)
- Workshop “Physical Biology of Tissue Morphogenesis”
October 17-21, 2016 in Dresden, Germany (Poster)
- DPG Spring Meeting
March 19-24, 2017 in Dresden, Germany (Talk)
- DPG Spring Meeting
March 11-16, 2018 in Berlin, Germany (Talk)
- Conference “Self-Organization in Active Matter: from Colloids to Cells”
October 1-6, 2018 in Erice, Italy (Poster)

- Workshop “Advances in Pattern Formation: New Questions Motivated by Applications”
February 18-21, 2019 in Sede Boqer, Israel (Poster)
- DPG Spring Meeting
April 2, 2019 in Regensburg, Germany (Talk)

5. Attached publications

Pattern orientation in finite domains without boundaries

Lisa Rapp, Fabian Bergmann and Walter Zimmermann

EPL **113**, 28006 (2016)
(DOI: 10.1209/0295-5075/113/28006)

Reprinted with permission from the EPL Association

Pattern orientation in finite domains without boundaries

LISA RAPP, FABIAN BERGMANN and WALTER ZIMMERMANN

Theoretische Physik I, Universität Bayreuth - 95440 Bayreuth, Germany

received 24 October 2015; accepted in final form 4 February 2016

published online 18 February 2016

PACS 89.75.Kd – Patterns

PACS 87.18.-h – Biological complexity

PACS 47.20.-k – Fluid instabilities

Abstract – We investigate the orientation of nonlinear stripe patterns in finite domains. Motivated by recent experiments, we introduce a control parameter drop from supercritical inside a domain to subcritical outside without boundary conditions at the domain border. As a result, stripes align perpendicularly to shallow control parameter drops. For steeper drops, non-adiabatic effects lead to a surprising orientational transition to parallel stripes with respect to the borders. We demonstrate this effect in terms of the Brusselator model and generic amplitude equations.

 Copyright © EPLA, 2016

Introduction. – Pattern formation is central to the wealth of fascinating phenomena in nature. It occurs in a great variety of physical, chemical and living systems [1,2]. Examples include patterns in isotropic and anisotropic convection systems [3–7], chemical reactions [8,9] and biological systems [10–12], or environmental patterns [13].

In real systems, patterns emerge in finite areas or volumes. Consequently, spatially periodic patterns only contain a finite number of wavelengths. Along the system borders, the relevant fields have to obey boundary conditions that influence the pattern in different ways [3,14–25]. In isotropic systems, stationary patterns may be oriented perpendicularly to the boundaries [3,15]. In thermal convection, convection rolls align perpendicularly to side walls due to boundary conditions for the flow fields [17–19]. Boundary conditions at the side walls may also restrict the range of possible stable wave numbers of periodic patterns [20]. Traveling waves of finite wave number may be reflected at the boundaries leading to a number of interesting and complex phenomena [21–25].

However, finite systems can also be achieved when the fluxes and forces driving a pattern, the so-called control parameters, are sufficiently strong (supercritical) only in a subdomain of the system. In this case, no specific boundary conditions act on the fields at *control parameter drops* to subcritical values. Related to this are studies of ramps in quasi-one-dimensional systems [26], whereby smooth ramps may lead to wave number selection [26,27] and rapid parameter changes to pinning effects for spatially periodic patterns [28]. But the effects of restricting two dimensional patterns to a finite domain by control parameter

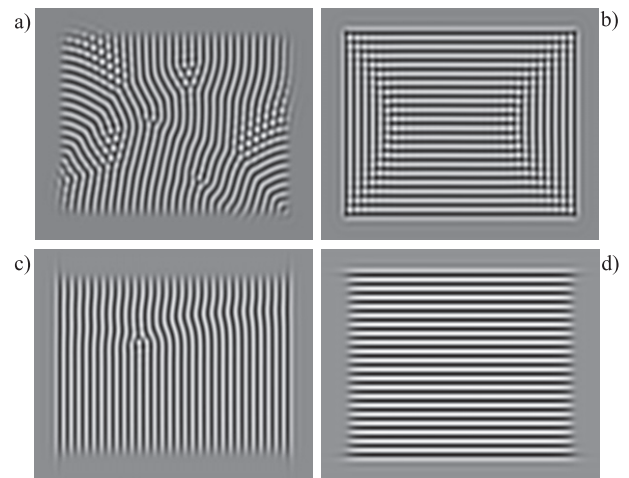


Fig. 1: Stripe patterns inside supercritical subdomains in the Brusselator model. The control parameter drops on different length scales $\delta_{x,y}$ along x and y from $\beta_m = 0.05$ to subcritical values in a wide vicinity: (a) $\delta_x = \delta_y = \lambda_c$, (b) $\delta_x = \delta_y = 0.32\lambda_c$, (c) $\delta_x = 0.32\lambda_c$, $\delta_y = 1.5\lambda_c$, (d) $\delta_x = 1.5\lambda_c$, $\delta_y = 0.32\lambda_c$.

drops have not been systematically investigated so far. Examples of pattern orientations resulting from different widths of the control parameter drops are shown in fig. 1 and explained in this work.

Recent experiments where pattern forming protein reactions take place in finite subdomains of substrates [29] belong to this class. Control parameter drops can also be designed in light-sensitive chemical reactions where illumination of the reaction cell suppresses pattern

formation [30,31]. If the illumination is only applied to a subdomain of the system, again no boundary conditions for the concentration fields are defined along the edge of the illumination mask.

We investigate how control parameter drops along the borders of a supercritical subdomain affect the orientation of stationary spatially periodic patterns when no boundary conditions for the fields are specified. We choose the Brusselator as a representative model system to study the influence of the control parameter drop width. This is complemented by studies of the so-called amplitude equations for supercritical bifurcations to spatially periodic patterns [3]. As a general description for this class of patterns, the conclusions drawn from the amplitude equations emphasize the universality of our results.

For large drop widths, we find that stripes align perpendicularly to the borders of the supercritical control parameter domain. By decreasing the length scale for the control parameter drop, we find a surprising orientational transition to stripes in parallel alignment. The analysis of the amplitude equations reveals additional non-adiabatic, resonance-like effects favouring parallel stripes.

Model systems and control parameter drop. –

Brusselator. The Brusselator is a common model for reaction-diffusion systems [32–35]. We use it as a prototype system for supercritical bifurcations to spatially periodic patterns (Turing patterns). It describes the non-linear behaviour of the concentration fields $u(x, y, t)$ and $v(x, y, t)$:

$$\partial_t u = \nabla^2 u + a - (b + 1)u + u^2 v, \quad (1a)$$

$$\partial_t v = D \nabla^2 v + bu - u^2 v, \quad (1b)$$

with the *control parameter* b and constant parameters a , D . These equations have the homogeneous fixed point solution

$$u_h = a, \quad v_h = b/a. \quad (2)$$

Turing patterns with the critical wave number q_c bifurcate from this basic state for control parameter values beyond its critical one b_c [34], where

$$b_c = (1 + a\eta)^2, \quad q_c = \sqrt{a\eta}, \quad (3)$$

and $\eta := \sqrt{1/D}$. The relative distance β of the control parameter from its critical value b_c is given by

$$b = b_c(1 + \beta), \quad (4)$$

i.e. $\beta_c = 0$. Hexagons are typical for the Brusselator near the onset of Turing patterns. But in this work, we consider the special case $D = a^2$ where stripes are preferred at the onset [35]. In this case, the critical wavelength of the stripes according to eq. (3) is $\lambda_c := 2\pi/q_c = 2\pi$. We choose $a = 4$ throughout this work.

Amplitude equations. The two concentration fields u and v may be combined to the vector field $\mathbf{w}(\mathbf{r}, t) = (u(\mathbf{r}, t), v(\mathbf{r}, t))$. We write spatially periodic stripes with the wave vector \mathbf{q}_c in the form [3,34]

$$\mathbf{w}(\mathbf{r}, t) = \mathbf{w}_h + A \tilde{\mathbf{w}} e^{i(\mathbf{q}_c \cdot \mathbf{r})} + A^* \tilde{\mathbf{w}}^* e^{-i(\mathbf{q}_c \cdot \mathbf{r})}, \quad (5)$$

where $\mathbf{w}_h = (u_h, v_h)$. Slow variations (compared to the wavelength λ_c) of the envelope $A(\mathbf{r}, t)$ can be described by a dynamical amplitude equation [3,36].

The Brusselator model is isotropic. Hence, in extended systems only the magnitude q_c of the critical wave vector \mathbf{q}_c for Turing stripes is fixed, but not its direction. Thus, all stripe orientations are equally likely at pattern onset. We consider the amplitude equations in two limits of stripe orientations: $\mathbf{q}_c = (q_c, 0)$ and $\mathbf{q}_c = (0, q_c)$, called parallel and perpendicular hereafter. The reduction method to amplitude equations, the so-called multiple scale analysis, is well established for supercritical bifurcations [3,36]. The generic amplitude equations for the two stripe orientations in the case of a small and constant control parameter β are

$$\partial_t A = \beta A + \mathcal{L}A - g|A|^2 A, \quad (6)$$

with

$$\mathcal{L} = \mathcal{L}_{\parallel}^2 := \xi_0^2 \left(\partial_x - \frac{i}{2q_c} \partial_y^2 \right)^2, \quad \text{for } \mathbf{q}_c = (q_c, 0), \quad (7a)$$

$$\mathcal{L} = \mathcal{L}_{\perp}^2 := \xi_0^2 \left(\partial_y - \frac{i}{2q_c} \partial_x^2 \right)^2, \quad \text{for } \mathbf{q}_c = (0, q_c). \quad (7b)$$

The coherence length ξ_0 and the nonlinear coefficient g for the Brusselator in the special case of $D = a^2$ are $\xi_0^2 = 1$ and $g = 3/(2a^2)$ [35].

Control parameter drop. We introduce the control parameter drop by assuming the spatially dependent control parameter $\beta(x, \delta_x)$:

$$\beta = \beta_0 + \frac{M}{2} \left[\tanh \left(\frac{x - x_l}{\delta_x} \right) - \tanh \left(\frac{x - x_r}{\delta_x} \right) \right]. \quad (8)$$

We assume $L := x_r - x_l \gg \lambda_c$ and $\beta_0 < 0$. M and β_0 are chosen such that the maximum value $\beta_m = \beta_0 + M$ is small and positive. Then $\beta(x, \delta_x)$ is supercritical in the subdomain $\bar{x}_l < x < \bar{x}_r$, where

$$\bar{x}_{l,r} = x_{l,r} \pm \frac{\delta_x}{2} \ln \left(\frac{-\beta_0}{M + \beta_0} \right), \quad (9)$$

and drops down to the subcritical value β_0 outside this domain. The steepness of the control parameter drop around $\bar{x}_{l,r}$ increases with decreasing values of the drop width δ_x .

For small values of δ_x , the control parameter $\beta(x, \delta_x)$ varies rapidly in a narrow range around $\bar{x}_{l,r}$. However, only the slowly (adiabatically) varying contributions to $\beta(x, \delta_x)$ affect the solutions of amplitude equations. The rapidly (non-adiabatically) varying part is smoothed out and must be treated separately. We therefore decompose

$\beta(x, \delta_x)$ into an adiabatic and non-adiabatic part. For this purpose, we introduce the slow length scale $\delta_A := 2\xi_0/\sqrt{\beta_m} > \delta_x$ and choose $\beta_0 = -\varepsilon$, $M = 2\varepsilon$ (where ε is positive and small). We then express the slowly varying contribution $B_0(x)$ via eq. (8) by choosing $\delta_x = \delta_A$:

$$B_0(x) = \beta(x, \delta_A). \quad (10)$$

The difference between $\beta(x, \delta_x)$ and $B_0(x)$ becomes small in the centre of $[x_l, x_r]$ and takes its largest values around $x_{l,r}$. We expand the rapidly varying difference $\beta(x, \delta_x) - B_0(x)$ into a series to obtain

$$\begin{aligned} \beta(x, \delta_x) = B_0(x) + \frac{M}{2} \sum_m \left\{ B_m^l(x) \sin[mq_c(x - x_l)] \right. \\ \left. + B_m^r(x) \sin[mq_c(x - x_r)] \right\}, \end{aligned} \quad (11)$$

where $m = n/N_L$, $n \in N$ and $N_L = L/\lambda_c$. The functions $B_m^{l,r}(x)$ are localised around $x_{l,r}$ and we choose a Gaussian for their representation:

$$B_m^{l,r}(x) = \hat{B}_m^{l,r} \exp\left[-\frac{(x - x_{l,r})^2}{\delta_{G,m}^2}\right]. \quad (12)$$

The Gaussian amplitudes $\hat{B}_m^{l,r}$ and their widths $\delta_{G,m}$ are determined via a correlation analysis. We calculate the correlation function between the rapidly varying part

$$\Delta\tilde{\beta}(x, \delta) = \tanh(x/\delta) - \tanh(x/\delta_A) \quad (13)$$

and the test function

$$f_m(x, \delta_{\text{test}}) = \frac{1}{\sqrt{\pi}\delta_{\text{test}}} e^{-x^2/\delta_{\text{test}}^2} \sin(mq_c x). \quad (14)$$

We then choose the Gaussian width $\delta_{G,m}$ to be the value of δ_{test} that maximises the correlation function. The amplitudes $\hat{B}_m^{l,r}$ are calculated via the overlap integral between $f_m(x, \delta_{G,m})$ and $\Delta\tilde{\beta}$. Figure 2(a) shows the contributions $\hat{B}_m^l := \varepsilon B_m^l(x) \sin(mq_c x)$ for $m = 1, 2$ in comparison to the full shape of $\beta(x, \delta_x)$. Both functions are localised around $x_l = 0$ and approach zero within a short range ($\ll \delta_A$) around the control parameter drop. The Gaussian amplitudes $\hat{B}_1^{l,r}$ and $\hat{B}_2^{l,r}$ decrease as a function of the drop width δ_x (fig. 2(b)). These non-adiabatic contributions vanish for $\delta_x > \delta_A$. The amplitude $\hat{B}_1^{l,r}$ is usually larger than $\hat{B}_2^{l,r}$, except in the limit of very small drop widths.

The patterns in fig. 1 are obtained for a rectangular supercritical subdomain of the control parameter in the form

$$\begin{aligned} \beta = \beta_0 + \frac{M}{4} \left[\tanh\left(\frac{x - x_l}{\delta_x}\right) - \tanh\left(\frac{x - x_r}{\delta_x}\right) \right] \\ \times \left[\tanh\left(\frac{y - y_b}{\delta_y}\right) - \tanh\left(\frac{y - y_t}{\delta_y}\right) \right]. \end{aligned} \quad (15)$$

Here, we introduced a second drop width δ_y to describe the additional spatial dependence of β in the y -direction. $\beta(x, y, \delta_x, \delta_y)$ is supercritical in the two-dimensional area $[\bar{x}_l, \bar{x}_r] \times [\bar{y}_b, \bar{y}_t]$.

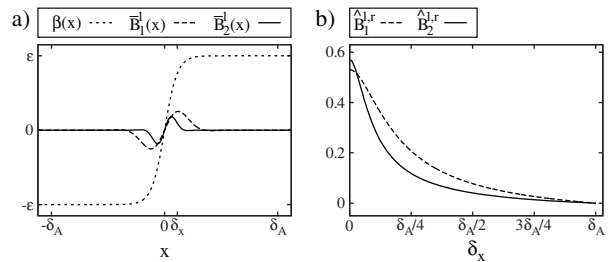


Fig. 2: (a) Contributions $\hat{B}_1^l(x)$ and $\hat{B}_2^l(x)$ to the control parameter drop $\beta(x, \delta_x)$ for $\delta_x = 0.11\delta_A$. (b) Gaussian amplitudes $\hat{B}_1^{l,r}$ and $\hat{B}_2^{l,r}$ of the localised amplitudes as a function of the drop width δ_x for $\varepsilon = 0.05$.

Non-adiabatic effects cause an orientational transition.

— We now include the control parameter drop into the amplitude equation using the decomposition given in eq. (11). The control parameter β in eq. (6) is replaced by the slowly (adiabatically) varying part $B_0(x)$ as given by eq. (10). The short-wavelength contributions $\propto B_m^{l,r}(x) \exp(imq_c x)$ with $m = 1, 2, 3, 4$ in eq. (11) cause additional (non-adiabatic) terms in the amplitude equation for parallel stripes [37]. It then takes the form

$$\begin{aligned} \partial_t A = B_0(x)A + \mathcal{L}_{\parallel}^2 A - g|A|^2 A \\ + \sum_{m=1}^4 \alpha_m B_m(x) (A^*)^{m-1}. \end{aligned} \quad (16)$$

Here, α_m are constant parameters depending on the respective system. The complex localised contributions $B_m(x)$ due to the control parameter drop are given by

$$B_m(x) = i \frac{M}{4} [B_m^l(x) e^{-imq_c x_l} - B_m^r(x) e^{-imq_c x_r}]. \quad (17)$$

The magnitudes of $B_1(x)$ and $B_2(x)$ are similar, as shown in fig. 2. The coefficient $B_2(x)$ reduces the threshold of the pattern onset [37]. $B_1(x)$ changes the supercritical bifurcation (in the case $B_1 = 0$) into an imperfect one [37,38] and, therefore, has a stronger impact than $B_2(x)$. The effects caused by $B_{3,4}(x)$ are restricted to the post-threshold regime and are much smaller than $B_{1,2}(x)$. Hence, they are neglected henceforth. Equation (16) can be derived from the functional

$$\begin{aligned} F_{\parallel} = \int dx dy \left[-B_0(x)|A|^2 + \frac{g}{2}|A|^4 + |\mathcal{L}_{\parallel} A|^2 \right. \\ \left. - \sum_{m=1}^2 \frac{\alpha_m}{m} (B_m(x)A^{*m} + B_m^*(x)A^m) \right] \end{aligned} \quad (18)$$

via $\partial_t A = -\delta F_{\parallel}/\delta A^*$. For the Brusselator in the case $D = a^2$, we find $\alpha_1 = 2a$ and $\alpha_2 = 5/3$.

The amplitude equation for perpendicular stripes with $\mathbf{q}_c = (0, q_c)$ is not affected by resonance contributions $\propto B_m$. It is described by eq. (6) with $\mathcal{L} = \mathcal{L}_{\perp}^2$ as given in eq. (7b) and the slowly varying control parameter

$\beta = B_0(x)$, cf. eq. (10). The related functional is

$$F_{\perp} = \int dx dy \left[-B_0(x)|A|^2 + \frac{g}{2}|A|^4 + |\mathcal{L}_{\perp}A|^2 \right]. \quad (19)$$

For small values of δ_x , the coefficients $B_{1,2}$ have considerable magnitude (fig. 2(b)). However, the related non-adiabatic effects only affect the amplitude equation for parallel stripes, cf. eq. (16). Due to the imperfect bifurcation, parallel stripes already have a finite amplitude below the bulk threshold $\beta_m = 0$, especially around $x_{l,r}$, where $B_{1,2}$ take the largest values. This finite amplitude A decreases the functional F_{\parallel} for parallel stripes with respect to F_{\perp} . Thus, for small values of δ_x , parallel stripes are preferred compared to perpendicular stripes.

For large values of δ_x , the non-adiabatic contributions $B_{1,2}$ become small and can be neglected (fig. 2(b)). In this case, the amplitude equations and the functionals for the two different stripe orientations only differ in the linear operator. These include different orders of derivatives in the x -direction: $|\partial_x A|^2$ in the functional for parallel stripes, eq. (18), and $|\partial_x^2 A|^2$ for perpendicular stripes, eq. (19). Thus, spatial variations of the amplitude $A(\mathbf{r}, t)$ affect the two functionals differently. The slow spatial variation of the control parameter $B_0(x)$ in the x -direction is reflected in a spatial variation of the amplitude $A(\mathbf{r}, t)$. This increases both functionals. However, due to the different orders of x -derivatives, the functional for perpendicular stripes has a lower value [3,39]. Therefore, perpendicular stripes will be preferred for large δ_x .

According to this reasoning, we predict stripes aligned perpendicular to the supercritical border for a large drop width δ_x and parallel for small δ_x . Therefore, we expect an orientational transition for medium values of δ_x . Note, for these considerations only the contributions B_0 , B_1 and B_2 to the decomposition in eq. (11) are taken into account. However, the predicted orientational transition of stripes is rather insensitive to these approximations as confirmed by simulations of the Brusselator in the next section.

Numerical results for the Brusselator. – In the previous part we found an orientational transition of stripe patterns by changing the width of control parameter drops. This prediction is based on a reasoning including approximations. Therefore, the effect is verified by simulations of the Brusselator model, cf. eqs. (1), with supercritical subdomains of width $L = 20\lambda_c$, embedded in larger subcritical domains with overall system sizes $l_{x,y}$. The model is solved using a common pseudospectral method with periodic boundary conditions [40] and $N_{x,y}$ modes, respectively. We choose $\beta_0 = -0.05$ and perturb the basic solution by small amplitude random noise.

For large widths δ_x of control parameter drops, *i.e.* slow variations of the control parameter, the preferred orientation of a stripe pattern is nearly perpendicular to the borders of the supercritical domain, *i.e.* $\mathbf{q} \sim (0, q_c)$, as shown in fig. 3 for $\delta_x = 5\lambda_c$. This confirms the prediction in terms of the amplitude equations in the previous section

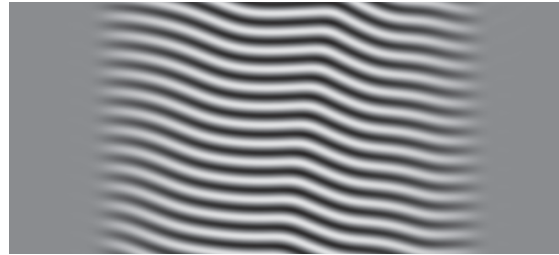


Fig. 3: Stripes favour a perpendicular orientation with respect to shallow control parameter drops ($\delta_x = 5\lambda_c$). Simulation of the Brusselator started at $\beta_m = 0.001$ and was slowly increased to $\beta_m = 0.05$. Parameters: $l_x = l_y = 50\lambda_c$, $N_x = N_y = 1024$. Note: only a cutout of the simulation is shown.

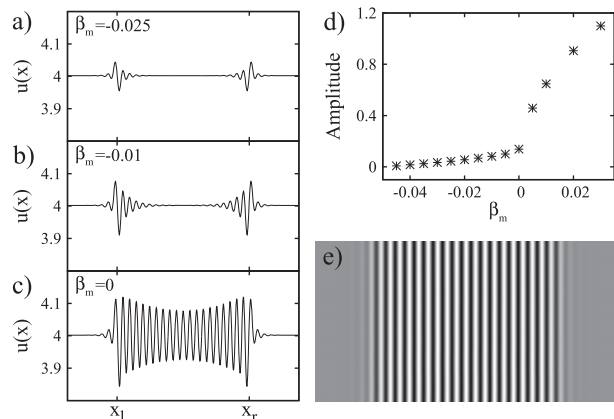


Fig. 4: Simulations of the Brusselator model with a narrow control parameter drop ($\delta_x = 0.5\lambda_c$). Cross-sections of the two-dimensional stripe pattern for (a) $\beta_m = -0.025$, (b) $\beta_m = -0.01$, (c) $\beta_m = 0$. (d) The stripe amplitude as a function of β_m implies an imperfect bifurcation. (e) Snapshot of the parallel stripes for $\beta_m = 0.02$. Simulation parameters: $l_x = 50\lambda_c$, $l_y = 25\lambda_c$, $N_x = 1024$, $N_y = 512$.

(for similar results for periodic modulations in extended systems see ref. [41]). Similar orientations are obtained for drop widths down to about $\delta_x \simeq \lambda_c$.

For small δ_x , *e.g.* $\delta_x = 0.5\lambda_c$, the stripes align parallelly to the borders of the supercritical range, *i.e.* $\mathbf{q}_c \sim (q_c, 0)$, as in fig. 4(e) for $\beta_m = 0.02$. Moreover, localised Turing stripe patterns of finite amplitude occur around the borders at $x_{l,r}$ already at subcritical values of β_m (see cross-sections in fig. 4(a) and (b)). For increasing β_m , they expand into the whole supercritical domain. At the bulk threshold $\beta_m = 0$ (fig. 4(c)) the stripes already have a finite amplitude throughout the range $[x_l, x_r]$. The maximum stripe amplitude of the stationary solution as a function of β_m is shown in the bifurcation diagram in fig. 4(d). The form of the bifurcation is imperfect, as expected from the analysis on the basis of the amplitude equations in the previous section.

The two different preferred stripe orientations for large $\delta_x = 5\lambda_c$ in fig. 3 and small $\delta_x = 0.5\lambda_c$ in fig. 4 clearly confirm an orientational transition of stripes in the

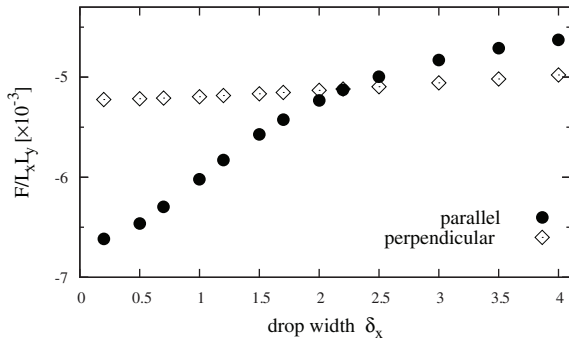


Fig. 5: Comparison of the functional for stripes as a function of the drop width δ_x with the stripe wave vector $\mathbf{q}_c = (0, q_c)$ (filled circles) and $\mathbf{q}_c = (q_c, 0)$ (open diamonds). Parameters: $\beta_0 = -0.05$, $M = 0.1$.

supercritical domain depending on the width of the control parameter drop along its border.

We can further restrict the domain size by varying the control parameter simultaneously along the x - and y -direction, cf. eq. (15). In these rectangular domains¹, one can combine different drop widths δ_x and δ_y to trigger different stripe orientations as shown by four examples in fig. 1. Combining, *e.g.*, large drop widths at the long side of the rectangle with small drop widths at the short side creates a remarkably uniform stripe pattern, cf. fig. 1(d). Using different combinations of $\delta_{x,y}$ may be a promising tool for designing Turing patterns in localised light-sensitive chemical reactions [42].

Orientational transition regime. – The orientational transition of stripes is deduced in terms of amplitude equations and confirmed by numerical simulations of the Brusselator model. The amplitude equations can be derived from the functionals, eqs. (18) and (19). Calculating these functionals as a function of the drop width allows to determine the preferred orientation for this δ_x . In the range where $F_\perp < F_\parallel$, a perpendicular stripe orientation is expected and vice versa. For this purpose, we perform simulations of the amplitude equations for the two stripe orientations using the aforementioned pseudospectral algorithm (simulation parameters: $l_x = l_y = 50\lambda_c$, $N_x = N_y = 1024$, $L = 20\lambda_c$, $\beta_0 = -0.05$, $\beta_m = 0.05$). When the solutions reach the stationary state, the functionals displayed in fig. 5 are calculated.

The functional corresponding to perpendicular stripes in eq. (19) does not contain the non-adiabatic contributions B_1 and B_2 to the control parameter drop. Regardless of the assumptions made for the justification of eq. (19) and the related amplitude equation, one may use $\beta(x, \delta_x)$ instead of $B_0(x)$. The functional then deviates only slightly from its constant value in the case of $B_0(x)$. In addition, fig. 5 shows that the functional with $\beta(x, \delta_x)$ is nearly independent of δ_x , *i.e.* stripes perpendicular to

¹Simulation parameters: $\beta_0 = -0.1$, $\beta_m = 0.05$, $L_x = 30\lambda_c$, $L_y = 20\lambda_c$, $l_x = 60\lambda_c$, $l_y = 50\lambda_c$, $N_x = N_y = 1024$.

the border of the supercritical range are rather insensitive to the width δ_x .

For parallel stripes, $\mathbf{q} = (q_c, 0)$, the resonance effects covered by B_1 (and B_2) are relevant and the associated functional is given in eq. (18). The two functionals for the two different stripe orientations are shown as a function of the drop width δ_x in fig. 5. For narrow control parameter drops, *i.e.* δ_x small, the functional for parallel stripes is significantly lower. Thus, the parallel orientation is preferred. However, the functional for parallel stripes strongly increases as a function of the drop width. The orientational transition takes place at the intersection of the two functionals. For larger δ_x , the perpendicular orientation of the stripes is preferred.

Summary and conclusions. – In this work, we identified and investigated a new class of finite pattern forming systems confined by control parameter drops from super- to subcritical values. These orient stripe patterns even without boundary conditions for the relevant fields. The stripe orientation depends on the width of the control parameter drops. We found a novel *orientational transition of stripe patterns* with respect to the borders as a function of the width of control parameter drops.

In light-sensitive chemical reaction-diffusion systems showing Turing patterns [30,31] the transition length between the patterns (supercritical) and the homogeneous state (subcritical) may be varied by the length of a smooth transition between illuminated and dark areas.

The Swift-Hohenberg (SH) model [43] is, besides the Brusselator a further paradigmatic model for studying the formation of spatially periodic patterns [2,3]. It behaves differently with respect to control parameter drops along the border of a supercritical domain. The basic state of the Brusselator is a function of the control parameter b , cf. eq. (2). Therefore, control parameter drops change the basic state of the bifurcation to Turing patterns. In the case of steep control parameter drops, the bifurcation to parallel stripes becomes imperfect, causing a different orientation than for smooth control parameter variations. In contrast, the basic state $u_h = 0$ of the SH model remains unchanged for spatially varying control parameters. The onset of periodic patterns is reduced but the bifurcation remains perfect. The local 1:2 resonance occurring in the case of a steep control parameter drop is not sufficient to change the stripe orientation like for the Brusselator. The same applies to the mean-field model for block copolymers (see, *i.e.*, [44]). Therefore, we do not find the aforementioned orientational transition of stripe patterns in the SH or the block copolymer model. However, in common systems where the basic state is also changed by control parameter variations, orientational transitions of stripe patterns are very likely.

Our results for stationary patterns may also be important for traveling waves that occur, for instance, in the cell biological MinE/MinD protein reaction on flat substrates [12,29]. To mimic the effects of cell confinement

in such extended experiments, reactive membranes were created in subdomains of the substrate [29,45]. In this way, the traveling waves are restricted to the range above the functionalised parts of the membrane. These may be interpreted as subdomains with a supercritical control parameter. In this experiment the traveling waves align perpendicularly to the borders of the functionalised area [29]. It is very likely that this orientational behaviour is again governed by generic principles similar to those discussed in this work and specific molecular reaction schemes or three-dimensional effects provide quantitative modifications [29,46,47]. Is the complex behavior of MinE/MinD oscillations in further restricted domains, as investigated recently in ref. [48], determined by the specific properties of the kinetic reaction models? Or do again generic principles of pattern formation play a leading role as described in this work?

* * *

Enlightening discussions with M. HILT and M. WEIß are gratefully acknowledged.

REFERENCES

- [1] BALL P., *The Self-Made Tapestry: Pattern Formation in Nature* (Oxford University Press, Oxford) 1998.
- [2] CROSS M. C. and GREENSIDE H., *Pattern Formation and Dynamics in Nonequilibrium Systems* (Cambridge University Press, Cambridge) 2009.
- [3] CROSS M. C. and HOHENBERG P. C., *Rev. Mod. Phys.*, **65** (1993) 851.
- [4] LAPPA M., *Thermal Convection: Patterns, Evolution and Stability* (Wiley, New York) 2010.
- [5] WEISS S., SEIDEN G. and BODENSCHATZ E., *New J. Phys.*, **14** (2012) 053010.
- [6] BODENSCHATZ E., ZIMMERMANN W. and KRAMER L., *J. Phys. (Paris)*, **49** (1988) 1875.
- [7] KRAMER L. and PESCH W., *Annu. Rev. Fluid Mech.*, **27** (1995) 515.
- [8] KAPRAL R. and SHOWALTER K. (Editors), *Chemical Waves and Patterns* (Springer, The Netherlands) 1995.
- [9] MIKHAILOV A. S. and SHOWALTER K., *Phys. Rep.*, **425** (2006) 79.
- [10] BEN-JACOB E., SHOCHET O., TENENBAUM A., COHEN I., CZIROK A. and VICSEK T., *Nature*, **368** (1994) 46.
- [11] KONDO S. and MIURA T., *Science*, **329** (2010) 1616.
- [12] LOOSE M., FISCHER-FRIEDRICH E., RIES J., KRUSE K. and SCHWILLE P., *Science*, **320** (2008) 789.
- [13] MERON E., *Nonlinear Physics of Ecosystems* (CRC Press, Boca Raton) 2015.
- [14] KRAMER L. and HOHENBERG P. C., *Physica D*, **13** (1984) 357.
- [15] GREENSIDE H. and COUGHRAN W. M., *Phys. Rev. A*, **30** (1984) 398.
- [16] KRAMER L., HOHENBERG P. C. and RIECKE H., *Physica D*, **15** (1985) 402.
- [17] CROSS M. C., *Phys. Fluids*, **25** (1982) 936.
- [18] BAJAJ K. M., MUKOLOBIEWIEZ N., CURRIER N. and AHLERS G., *Phys. Rev. Lett.*, **83** (1999) 5282.
- [19] CHIAM K.-H., PAUL M. R., CROSS M. C. and GREENSIDE H., *Phys. Rev. E*, **67** (2003) 056206.
- [20] CROSS M. C., DANIELS P. G., HOHENBERG P. C. and SIGGIA E. D., *J. Fluid Mech.*, **127** (1983) 155.
- [21] CROSS M. C., *Phys. Rev. Lett.*, **57** (1986) 2935.
- [22] CROSS M. C., *Phys. Rev. A*, **38** (1988) 3593.
- [23] MOSES E., FINEBERG J. and STEINBERG V., *Phys. Rev. A*, **35** (1987) 2757.
- [24] KOLODNER P. and SURKO C. M., *Phys. Rev. Lett.*, **61** (1988) 842; KOLODNER P., *Phys. Rev. A*, **44** (1991) 6448.
- [25] GARNIER N., CHIFFAUDEL A. and DAVIAUD F., *Physica D*, **174** (2003) 30.
- [26] KRAMER L., BEN-JACOB E., BRAND H. and CROSS M. C., *Phys. Rev. Lett.*, **49** (1982) 1891.
- [27] CROSS M. C., *Phys. Rev. A*, **29** (1984) 391.
- [28] RIECKE H., *Europhys. Lett.*, **2** (1986) 1.
- [29] SCHWEIZER J., LOOSE M., BONNY M., KRUSE K., MÖNCH I. and SCHWILLE P., *Proc. Natl. Acad. Sci. U.S.A.*, **109** (2012) 15283.
- [30] MUNUZURI A. P., DOLNIK M., ZHABOTINSKY A. M. and EPSTEIN I. R., *J. Am. Chem. Soc.*, **121** (1999) 8065.
- [31] DOLNIK M., BERENSTEIN I., ZHABOTINSKY A. M. and EPSTEIN I. R., *Phys. Rev. Lett.*, **87** (2001) 238301.
- [32] PRIGOGINE I. and LEFEVER R., *J. Chem. Phys.*, **48** (1968) 1695.
- [33] NICOLIS G. and PRIGOGINE I., *Self-Organization in Nonequilibrium Systems, from Dissipative Structures to Order through Fluctuations* (Wiley, New York) 1977.
- [34] WALGRAEF D., *Spatio-Temporal Pattern Formation* (Springer, New York) 1997.
- [35] PENA B. and PEREZ-GARCIA C., *Phys. Rev. E*, **64** (2001) 056213.
- [36] NEWELL A. C. and WHITEHEAD J. A., *J. Fluid Mech.*, **38** (1969) 279.
- [37] COULET P., *Phys. Rev. Lett.*, **56** (1986) 724.
- [38] PETER R. *et al.*, *Phys. Rev. E*, **71** (2005) 046212.
- [39] MALOMED B. A. and NEPOMNYASHCHY A. A., *Europhys. Lett.*, **21** (1993) 195.
- [40] KOPRIVA D. A., *Implementing Spectral Methods for Partial Differential Equations* (Springer, The Netherlands) 2009.
- [41] FREUND G., PESCH W. and ZIMMERMANN W., *J. Fluid Mech.*, **673** (2011) 318.
- [42] STEINBOCK O., KETTUNEN P. and SHOWALTER K., *Science*, **269** (1995) 1857.
- [43] SWIFT J. B. and HOHENBERG P. C., *Phys. Rev. A*, **15** (1977) 319.
- [44] WEITH V., KREKHOV A. and ZIMMERMANN W., *J. Chem. Phys.*, **139** (2013) 054908.
- [45] LAGNY T. J. and BASSEREAU P., *Interface Focus*, **5** (2015) 20150038.
- [46] HALATEK J. and FREY E., *Cell Rep.*, **1** (2012) 741.
- [47] HALATEK J. and FREY E., *Proc. Natl. Acad. Sci. U.S.A.*, **111** (2014) E1817.
- [48] WU F., VAN SCHIE B. G. C., KEYNER J. E. and DEKKER C., *Nat. Nanotechnol.*, **10** (2015) 719.

Size matters for nonlinear (protein) waves

Fabian Bergmann, Lisa Rapp and Walter Zimmermann

New J. Phys. **20**, 072001 (2018)

(DOI: [10.1088/1367-2630/aad457](https://doi.org/10.1088/1367-2630/aad457))

Reprinted without changes under a CC-BY License

**FAST TRACK COMMUNICATION**

Size matters for nonlinear (protein) wave patterns

OPEN ACCESSRECEIVED
19 June 2018REVISED
5 July 2018ACCEPTED FOR PUBLICATION
18 July 2018PUBLISHED
27 July 2018Fabian Bergmann¹, Lisa Rapp¹ and Walter Zimmermann

Theoretische Physik I, Universität Bayreuth, D-95440 Bayreuth, Germany

¹ Contributed equally to this work.E-mail: walter.zimmermann@uni-bayreuth.de**Keywords:** pattern formation, biological physics, reaction–diffusion, nonlinear wavesSupplementary material for this article is available [online](#)

Original content from this work may be used under the terms of the [Creative Commons Attribution 3.0 licence](#).

Any further distribution of this work must maintain attribution to the author(s) and the title of the work, journal citation and DOI.



Abstract

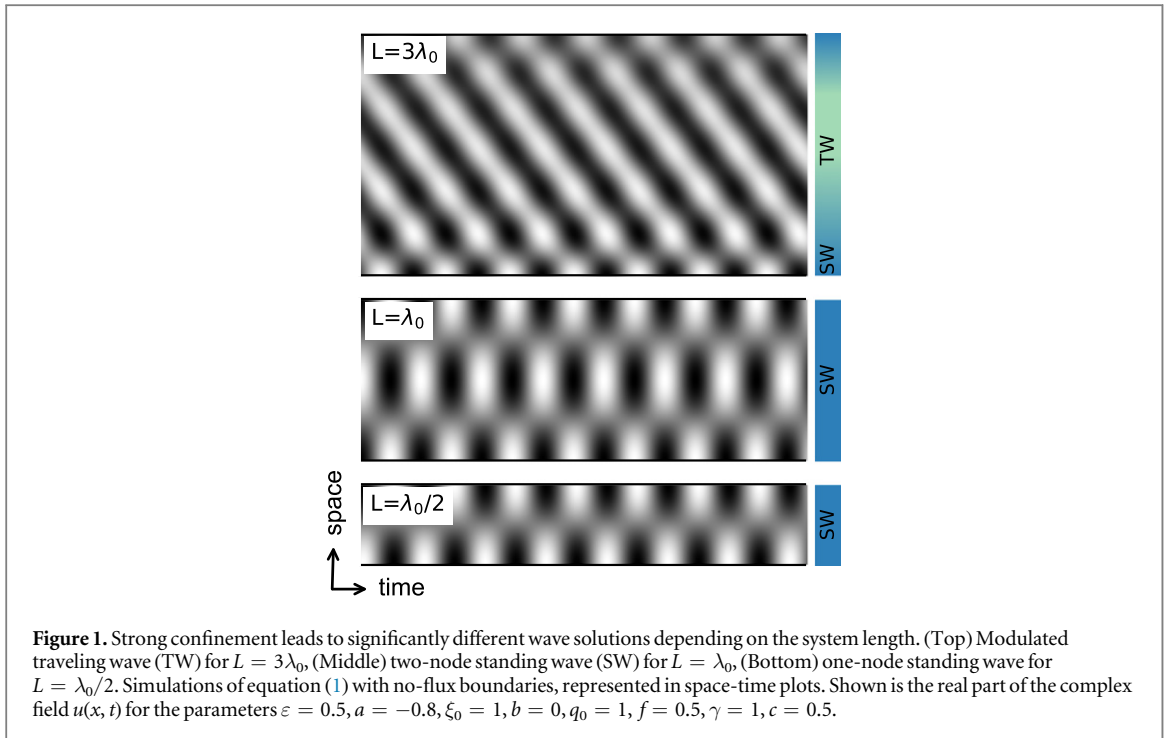
Pattern formation and selection are fundamental, omnipresent principles in nature—from small cells up to geological scales. In *E. coli* bacteria, for example, self-organized pole-to-pole oscillations of Min proteins—resembling a short standing wave—ensure correct positioning of the cell division site. The same biochemical reaction leads to traveling protein waves on extended membranes in *in vitro* experiments. Are these seemingly contradictory observations of system-spanning importance? We show that a transition of nonlinear traveling wave patterns to reflection-induced standing waves in short systems is a generic and robust phenomenon. It results from a competition between two basic phenomena in pattern formation theory. We confirm the generic findings for the cell-biological Min reaction and for a chemical reaction–diffusion system. These standing waves show bistability and adapt to varying system lengths similar as pole-to-pole oscillations in growing *E. coli*. Our generic results highlight key functions of universal principles for pattern formation in nature.

1. Introduction

A variety of fascinating patterns emerges spontaneously in a wealth of living or inanimate driven systems [1–13]. The esthetic appeal of these patterns is immediately apparent to all observers [1]. But universal principles of patterns and their importance in nature also attract researchers from many disciplines. They explore, for instance, the important functions patterns fulfill: self-organized patterns in biology guide size sensing [6], positioning of protein clusters [7], self-driven morphogenesis [8] and communication between species [10]. They furthermore enhance heat transport in fluid systems [3, 11] and are the basis of successful survival strategies for vegetation in water-limited systems [12–14].

Patterns include both stationary spatial structures such as stripes or hexagons, and dynamic structures like traveling waves [1–4]. Traveling waves occur in such different and prominent systems as thermally driven fluid convection [3, 15–18], electroconvection in nematic liquid crystals [19, 20] or the biochemical Min protein reaction on extended membranes [21, 22]. As these examples show, patterns emerge in diverse systems and are driven by very different mechanisms. Nevertheless, once stripes, hexagons or traveling waves have evolved, they often have certain universal properties described by pattern formation theory [2–4, 12].

In nature, patterns often evolve in the presence of domain boundaries—be it the walls of a convection cell, the finite size of a petri dish or the membrane enclosing the cytosol of a biological cell. These boundaries have a strong influence on the process of pattern formation. Stripe patterns, e.g., respond to system boundaries by adjusting their stripe orientation or selecting specific wavelengths [3, 23–25]. System boundaries in general break symmetries. Spatially varying parameters break them, too, and thus have similar effects [26–28]. The response of stationary periodic patterns to such symmetry breaking effects is broadly similar in different systems, i.e. independent of system details [3, 23, 25]. Traveling waves near boundaries show similar fascinating spatio-temporal behavior [15, 16, 29, 30]. However, the effects of strong confinement on nonlinear wave patterns have not yet been thoroughly examined.



In this work, we show that nonlinear traveling waves inevitably change into reflection-induced standing waves in sufficiently short, confined systems. Since this generic phenomenon relies on basic universal principles of pattern formation, we explore it at first within a minimal model for nonlinear traveling waves. The resulting system-spanning properties can then be transferred to related phenomena in nature: in the Min system, e.g., traveling waves form by coordinated attachment and detachment of Min proteins from the membrane. This protein system originates from *E. coli* bacteria where it plays an important role in the cell division process [31–33]: inside the rod-shaped *E. coli* bacteria, oscillating proteins shuttle between the two cell poles. Thereby, they ensure the positioning of the cell division site at the cell center. In *in vitro* experiments on the other hand, the same biochemical reaction leads to traveling waves on large extended membranes [21, 22]. A deeper understanding of generic properties of nonlinear waves in confinement will help to reconcile these seemingly contradictory observations.

2. Transition to reflection-induced standing waves in short systems

We first analyze the transition from nonlinear traveling waves in extended systems to reflection-induced standing waves in strongly confined systems using a generic model. ‘Strong confinement’ refers to short system lengths in the order of the preferred wavelength of the traveling wave. The model we use is the complex Swift–Hohenberg (CSH) model [4, 34–36],

$$\partial_t u(x, t) = (\varepsilon + ia)u - \xi_0^2(1 + ib)(q_0^2 + \partial_x^2)^2 u + if\partial_x^2 u - \gamma(1 + ic)|u|^2 u, \quad (1)$$

for the complex scalar field $u(x, t)$ in one spatial dimension. In extended systems and for $\varepsilon > 0$, this model shows traveling waves with a preferred wavelength $\lambda_0 = 2\pi/q_0$ over a wide range of parameters. We measure the system length L in units of λ_0 since it represents an intrinsic length scale of the problem.

Simulations of equation (1) with no-flux boundary conditions (see appendix A for details) for three different system lengths lead to the results shown in figure 1: depending on the system length, we get three significantly different wave solutions.

In moderately short systems ($L = 3\lambda_0$, top), we find a traveling wave pattern in the center (bulk) of the system. This resembles the traveling wave patterns that occur for the CSH model in large, quasi-unconfined systems. Two traveling wave directions, described by $u_R(x - \omega t)$ (traveling to the right) and $u_L(x + \omega t)$ (traveling to the left), are equally likely in extended pattern forming systems. In contrast to, e.g., light or sound waves, however, traveling waves in pattern forming systems are nonlinear. While light or sound waves are thus superimposable, two counter-propagating nonlinear waves compete with each other: one of the traveling wave directions is spontaneously selected, while the other is suppressed [3, 29]. But their confinement in finite systems introduces an additional effect: traveling waves are reflected at the boundaries of a finite system. The boundary conditions apply to the whole field $u(x, t)$ in equation (1), i.e. the incoming and reflected waves together.

Therefore, the sum $u_R + u_L$, has to match them at the system borders. This boundary coupling forces the incoming and reflected waves into coexistence in a finite neighborhood of the boundary. The resulting superposition of both wave directions leads to standing wave patterns. Further away in the bulk the nonlinear competition between both wave directions dominates and the reflected wave is damped by the predominant incoming traveling wave. The largest system in figure 1 (top) shows the interplay between both bulk and boundary effects. Reflection effects dominate very close to the top and bottom boundaries of the system. There, the incoming and reflected wave form a local standing wave. The extent of this standing wave depends on the distance ε from threshold and increases by decreasing ε . In the bulk region, however, wave competition prevails—the pattern resembles a traveling wave. By decreasing the system length L , the boundaries move closer together, i.e. the fraction of the system with significant superposition of incoming and reflected waves increases. Therefore, the boundary-induced reflection becomes more and more important. For sufficiently short systems—shorter than a critical length L_c —the reflection effect predominates the nonlinear competition in the whole system. As a result, standing waves become inevitable. Note that these standing waves are reflection-induced. In principle, standing wave solutions can be inherently stable. However, this is not the case here: in the CSH model, standing waves in extended systems are always unstable. Thus, the standing waves we find here are a direct consequence of the confinement. While this novel, reflection-induced transition from traveling to standing waves is generic, the critical length L_c depends on the chosen parameters and is specific to each system. The middle and bottom panel in figure 1 show simulations for $L = \lambda_0$ and $L = \lambda_0/2$, respectively. Both system lengths are below L_c leading to standing wave patterns. In the standing wave regime, the system length influences the number of standing wave nodes. For $L = \lambda_0$ (figure 1, middle) and similar lengths, we find a two-node standing wave. If only about half of the preferred wavelength fits into the system (e.g. $L = \lambda_0/2$, figure 1 bottom), the standing wave has a single node in the system center.

3. Length adaptability and bistability of nonlinear standing waves

The discovered reflection-induced standing waves in strongly confined systems are further characterized by exploring their linear stability. For stationary stripe patterns it is well known that they are stable for different wavenumbers in a finite band width. The basis of this multistability is the so-called Eckhaus stability band [37, 38]. Both fluid experiments [39, 40] and numerical analysis of different systems [27, 41] confirmed multistability for stationary patterns (e.g. stripes) in extended systems. The Eckhaus stability band also exists for traveling waves in unconfined systems [4, 17, 42, 43]. Do the standing waves we find in strongly confined systems also show multistable behavior? Does the confinement influence the stability band compared to spatially extended systems?

An analytical approximation of a standing wave solution of equation (1) is given by

$$u(x, t) = Fe^{-i\Omega t}[e^{iqx} + e^{-iqx}] = 2Fe^{-i\Omega t} \cos(qx), \quad (2)$$

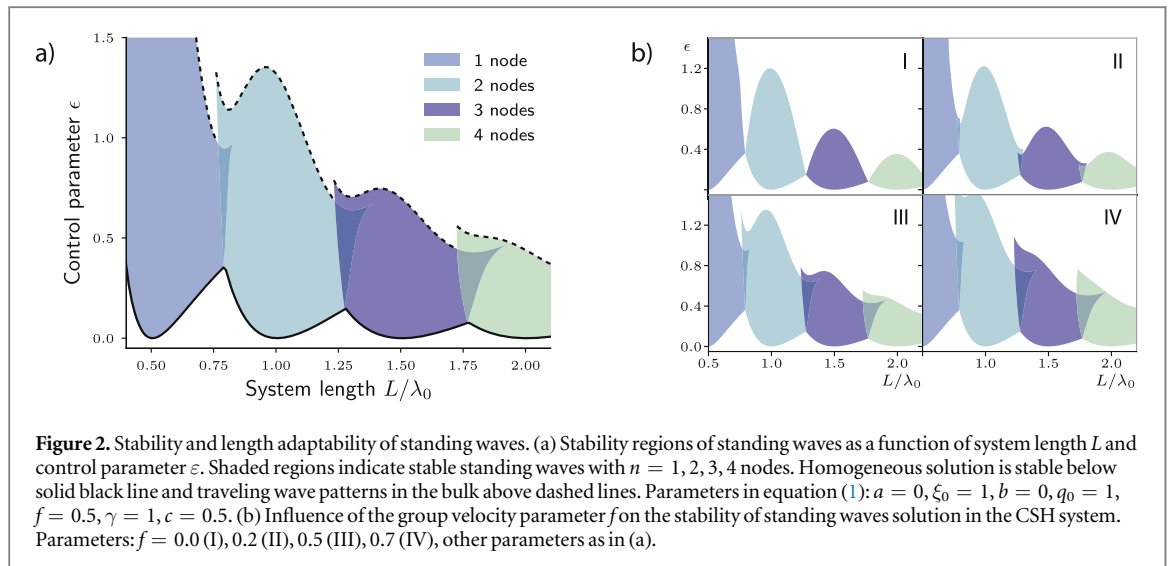
with amplitude F and frequency Ω ,

$$F^2 = \frac{1}{3\gamma}[\varepsilon - \xi_0^2(q_0^2 - q^2)^2], \quad (3)$$

$$\Omega = \frac{1}{\tau_0}[-a + \xi_0^2 b(q_0^2 - q^2)^2 + fq^2 + 3\gamma cF^2]. \quad (4)$$

Due to the no-flux boundaries, the wavenumber q is connected to the system length L via $q = n\pi/L$, where $n = 1, 2, 3 \dots$ is the number of nodes. This standing wave solution in equation (2) theoretically exists for $F^2 > 0$, i.e. for $\varepsilon > \xi_0^2(q_0^2 - q^2)^2$. In nature, e.g. in (bio)chemical reactions, the control parameter value, corresponding to ε in our model, is often fixed above the threshold of pattern formation. Then, standing waves only fulfill the aforementioned existence condition within a finite range of system lengths. Therefore standing waves with n nodes only exist in a certain length regime (existence band), located around $L = n\lambda_0/2$. In addition, existence ranges of standing waves with different numbers of nodes may overlap. Thus, for certain system lengths, multiple standing wave solutions (with different numbers of nodes) exist simultaneously. However, parameter ranges where patterns theoretically exist are not equivalent to the parameter ranges where they are stable. In fact, patterns are usually not stable throughout their whole existence range [3, 17, 27, 39–42]. By also analyzing the stability of standing waves, we thus identify the range in which to expect these solutions, especially in experiments (see SM is available online at stacks.iop.org/NJP/20/072001/mmedia for more details on the linear stability analysis).

Figure 2(a) shows the stability regions of standing wave solutions as a function of both system length L and the control parameter ε . For a given system length, standing waves with n nodes only exist for sufficiently large $\varepsilon > \xi_0^2(q_0^2 - (n\pi/L)^2)^2$. Below this threshold (black line in figure 2(a)), the homogeneous solution $u = 0$ is stable and no pattern occurs. The stability range of standing waves with n nodes is located around $L = n\lambda_0/2$ at

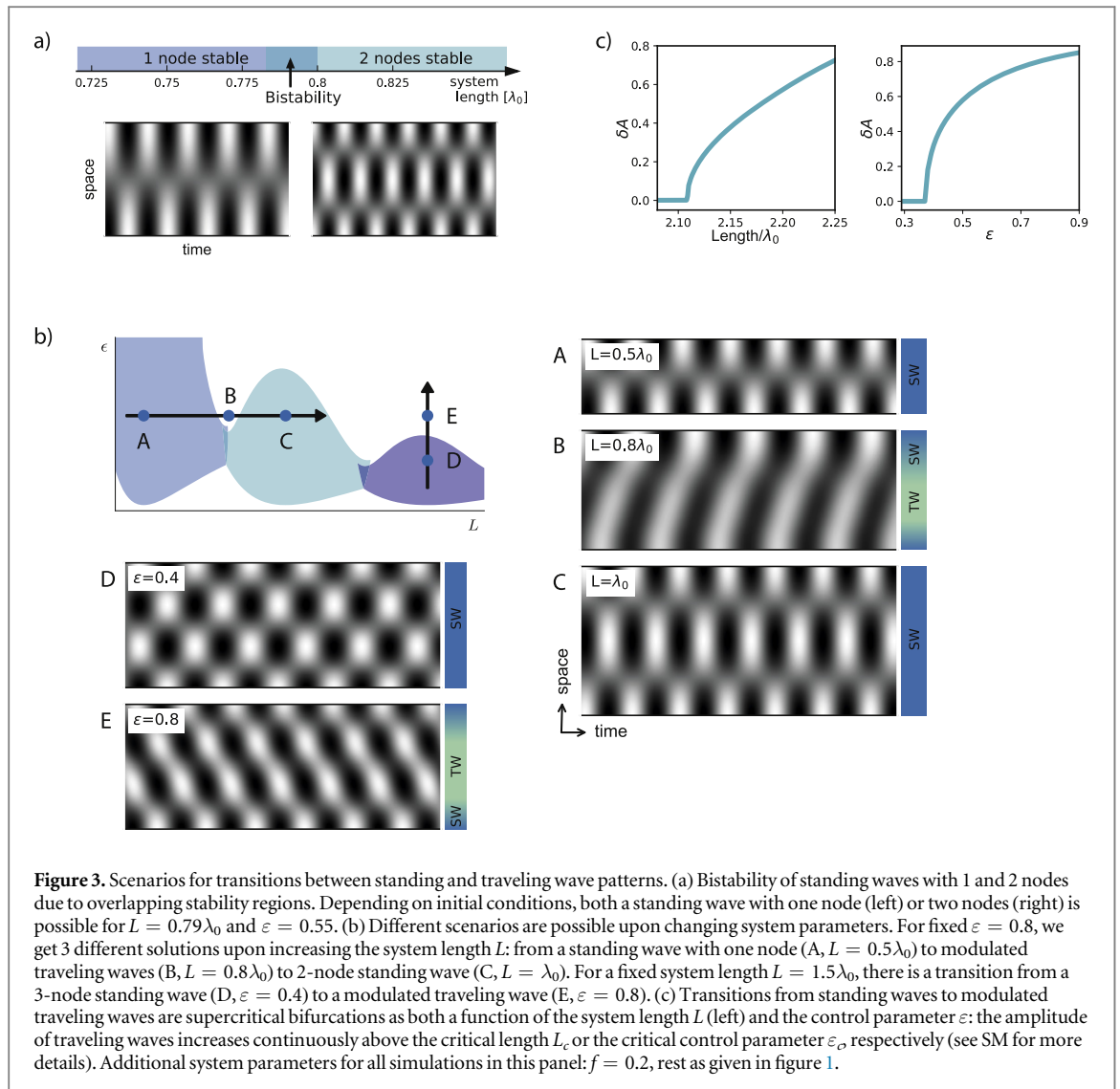


moderate values of ϵ . For $L = n\lambda_0/2$, the wavelength of the standing wave corresponds to the preferred wavelength λ_0 of the CSH model. For these ‘optimal’ system lengths, standing waves are stable over a large range of control parameter values. Nevertheless, we can deviate from these optimal lengths while still maintaining stable standing waves. This creates regions of stability in the ϵ - L -plane. These stability regions constitute the Eckhaus stability band for different number of nodes. We can now compare the width of the Eckhaus band to the width of the existence band for the standing waves. In extended systems, the waves are only stable in a subrange of their existence band. In contrast, in our confined systems close to the onset of pattern formation, the Eckhaus band spans the whole existence range (see figure 1 in SI). Additionally, adjacent stability regions may be large enough to overlap. In these cases, standing waves with both n and $n + 1$ nodes are stable. These overlapping stability regions therefore constitute areas of multistability. For large values of ϵ (above the dashed line in figure 2(a)), standing waves eventually lose stability. Simulations then show a transition to traveling wave patterns such as in figure 1 (top). The details of the stability regions also depend on the other parameters of the CSH model. Parameter f , e.g., which is connected to the group velocity of the waves, qualitatively changes the exact shape of the stability regions (figure 2(b)). As a result, the overlap between adjacent stability regions increases with increasing f . Other system parameters such as b or c only marginally change the stability of standing waves (figures S2 and S3) in confined systems. Importantly, however, the generic principle of a transition from traveling to standing waves in short systems remains qualitatively independent from system details.

Note that due to the shape of the stability regions, different scenarios are possible upon observing systems with increasing length: if we choose ϵ such that stability regions overlap, we expect direct transitions between standing waves with an increasing number of nodes (as seen in figure 1). Inside the overlap, there is bistability of standing waves with different numbers of nodes. Therefore, both types of standing waves are possible and the resulting pattern depends on initial conditions (see figure 3(a)). Notably, this provides the possibility for hysteresis. The transition from one to two nodes in a growing system, e.g., takes place at a different system length than the reverse transition in a shrinking system. For other values of ϵ , the different standing wave solutions are intersected by either the homogeneous solution (for small ϵ) or by traveling wave patterns (for larger ϵ , figures 3(b), (A)–(C)). In all cases, standing waves eventually lose stability for sufficiently large systems (after crossing the dashed line in figure 2(a)). For a fixed system length L , standing waves also lose their stability for sufficiently large ϵ (figures 3(b), (D)–(E)). These transitions to modulated traveling waves—both as a function of L and ϵ —take place in the form of supercritical (continuous) bifurcations (figure 3(c), see SM for details on how this was calculated).

4. Reflection-induced standing waves in models for a chemical reaction and the Min protein system

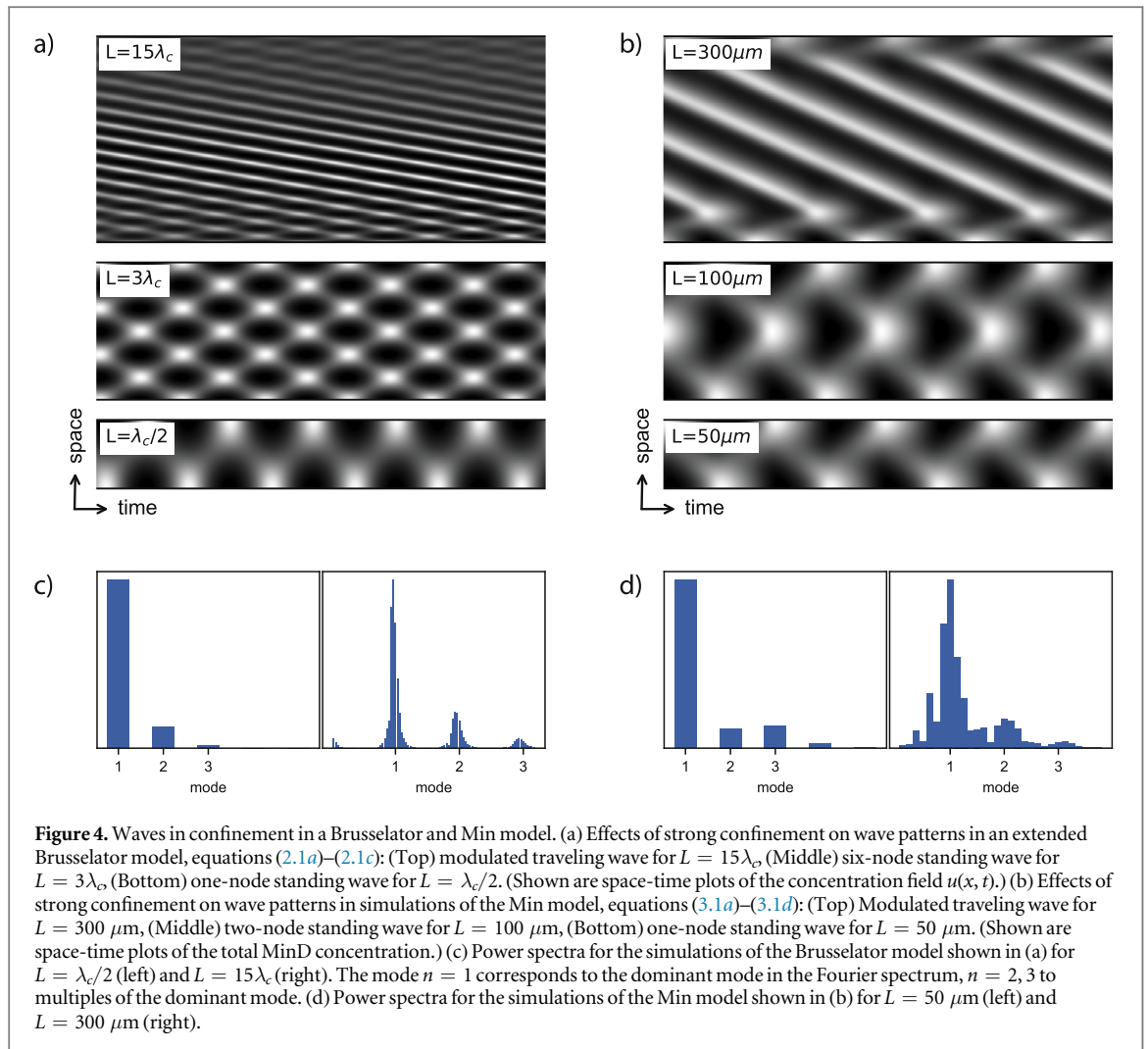
Minimal models such as the CSH model we study here for traveling waves are powerful tools to study system-spanning properties of self-organized patterns. System-specific models describing traveling waves are usually more complex than the CSH model. They are, e.g., often composed of several coupled nonlinear equations and/or include higher order nonlinearities (see e.g. [3, 21, 22, 44–49]). Moreover, traveling waves can occur far from the onset of pattern formation. Possible intricacies in these cases include secondary instabilities or anharmonic



wave profiles. Such effects can potentially overshadow the generic behavior of traveling waves under constraints discussed so far. Apart from these exceptions, however, even more complex scenarios often qualitatively follow generic principles extracted from minimal models. Thus, our results obtained from the generic CSH model help us to understand wave patterns in more complex systems.

We support this view by investigating the behavior of nonlinear traveling waves under confinement in two specific systems far from equilibrium. The first model describes the aforementioned Min protein oscillations in *E. coli* bacteria [21]. The second example is an extended Brusselator—a chemical reaction–diffusion model that forms traveling waves [49] (see appendices B and C for details on both models). As figures 4(a) and (b) show, the qualitative behavior of nonlinear waves in both of these models is very similar to the generic CSH model: in sufficiently strong confinement, traveling wave patterns inevitably change into reflection-induced standing waves. Depending on the system length, we also find standing wave patterns with different numbers of nodes. Note that both sets of simulations take place far beyond threshold. In this highly nonlinear regime the spatial dependence of the waves cannot be described by a single harmonic as in equation (2). Instead, they include higher harmonics—as seen in the Fourier spectra in figures 4(c) and (d).

Both models have a similar growth dispersion relation for perturbations of the homogeneous basic state as the CSH model—with a maximum at a finite wavenumber, while other modes are damped. Furthermore, the extended Brusselator shows a continuous bifurcation from the homogeneous state to traveling wave patterns—again, similar to the CSH model. On the basis of these common properties, the similar behavior of nonlinear waves in strong confinement were to be expected. Traveling waves in the Min model in figure 4(b) are even further from threshold and thus in the strongly nonlinear regime. Nevertheless, we find the same scenarios for the Min reaction as for the CSH model and the Brusselator. This further supports the generic nature of our predictions on reflection-induced standing waves.



Furthermore, our findings are not limited to no-flux boundary conditions. The reflection-induced transition to standing waves prevails for different boundary conditions such as fixed boundaries ($u|_{x=0} = u|_{x=L} = 0$). The only qualitative difference is the position of the standing wave nodes: they are shifted to the boundaries due to the vanishing fields at these points (see figure S4).

Nonlinear traveling waves in extended systems may be convectively unstable directly beyond threshold. This is also known as Benjamin–Feir instability [3, 4]. For the CSH model, this is the case in the parameter range $(b + f/4\xi_0^2 q_0^2)c > -1$. In this Benjamin–Feir unstable regime, spatio-temporally chaotic solutions are possible (above the transition to absolute instability). System size matters for spatio-temporal chaos as well: strong confinement and the related boundary-induced reflection can reestablish ordered standing waves (see figure S5).

5. Discussion

In our work we identified generic properties of nonlinear waves in very short systems, i.e. under strong spatial confinement. We found a universal and robust reflection-induced transition from traveling wave patterns in extended systems to standing waves in sufficiently short systems. Stability analysis shows that these standing waves can adapt to different system lengths. This corresponds to stability within a finite wavenumber band—a feature they share with stationary spatially periodic patterns or traveling waves [3, 17, 38–42]. They can also react to larger length variations by changing their number of nodes. We also find multistability of standing waves with different numbers of nodes in a system of the same length.

Our results obtained in terms of basic pattern formation theory show striking similarities to oscillating Min protein patterns. We hypothesize that basic generic properties of nonlinear wave patterns have a key function in the Min system. They may provide the missing link between pole-to-pole Min oscillations in short systems [31, 50–52] and traveling protein waves on extended membranes [21, 22]: the pole-to-pole oscillations in *E. coli* behave like standing waves originating from traveling waves confined to short systems. We also suggest that generic features of the reflection-induced standing waves such as length adaptability further contribute to the

regulation of cell division. This view is supported by experimental observations in the Min system: depending on bacteria length, the Min proteins also form standing waves with multiple nodes [31, 47, 53] or even traveling waves [47]. More importantly though, not only do living bacteria slightly differ in length, they also actively grow. To maintain accurate cell division at the cell center, the pole-to-pole oscillations must be robust over a range of cell sizes. The generic length adaptability of reflection-induced standing waves enables pole-to-pole oscillations in the Min system to adapt to the growing cell. In fact, *E. coli* maintain robust pole-to-pole oscillations even as they almost double in length prior to cell division. Continued cell growth to filamentous bacteria also allows for transitions between standing waves with different numbers of nodes or to traveling waves [33, 47, 53]. Even multistability of different wave patterns has recently been found in living *E. coli* [51].

Due to their generic nature, we expect our findings to be independent of system details. Our simulations of a Min protein model and an extended Brusselator substantiate this claim. While we analyzed one-dimensional systems in this work, we believe the basic principles also apply to two or three spatial dimensions: in sufficiently small multidimensional systems the boundary reflection of traveling waves along the long axis will likely overrule the bulk competition between counter-propagating traveling waves. Thus, system borders force them into reflection-induced standing waves—with slight system-specific modifications. Fluid experiments [17, 30] or oscillating chemical reactions guided by recent models as in [48, 49] are further suitable candidates to verify our results. Pattern formation theory applied to stationary 2d patterns recently provided important insights into pattern orientation with respect to spatial inhomogeneities or confinement [28, 54]. A combination of these approaches with our analysis of nonlinear traveling waves in confined systems is very promising. It may reveal further generic properties of nonlinear traveling waves and, e.g., provide additional guidance for experiments in 2d Min systems [50, 52]. This is particularly interesting for designing bottom-up approaches in synthetic biology to reconstitute cells [52]. In this context, our robust rules about nonlinear (protein) waves may present another puzzle piece to understand how nature controls crucial steps of life.

Acknowledgments

Support by the Elite Study Program Biological Physics is gratefully acknowledged.

Appendix A. Simulation methods

We solve the CSH model as well as the models for the Min oscillations and the chemical reactions below numerically by using a pseudo-spectral method with a semi-implicit time step (implicit Euler for the linear part of the equation, explicit Euler for the nonlinearities) (66). We calculate all spatial derivatives by transformation to a suitable function space depending on the boundary conditions. We use Fourier representations of the fields for periodic boundaries (i.e. in case of the CSH model $u|_{x=0} = u|_{x=L}$), a cosine transform for no-flux boundaries ($\partial_x u|_{x=0,L} = 0$) and a sine transform for vanishing fields at the boundary ($u|_{x=0,L} = 0$), where L is the system length.

Appendix B. Oscillating chemical reaction

As a model for a pattern forming chemical reaction, we use an extended Brusselator model as proposed by Yang *et al* [49]. The Brusselator is a well-known prototype for reaction–diffusion systems. Typically, this system is a two-component activator-inhibitor model with a bifurcation to Turing patterns or homogenous Hopf oscillations. The model by Yang *et al* extends the Brusselator by a third component. The dynamics of the three concentration fields u , v and w are given by:

$$\partial_t u = D_u \partial_x^2 u + a - (b + 1)u + u^2 v - cu + dw, \quad (2.1a)$$

$$\partial_t v = D_v \partial_x^2 v + bu - u^2 v, \quad (2.1b)$$

$$\partial_t w = D_w \partial_x^2 w + cu - dw. \quad (2.1c)$$

We choose $a = 0.8$, $c = 2$, $d = 1$, $D_u = 0.01$, $D_v = 0$ and $D_w = 1$. We consider b the control parameter of the system. The homogeneous solution ($u_h = a$, $v_h = b/a$, $w_h = ac/d$) becomes unstable towards traveling waves at the critical value $b_c = 3.076$. The intrinsic wavelength of the traveling wave pattern above threshold is $\lambda_c \approx 9.5$. We perform our simulations close to pattern onset, for $b = b_c(1 + \varepsilon)$ where $\varepsilon = 0.005$. The onset of the Turing instability (i.e. of stationary periodic patterns) tends to infinity for $D_v \rightarrow 0$. By choosing $D_v = 0$, we thereby eliminate any competition between traveling waves and Turing structures.

Appendix C. Min oscillation model

As a representative model for the Min oscillations shown in figure 4, we consider the model given by equations (3.1a)–(3.1d) as proposed by Loose *et al* [22] (see also equations [1]–[4] in their supplementary information). This model describes the dynamics of both MinD and MinE in the cytosol (c_D and c_E , respectively), the MinD concentration on the membrane c_d and the concentration of MinD/MinE complexes on the membrane c_{de} :

$$\partial_t c_D = D_D \partial_x^2 c_D + \omega_{de} c_{de} - c_D (\omega_D + \omega_{dD} c_d), \quad (3.1a)$$

$$\partial_t c_E = D_E \partial_x^2 c_E + \omega_{de} c_{de} - c_E c_d (\omega_E + \omega_{eE} c_{de}^2), \quad (3.1b)$$

$$\partial_t c_d = D_d \partial_x^2 c_d + c_D (\omega_D + \omega_{dD} c_d) - c_E c_d (\omega_E + \omega_{eE} c_{de}^2), \quad (3.1c)$$

$$\partial_t c_{de} = D_{de} \partial_x^2 c_{de} + c_E c_d (\omega_E + \omega_{eE} c_{de}^2) - \omega_{de} c_{de}. \quad (3.1d)$$

For the simulation shown in figure 4 we choose the parameters as suggested in [22]: $D_D = D_E = 60 \mu\text{m}^2 \text{s}^{-1}$, $D_d = 1.2 \mu\text{m}^2 \text{s}^{-1}$, $D_{de} = 0.4 \mu\text{m}^2 \text{s}^{-1}$, $\omega_{de} = 0.029 \text{s}^{-1}$, $\omega_D = 2.9 \cdot 10^{-4} \text{s}^{-1}$, $\omega_{dD} = 4.8 \cdot 10^{-8} \mu\text{m}^2 \text{s}^{-1}$, $\omega_E = 1.9 \cdot 10^{-9} \mu\text{m}^2 \text{s}^{-1}$, $\omega_{eE} = 2.1 \cdot 10^{-20} \mu\text{m}^6 \text{s}^{-1}$. We choose a total MinD concentration of $c_{D,\text{tot}} = c_D + c_d + c_{de} = 3.6 \cdot 10^6 \mu\text{m}^{-2}$, and a total MinE concentration of $c_{E,\text{tot}} = c_E + c_e + c_{de} = 5.8 \cdot 10^6 \mu\text{m}^{-2}$. In large, quasi-unconfined systems this leads to traveling waves with a typical wavelength $\lambda_{\text{min}} \approx 71 \mu\text{m}$.

References

- [1] Ball P 1998 *The Self-Made Tapestry: Pattern Formation in Nature* (Oxford: Oxford University Press)
- [2] Cross M C and Greenside H 2009 *Pattern Formation and Dynamics in Nonequilibrium Systems* (Cambridge: Cambridge University Press)
- [3] Cross M C and Hohenberg P C 1993 Pattern formation outside of equilibrium *Rev. Mod. Phys.* **65** 851
- [4] Aranson I and Kramer L 2002 The world of the complex Ginzburg–Landau equation *Rev. Mod. Phys.* **74** 99
- [5] Kondo S and Miura T 2010 Reaction–diffusion model as a framework for understanding biological pattern formation *Science* **329** 1616
- [6] Lander A D 2011 Pattern, growth, and control *Cell* **144** 955
- [7] Murray S M and Sourjik V 2017 Self-organization and positioning of bacterial protein clusters *Nat. Phys.* **13** 1006
- [8] Sasai Y 2013 Cytosystems dynamics in self-organization of tissue architecture *Nature* **493** 318
- [9] Kondo S and Asai R 1995 A reaction–diffusion wave on the skin of the marine angelfish *Pomacanthus* *Nature* **376** 786
- [10] Singh A P and Nüsslein-Volhard C 2015 Zebrafish stripes as a model for vertebrate colour pattern formation *Curr. Biol.* **25** R81
- [11] Lappa M 2009 *Thermal Convection: Patterns, Evolution and Stability* (New York: Wiley)
- [12] Meron E 2015 *Nonlinear Physics of Ecosystems* (Boca Raton, FL: CRC Press)
- [13] Meron E 2012 Pattern-formation approach to modelling spatially extended ecosystems *Ecol. Modelling* **234** 70
- [14] Getzin S, Yizhaq H, Bell B, Erickson T E, Postle A, Katra I, Tzuk O, Zelnik Y R, Wiegand K and Meron E 2016 Discovery of fairy circles in australia supports self-organization theory *Proc. Natl Acad. Sci. USA* **113** 3551
- [15] Moses E, Fineberg J and Steinberg V 1987 Multistability and confined traveling-wave patterns in a convecting binary mixture *Phys. Rev. A* **35** 2757
- [16] Heinrichs R, Ahlers G and Cannell D S 1987 Traveling waves and spatial variation in the convection of a binary mixture *Phys. Rev. A* **35** 2761
- [17] Kolodner P 1992 Extended states of nonlinear traveling-wave convection. I. The Eckhaus instability *Phys. Rev. A* **46** 6431
- [18] Schöpf W and Zimmermann W 1993 Convection in binary fluids: amplitude equations, codimension-2 bifurcation, and thermal fluctuations *Phys. Rev. E* **47** 1739
- [19] Rehberg I, Rasenat S, Fineberg J, de la Torre Juárez M and Steinberg V 1988 Temporal modulation of traveling waves *Phys. Rev. Lett.* **61** 2449
- [20] Kramer L and Pesch W 1995 Convection instabilities in nematic liquid crystals *Annu. Rev. Fluid Mech.* **27** 515
- [21] Loose M, Fischer-Friedrich E, Ries J, Kruse K and Schwille P 2008 Spatial regulators for bacterial cell division self-organize into surface waves *in vitro Science* **320** 789
- [22] Schweizer J, Loose M, Bonny M, Kruse K, Mönch I and Schwille P 2012 Geometry sensing by self-organized protein patterns *Proc. Natl Acad. Sci. USA* **109** 15283
- [23] Cross M C 1982 Boundary conditions on the envelope function of convective rolls close to onset *Phys. Fluids* **25** 936
- [24] Kramer L and Hohenberg P C 1984 Effects of boundaries on periodic structures *Physica D* **13** 352
- [25] Greenside H S and Coughran W M 1984 Nonlinear pattern formation near the onset of Rayleigh–Bénard convection *Phys. Rev. A* **30** 398
- [26] Kramer L, Ben-Jacob E, Brand H and Cross M C 1982 Wavelength selection in systems far from equilibrium *Phys. Rev. Lett.* **49** 1891
- [27] Riecke H and Paap H G 1986 Stability and wave-vector restriction of axisymmetric Taylor vortex flow *Phys. Rev. A* **33** 547
- [28] Rapp L, Bergmann F and Zimmermann W 2016 Pattern orientation in finite domains without boundaries *Europhys. Lett.* **113** 28006
- [29] Cross M C 1988 Structure of nonlinear traveling-wave states in finite geometries *Phys. Rev. A* **38** 3593
- [30] Garnier N, Chiffaudel A and Daviaud F 2003 Nonlinear dynamics of waves and modulated waves in 1d thermocapillary flows. II. convective/absolute transitions *Physica D* **174** 30
- [31] Raskin D M and de Boer P A J 1999 Rapid pole-to-pole oscillation of a protein required for directing division to the middle of *Escherichia coli* *Proc. Natl Acad. Sci. USA* **96** 4971
- [32] Lutkenhaus J 2007 Assembly dynamics of the bacterial MinCDE system and spatial regulation of the Z ring *Annu. Rev. Biochem.* **76** 539
- [33] Loose M, Kruse K and Schwille P 2011 Protein self-organization: lessons from the min system *Annu. Rev. Biophys.* **40** 315
- [34] Malomed B A 1984 Nonlinear waves in nonequilibrium systems of the oscillatory type, part I *Physik B* **55** 241
- [35] Aranson I and Tsimring L 1995 Domain walls in wave patterns *Phys. Rev. Lett.* **75** 3273

- [36] Gelens L and Knobloch E 2011 Traveling waves and defects in the complex Swift–Hohenberg equation *Phys. Rev. E* **84** 056203
- [37] Eckhaus V 1965 *Studies in Nonlinear Stability Theory* (Berlin: Springer)
- [38] Kramer L and Zimmermann W 1985 On the Eckhaus instability for spatially periodic patterns *Physica D* **16** 221
- [39] Lowe M and Gollub J P 1985 Pattern selection near the onset of convection: the Eckhaus instability *Phys. Rev. Lett.* **55** 2575
- [40] Dominguez-Lerma M A, Cannell D S and Ahlers G 1986 Eckhaus boundary and wave-number selection in rotating Couette–Taylor flow *Phys. Rev. A* **34** 4956
- [41] Zimmermann W and Kramer L 1985 Wavenumber restriction in the buckling instability of a rectangular plate *J. Phys.* **46** 343
- [42] Janiaud B, Pumir A, Bensimon D, Croquette V, Richter H and Kramer L 1992 The Eckhaus instability for traveling waves *Physica D* **55** 269
- [43] Liu Y and Ecke R E 1997 Eckhaus–Benjamin–Feir instability of rotating convection *Phys. Rev. Lett.* **78** 4391
- [44] Howard M, Rutenberg A D and de Vet S 2001 Dynamic compartmentalization of bacteria: accurate division in *E. coli* *Phys. Rev. Lett.* **87** 278102
- [45] Meinhardt H and de Boer P A J 2001 Pattern formation in *Escherichia coli*: a model for the pole-to-pole oscillations of Min proteins and the localization of the division site *Proc. Natl Acad. Sci. USA* **98** 14202
- [46] Halatek J and Frey E 2012 Highly canalized MinD transfer and MinE sequestration explain the origin of robust MinCDE-protein dynamics *Cell Reports* **1** 741
- [47] Bonny M, Fischer-Friedrich E, Loose M, Schwille P and Kruse K 2013 Membrane binding of MinE allows for a comprehensive description of min-protein pattern formation *PLoS Comput. Biol.* **9** e1003347
- [48] Bánsági T, Vanag V K and Epstein I R 2012 Two- and three-dimensional standing waves in a reaction–diffusion system *Phys. Rev. E* **86** 045202
- [49] Yang L, Dolnik M, Zhabotinsky A M and Epstein I R 2002 Pattern formation arising from interactions between Turing and wave instabilities *J. Chem. Phys.* **117** 7259
- [50] Wu F, van Schie B G C, Keymer J E and Dekker C 2015 Symmetry and scale orient Min protein patterns in shaped bacterial sculptures *Nat. Nanotechnol.* **10** 719
- [51] Wu F, Halatek J, Reiter M, Kingma E, Frey E and Dekker C 2016 Multistability and dynamic transitions of intracellular protein patterns *Mol. Syst. Biol.* **12** 873
- [52] Zieske K and Schwille P 2014 Reconstitution of self-organized protein gradients as spatial cues in cell-free systems *eLife* **3** e03949
- [53] Fischer-Friedrich E, Meacci G, Lutkenhaus J, Chaté H and Kruse K 2010 Intra- and intercellular fluctuations in Min-protein dynamics decrease with cell length *Proc. Natl Acad. Sci. USA* **107** 6134
- [54] Hiscock T W and Megason S G 2015 Orientation of Turing-like patterns by Morphogen gradients tissue anisotropies *Cell Syst.* **1** 408

Polarity bias in systems with broken up-down symmetry

Lisa Rapp, Fabian Bergmann and Walter Zimmermann

Polarity bias in systems with broken up-down symmetry

Lisa Rapp,¹ Fabian Bergmann,¹ and Walter Zimmermann¹

¹*Theoretische Physik I, Universität Bayreuth, 95440 Bayreuth, Germany*

(Dated: April 3, 2019)

A model for selforganization of bacterial protein clusters was presented recently [Nat. Phys. **13**, 1006 (2017)]. In this model, in the great majority of cases, a single protein cluster will be positioned in the center of the cell. Maximum density at the boundaries occurs far less likely even though for symmetry reasons the two solutions should be equivalent. By studying generic models of pattern formation, we found that broken up-down-symmetries in combination with strong spatial confinement are the generic basis of this observed polarity bias.

I. INTRODUCTION

Living systems require high levels of complexity and (self-)organization [1–3]. Complex structural components interact in a series of intricate processes to create the machinery of life - often displaying astonishing precision and robustness. Pattern formation is a part of nature’s toolbox to implement some of these processes [4–6]. Some of the many examples include embryonic pattern formation [7], cell polarization [1, 8], collective behavior in multicellular organisms such as the slime mold *Dictyostelium discoideum* [9–11], skin patterning [12, 13], the placement of hair follicles [14] or positioning of the cell division site in *E. coli* via the Min protein system [15–17].

A recent publication dealt with the question of precise positioning of protein clusters within cells [18]. They found that protein clusters show a clear bias to being positioned in the center of the system. A single protein concentration peak is unlikely to occur at the boundaries of the system. This is surprising since due to the symmetry of the system, the phase of the solution is a priori not fixed.

In this work, we give insights into the generic basis of these observations. We study minimal models of pattern formation in very small systems - mimicking the strong spatial confinement of protein clusters in cells. We assess the minimal requirements to recreate the polarity bias observed in the protein cluster model.

II. CHARACTERISTICS OF THE PROTEIN CLUSTERING MODEL

The protein clustering model presented in [18] describes the dynamics of a two-’species’ system in which one protein species only exists on the surface of a membrane (v_m), while the second protein species exists in a cytosolic (u_c) and a membrane-bound state (u_m). The

dynamic equations are given by

$$\begin{aligned} \partial_t u_m = & D_{u_m} \partial_x^2 u_m - \alpha u_m - \beta u_m v_m^2 \\ & + \gamma v_m + \epsilon u_c - \delta u_m, \end{aligned} \quad (1a)$$

$$\begin{aligned} \partial_t v_m = & D_{v_m} \partial_x^2 v_m + \alpha u_m + \beta u_m v_m^2 \\ & - \gamma v_m - \delta' v_m, \end{aligned} \quad (1b)$$

$$\partial_t u_c = D_{u_c} \partial_x^2 u_c - \epsilon u_c + \delta u_m + \delta' v_m. \quad (1c)$$

The rates ϵ , δ and δ' describe transitions between the membrane and the cytosol, α and γ are linear transition rates between the two states at the membrane, and β is a nonlinear reaction rate. Note that the reaction terms are chosen such that the total number of proteins in the system is conserved.

A homogeneous solution of Eqs. (1) is $(\tilde{u}_m, \tilde{v}_m, \tilde{u}_c)$, where \tilde{v}_m is the solution of the 3rd order polynomial

$$\tilde{v}_m^3 - a_2 \tilde{v}_m^2 + a_1 \tilde{v}_m - a_0 = 0, \quad (2)$$

with

$$a_2 = \frac{\beta \epsilon}{\epsilon + \delta} c_0, \quad (3)$$

$$a_1 = \frac{(\gamma + \delta' + \alpha)\epsilon + (\delta + \alpha)\delta' + \delta\gamma}{\beta(\epsilon + \delta')}, \quad (4)$$

$$a_0 = \frac{\epsilon \alpha}{\beta(\epsilon + \delta')} c_0, \quad (5)$$

and

$$\tilde{u}_m = \frac{\epsilon}{\epsilon + \delta} c_0 - \frac{\epsilon + \delta'}{\epsilon + \delta} \tilde{v}_m, \quad (6)$$

$$\tilde{u}_c = c_0 - \tilde{u}_m - \tilde{v}_m, \quad (7)$$

and c_0 is the total protein concentration:

$$c_0 = \tilde{u}_m + \tilde{v}_m + \tilde{u}_c. \quad (8)$$

We analyze the stability of the homogeneous state by adding small perturbations and solving the linearized model equations via an ansatz $\propto \exp(\sigma t + i q x)$. The resulting eigenvalue problem determines the perturbation growth rate σ . Using the total protein concentration c_0 as the control parameter in the system, we generally find two types of dispersion relations $\sigma(q)$: A finite k -instability where the growth rate is positive in a range

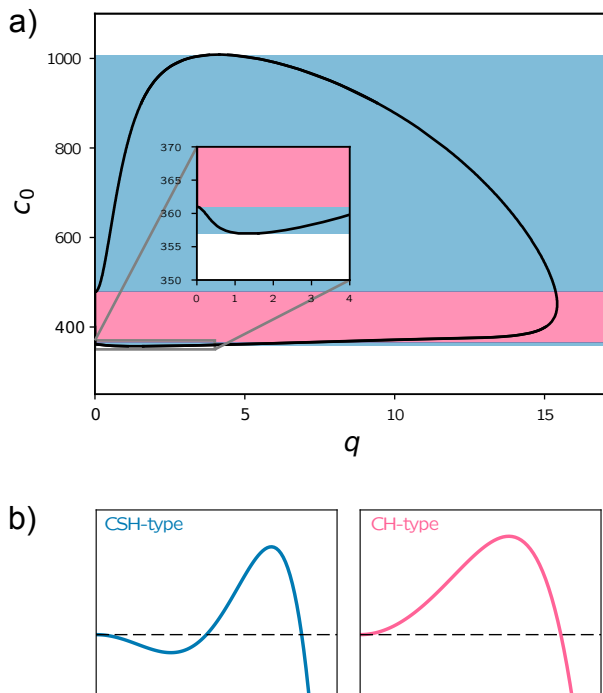


FIG. 1. a) Linear stability of the homogeneous basic state: perturbation growth rate σ is positive within the black line. Shading indicates the type of dispersion relation $\sigma(q)$ as sketched in b) CSH-type (blue), CH-type (pink).

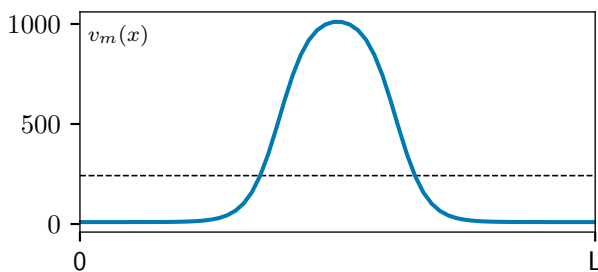


FIG. 2. Stationary profile of the concentration field $v_m(x)$ from simulations of Eqs. 1. Parameters as given in [18].

of finite wavenumbers, and a long-wavelength instability where the band of unstable wavenumbers extends down to $q = 0$. We call these dispersion relations CSH-type and CH-type, respectively, after the prototypical pattern formation models with the same type of instability - the conserved Swift-Hohenberg (CSH) model [19] and the Cahn-Hilliard (CH) model [20]. Figure 1 shows the linear stability as a function of the total protein concentration c_0 . The growth rate σ is positive within the black line. The colored shading indicates the dispersion relation type introduced above and as sketched in Fig. 1b. The important conclusion from this linear stability anal-

ysis is that the primary instability in the system is of the finite wavelength (CSH) type. While the long-wavelength instability does exist for a range of total protein concentrations, the homogeneous basic state first becomes unstable towards perturbations of the CSH-type when increasing the total protein concentration above the critical level of $c_0 = 357$ in this case. The fastest growing mode indicating the pattern wavelength above onset is $q = 1.36$.

A third important characteristic of the protein clustering model can be identified from the shape of the solutions found in the model. Figure 2 shows a typical stationary solution found in simulations of Eqs. (1). It clearly shows that the deviation of the local protein concentration from its mean value (dashed line) is strongly asymmetric. This indicates a broken up-down symmetry in the system.

III. A MINIMAL PATTERN FORMATION MODEL

As established in the previous chapter, the protein clustering model presented in [18] has three key characteristics: The system undergoes a finite- k instability, the total protein concentration in the system is conserved, and the up-down symmetry is broken. A minimal pattern formation model with the same characteristics is the conserved Swift-Hohenberg (CSH) model [19]:

$$\partial_t u(x, t) = -\partial_x^2 \left[\varepsilon u - (q_0^2 + \partial_x^2)^2 u + \alpha u^2 - u^3 \right]. \quad (9)$$

In this model, $u(x, t)$ is a conserved order parameter field. For $\varepsilon > 0$, the homogeneous state $u = 0$ is unstable towards periodic patterns with the preferred wavenumber q_0 . The dispersion relation of the perturbation growth rate is of the CSH-type as sketched in Fig. 1b. The quadratic nonlinearity breaks the $\pm u$ -symmetry in the system and can be tuned with the asymmetry parameter α . We analyze this model in finite systems assuming no-flux boundary conditions.

Simulations of Eq. (9) show that different solution types are possible depending on the value of the symmetry-breaking parameter α (see Fig. 3). For $\alpha = 1.1$, we find solutions mainly consisting of the mode $\propto \cos(q_0 x)$ with very small contributions from higher harmonics. This solution exists with two polarities: The concentration peak is located in the system center for 1^- and near the boundaries for 1^+ . For $\alpha = 1.1$ both solutions are equally likely to occur starting from random initial conditions. If α is increased to 1.5, the 1^+ -solution vanishes. The 1^- -solution occurs with a probability of around 45%. In addition, a new solution of the approximate form

$$2^\pm = A \cos(q_0 x) \pm B \cos\left(\frac{q_0}{2} x\right) \quad (10)$$

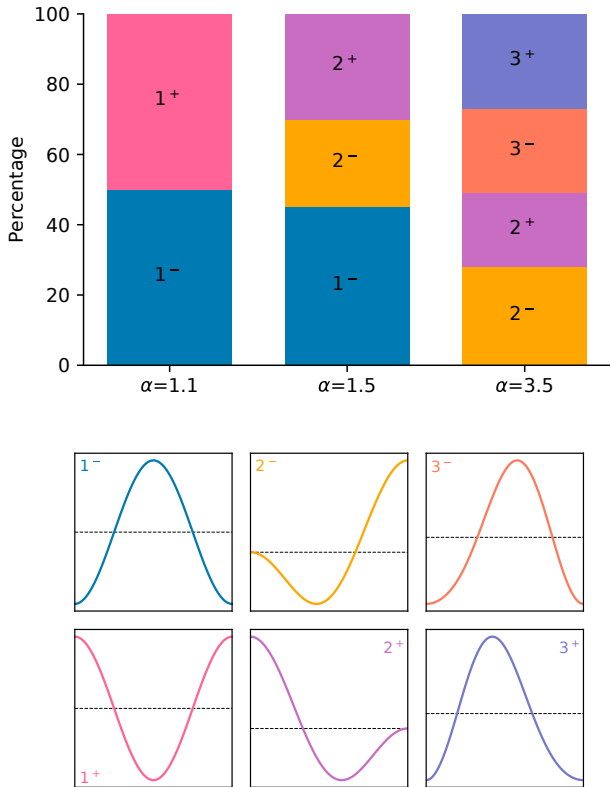


FIG. 3. Stationary solutions in simulations of Eq. (9) for different values of the symmetry-breaking parameter α . Top: Frequency of different solution types in a minimum of 100 simulations for each value of α . Bottom: Sketches of the different solution types. Parameters: $L = \lambda_0$, $q_0 = 1$, $g = 1$, $\varepsilon = 0.5$.

appears. There is no bias towards either of the two polarities of this solution. For $\alpha = 3.5$, the solution 1^- vanishes. The solutions 2^\pm still appear with approximately equal probability. Additionally, there is a third solution type of the form

$$3^\pm = -A \cos(q_0 x) \pm B \cos\left(\frac{q_0}{2} x\right) \mp C \cos\left(\frac{3q_0}{2} x\right). \quad (11)$$

While several modes significantly contribute to this solution type, the shape is very similar to the 1^- -solution. In the 3^\pm -solution, however, the concentration peak is located slightly off-center compared to the central positioning in the 1^- -solution. In this case again, simulations show no clear bias towards the positive or negative polarity.

IV. LINEAR STABILITY & ANALYTICAL CONSIDERATIONS

In this section, we gain more insight into the simulation results presented in Fig. 3 via some semi-analytical

considerations. Due to the no-flux boundary conditions, any possible solution of the system can be written as a series of cosine functions:

$$u(x) = \sum_{n=1}^N u_n \cos(k_n x), \quad (12)$$

where $k_n = n\pi/L$ (with the system length L). The simulation results suggest that for moderate symmetry-breaking parameters α , stationary solutions mainly have a contribution from the basic mode q_0 (if the system length matches the preferred wavelength $\lambda_0 = 2\pi/q_0$). However, due to the broken up-down symmetry in the system, higher harmonics of the intrinsic mode q_0 are actually always excited. An approximation of the stationary solution for finite values of α is thus given by

$$u(x) = A \cos(q_0 x) + B \cos(2q_0 x). \quad (13)$$

We calculate the amplitudes A, B in Eq. (13) by plugging the ansatz into the conserved SH equation, Eq. (9). Projecting onto the cosine modes $\propto \cos(q_0 x)$ and $\propto \cos(2q_0 x)$, we find two coupled equations for the amplitudes A and B :

$$0 = A \left(\varepsilon + \alpha B - \frac{3}{4} g A^2 - \frac{3}{2} g B^2 \right), \quad (14)$$

$$0 = \varepsilon B + \frac{1}{2} \alpha A - \frac{3}{4} g B^3 - \frac{3}{2} g A^2 B - 4q_0^4 B. \quad (15)$$

Assuming the amplitudes to be real, we generally find two relevant solutions: $[A > 0, B > 0]$ and $[-A, B]$. The different signs in the amplitude of the contribution $\propto \cos(q_0 x)$ correspond to solutions with different polarities. We call a solution with a maximum in the center of the system u^- , corresponding to the solution $[-A, B]$, while u^+ is a solution with the maximum at the system boundary corresponding to $[A, B]$ (see Fig. 4, top). Figure 4 (bottom) shows the amplitudes A and B as a function of the symmetry-breaking parameter α . Both A and B increase with increasing α . Thus, the contribution B of the higher harmonic $\propto \cos(2q_0 x)$ is small for small values of the asymmetry parameter α and becomes significant only for strongly broken symmetry. This is in agreement with observations in the simulations.

We next analyze the stability of these solutions by adding a small perturbation v to the stationary solution, $u = u_\pm + v$, plugging the ansatz into Eq. (9) and linearizing with respect to v . The dynamic equation for the perturbation v then reads:

$$\partial_t v = -\partial_x^2 \left[\varepsilon v - (q_0^2 + \partial_x^2) v + 2\alpha u_\pm v - 3g u_\pm^2 v \right]. \quad (16)$$

The term $2\alpha u_\pm v$ already suggests that the stability will be different depending on the polarity of the solution. We solve Eq. (16) via a cosine ansatz for the perturbation v :

$$v = e^{\sigma t} \sum_{n=1}^N v_n \cos(k_n x), \quad (17)$$

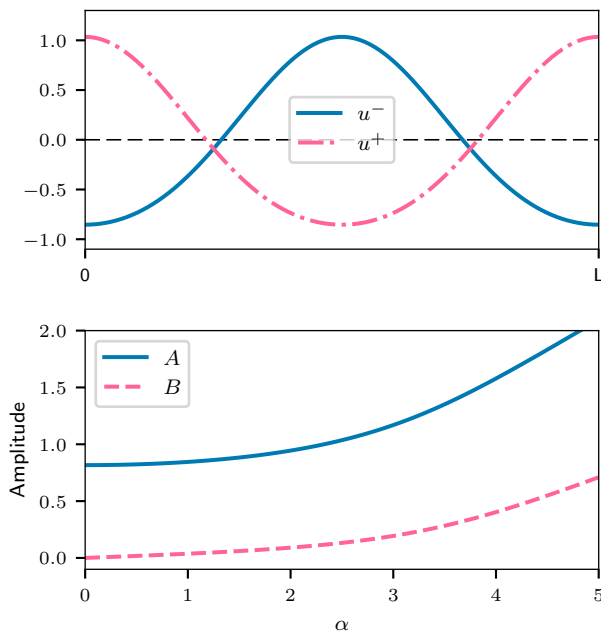


FIG. 4. Top: Solution types of two-mode solutions as given in Eq. (13): u^- with negative polarity (i.e. $[-A, B]$), u^+ with positive polarity (i.e. $[A, B]$). Bottom: Amplitudes of the two-mode solution, Eq. (13), as a function of symmetry-breaking parameter α . Other parameters: $q_0 = 1$, $g = 1$, $\varepsilon = 0.5$.

where σ is the growth rate of the perturbation and $k_n = n\pi/L$. Projecting onto the different cosine modes, we end up with an eigenvalue problem for the growth rate σ that we can solve numerically.

Figure 5 shows the largest eigenvalue for the two solution types with different polarity, u^\pm , as a function of α , the strength of the broken up-down-symmetry. In the top image in Fig. 5 the system size is $L = \lambda_0$. In this case, the growth rate for the solution u^- with the concentration maximum in the system center is always smaller than for the solution u^+ . The solution u^+ first becomes unstable at $\alpha = 1.3$. The solution with negative polarity stays stable up until $\alpha = 3.1$. Thus, in the region $1.3 < \alpha < 3.1$, only the solution with negative polarity is stable. This is the parameter region of polarity bias towards the solution u^- . For $\alpha > 3.1$, finally, both solutions are unstable. These results explain the simulation results presented in Fig. 3: both solutions u^\pm were equally likely for $\alpha = 1.1$, the solution u^+ vanishes when α is increased above the critical value of $\alpha = 1.3$. For even larger α , both solutions vanish in favor of multi-mode solutions.

Interestingly, the situation changes if the system size is doubled to $L = 2\lambda_0$ (Fig. 5, bottom). Changing the system size influences the linear stability due to the discretization of possible perturbation modes. In the ansatz for the perturbation, Eq. (17), the perturbation modes are given by k_n which is connected to the system length

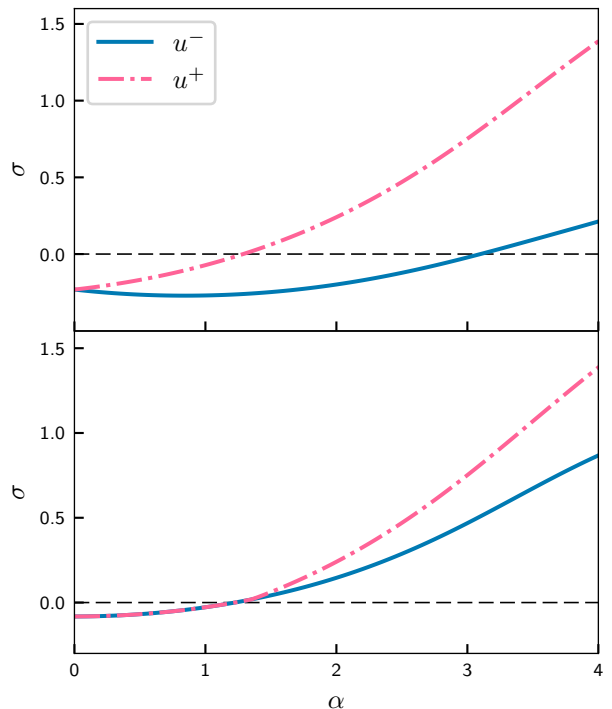


FIG. 5. Largest growth rates for perturbations of the stationary two-mode solutions u^\pm as a function of the up-down symmetry parameter α for two different system lengths: $L = \lambda_0$ (top) and $L = 2\lambda_0$ (bottom). Other parameters: $q_0 = 1$, $g = 1$, $\varepsilon = 0.5$.

via $k_n = n\pi/L$. Thus, in a larger system, the smallest possible perturbation wavenumber as well as the distance between the modes decreases - opening up more possibilities for the solution to become unstable. Here, the solutions with different polarity become simultaneously unstable at $\alpha = 1.3$, and the polarity bias thus vanishes. This is also confirmed in simulations for system lengths $L = 2\lambda_0$, in which no polarity bias can be detected for $\alpha < 1.3$. For larger values of α , both two-mode solutions u^\pm vanish in favor of more complex multi-mode solutions.

V. MINIMUM REQUIREMENTS

The conserved SH model was the first simple model where we found polarity bias. The decision to study the two-mode solution, Eq. (13), was based on simulation results and the knowledge that broken up-down symmetries excite higher harmonics. However, neither conservation nor two-mode solutions are required to find polarity bias. In fact, the results are mostly unchanged if we study the standard unconserved Swift-Hohenberg model [4],

$$\partial_t u = \varepsilon u - (q_0^2 + \partial_x^2)^2 u + \alpha u - u^3, \quad (18)$$

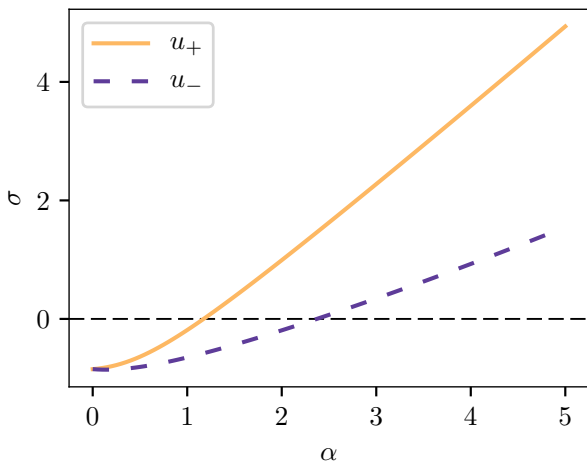


FIG. 6. Largest growth rates for perturbations of the stationary solutions u_{\pm} in the regular SH model of size $L = \lambda_0$ as a function of the up-down symmetry parameter α .

with a simple periodic solution of the form

$$u = A \cos(q_0 x), \quad (19)$$

where the stationary amplitude is given by

$$A = \pm \sqrt{\frac{4}{3}} \varepsilon. \quad (20)$$

In the following, we will call the solution with positive amplitude u^+ , while u^- stands for the solution with $A < 0$.

Fig. 6 shows the largest perturbation growth rates for the two solutions u_{\pm} in a system of size $L = \lambda_0$ as a function of α . The solution u_+ becomes unstable at $\alpha = 1.2$, while the solution u_- only becomes unstable at $\alpha = 2.4$. Thus, in the range $\alpha = [1.2, 2.4]$, only the solution with the negative sign of the amplitude is stable - creating a polarity bias.

As was the case for the CSH model discussed in the previous section, the polarity bias depends on the system size. If we increase the system size to $L = 2\lambda_0$, the polarity bias disappears (see. Fig. 7). The largest growth rate in this case does not depend on the sign of the amplitude. Thus, both solution types become unstable at the same time (at $\alpha = 1.2$) resulting in no clear bias towards any of the two solutions.

From these observations we can conclude the minimum requirements for polarity bias: A broken up-down symmetry in a small finite system leads to polarity bias.

VI. MORE DETAILED OBSERVATIONS

The broken up-down symmetry is obviously required to create solutions of different polarity in the first place.

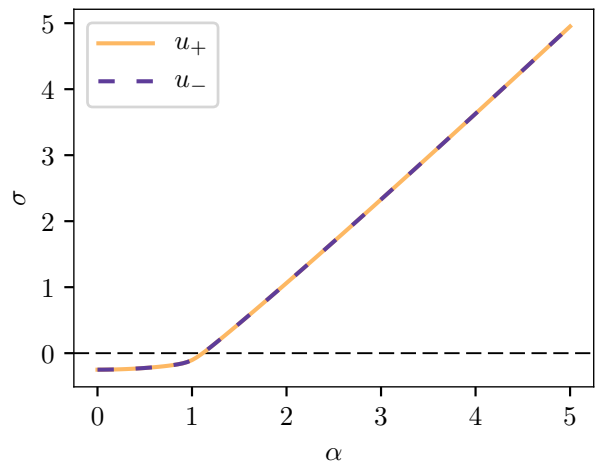


FIG. 7. Largest growth rates for perturbations of the stationary solutions u_{\pm} in the regular SH model of size $L = 2\lambda_0$ as a function of the up-down symmetry parameter α .

However, why do we also need small system sizes? In general, the solution seems to first become unstable towards small perturbation wavenumbers. Note that due to the finite system size and the no-flux boundary conditions, the smallest possible perturbation wavenumber is $k_{\min} = \pi/L$, where L is the system length. In the system of size $L = \lambda_0$, the smallest possible wavenumber is $k_{\min} = q_0/2$. If we assume the perturbation to only have contributions with this wavenumber, the single growth rate for the perturbation is given by

$$\sigma_{\lambda_0} = \varepsilon - \frac{9}{16} q_0^4 - \frac{3}{2} g A^2 \pm \alpha A. \quad (21)$$

Due to the linear contribution $\propto \alpha A$, this growth rate depends on the sign of the amplitude A . Thus, the solution u^+ (where $A > 0$) first becomes unstable at

$$\alpha_c = \frac{(2g-1)\sqrt{3}}{2} \sqrt{\varepsilon} + \frac{9\sqrt{3}}{32} \frac{q_0^4}{\sqrt{\varepsilon}}. \quad (22)$$

For the parameters used in Fig. 6, we get $\alpha_c \approx 1.3$. This is in good agreement with our earlier observations where we used a multimode ansatz, Eq. (17). For this single-mode perturbation and the parameters used in Fig. 6, the solution u^- would, in fact, never become unstable. However, as we saw from the detailed linear stability analysis earlier in this chapter, higher harmonic contributions to the perturbation eventually destabilize the solution u^- for higher values of α . Nevertheless, from this single-mode perturbation approximation, we can already see the origin of the polarity bias.

Increasing the system size to $L = 2\lambda_0$ allows for smaller perturbation wavenumbers, namely $k_{\min} = q_0/4$. A single-mode perturbation with the wavenumber $q_0/4$

would lead to the growth rate

$$\sigma = \varepsilon - \frac{225}{256}q_0^4 - \frac{3}{2}gA^2 = (1 - 2g)\varepsilon - \frac{225}{256}q_0^4. \quad (23)$$

For $g = 1$, this growth rate is always negative and thus the solution would remain stable. However, this changes when we also take the next perturbation mode that couples to the mode $q_0/4$ into account, thus making an ansatz of the form

$$v = \exp^{\sigma t} \left(v_1 \exp^{i\frac{1}{4}q_0 x} + v_2 \exp^{i\frac{3}{4}q_0 x} \right). \quad (24)$$

Of the two eigenvalues, one is usually negative, while the other is given by

$$\sigma_{2\lambda_0} = \varepsilon - \frac{137}{256}q_0^4 - \frac{3}{2}gA^2 + \sqrt{\alpha^2 A^2 + \frac{121}{1024}q_0^8}. \quad (25)$$

Comparing this to σ_{λ_0} , Eq. (21), we find that $\sigma_{2\lambda_0} > \sigma_{\lambda_0}$. By increasing the system size and thus allowing smaller wavenumbers, the instability towards the $q_0/2$ mode becomes irrelevant. Instead the new smallest wavenumber and the higher harmonic modes it couples to are responsible for the instability of the stationary periodic solution. $\sigma_{2\lambda_0}$, however, is independent of the sign of the amplitude. Thus both solutions u^+ and u^- simultaneously become unstable at $\alpha_c \approx 1.2$ which is in agreement with the value we found earlier in the full stability analysis.

VII. CONCLUSIONS & OPEN QUESTIONS

In this work, we tackled the question of protein cluster positioning in cells from a generic pattern formation perspective. In order to do so, we studied minimal pattern formation models which mimic key characteristics

of a recently introduced protein clustering model [18] in small confined systems. We found that polarity bias, i.e. a preference for high density clusters in the center of the system instead of aggregations near the system boundary, is a result of a broken up-down symmetry in combination with strong spatial confinement.

However, this work can only be seen as a first step to further explore this issue. Many questions still remain when it comes to understanding how biological systems control spatial positioning. In our minimal system, polarity bias is limited to the simplest quasi-one-mode solution type. For stronger asymmetry parameters α in the range of where the polarity bias occurs, solutions quickly become more complex with multiple contributing Fourier modes. These solutions do not achieve the desired effect of robust cluster positioning in the cell center. The solution type 2^\pm , for example, would aggregate proteins near one of the system boundaries. Solutions similar to type 3^\pm achieve high densities at a slightly off-center position in the system. If the system size is increased, multi-mode solutions are even more prevalent. In the protein clustering model [18], however, cluster positioning remains robust even for multiple clusters (i.e. if the system length is increased to include multiple wavelengths of the periodic pattern). From these observations we must conclude that confinement and broken symmetry are unlikely to be the only positioning mechanisms used in cells. Some of these possible additional mechanisms such as surface fluxes have already been discussed in [18]. Diving deeper into this subject matter in the future, we hope to gain further insights into additional generic mechanisms of polarity bias.

Fruitful discussions with S. Murray are gratefully acknowledged.

-
- [1] B. Alberts et al. *Molecular biology of the cell (4th ed.)*. Garland Science, New York, 2002.
- [2] E. Schrödinger. *What is life?* Cambridge University Press, Cambridge, 1944.
- [3] R. Solé and B. Goodwin. *Signs of life: How complexity pervades biology*. Basic Books, New York, 2000.
- [4] M. C. Cross and P. C. Hohenberg, *Rev. Mod. Phys.* **65**, 851 (1993).
- [5] A. J. Koch and H. Meinhardt, *Rev. Mod. Phys.* **66**, 1481 (1994).
- [6] S. Kondo and T. Miura, *Science* **329**, 1616 (2010).
- [7] T. Gregor, W. Bialek, R. R. d. R. van Steveninck, D. W. Tank, and E. F. Wieschaus, *PNAS* **102**, 18403 (2005).
- [8] W.-J. Rappel and L. Edelstein-Keshet, *Curr. Opin. Syst. Biol.* **3**, 43 (2017).
- [9] D. A. Kessler and H. Levine, *Phys. Rev. E* **48**, 4801 (1993).
- [10] T. Höfer, J. A. Sherratt, and P. K. Maini, *Physica D* **85**, 425 (1995).
- [11] T. Gregor, K. Fujimoto, N. Masaki, and S. Sawai, *Science* **328**, 1021 (2010).
- [12] S. Kondo, M. Iwashita and M. Yamaguchi, *Int. J. Dev. Biol.* **53**, 851 (2009).
- [13] A. P. Singh and C. Nüsslein-Volhard, *Curr. Biol.* **25**, R81 (2015).
- [14] C. Mou, B. Jackson, P. Schneider, P. A. Overbeek, and D. J. Headon, *PNAS* **103**, 9075 (2006).
- [15] D. M. Raskin and P. A. J. de Boer, *PNAS* **96**, 4971 (1999).
- [16] V. Wells Rowlett and W. Margolin, *Curr. Biol.* **23**, R553 (2013).
- [17] L. Wettmann and K. Kruse, *Phil. Trans. R. Soc. B* **373**, 20170111 (2017).
- [18] S. M. Murray and V. Sourjik, *Nat. Phys.* **13**, 1006 (2017).
- [19] E. Knobloch, *Phys. Rev. A* **40**, 1549 (1989).
- [20] J. W. Cahn and J. E. Hilliard, *J. Chem. Phys.* **28**, 258 (1958).

Active phase separation: A universal approach

Fabian Bergmann, Lisa Rapp and Walter Zimmermann

Phys. Rev. E **98**, 020603(R) (2018)
(DOI: 10.1103/PhysRevE.98.020603)

Reprinted with permission from the American Physical Society
©2018 American Physical Society

Active phase separation: A universal approach

Fabian Bergmann, Lisa Rapp, and Walter Zimmermann*

Theoretische Physik I, Universität Bayreuth, 95440 Bayreuth, Germany

(Received 31 January 2018; revised manuscript received 18 April 2018; published 24 August 2018)

We identify active phase separation as a generic demixing phenomenon in nonequilibrium systems with conservation constraints. Examples range from cell polarization to cell populations communicating via chemotaxis, and from self-propelled particle communities to mussels in ecology. We show that system-spanning properties of active phase separation in nonequilibrium systems near onset are described by the classical Cahn-Hilliard (CH) model. This result is rather surprising since the CH equation is famous as a model for phase separation at thermal equilibrium. We introduce a general reduction scheme to establish a unique mathematical link between the generic CH equation and system-specific models for active phase separation. This approach is exemplarily applied to a model for polarization of cells and a model for chemotactic cell communities. For cell polarization, we also estimate the validity range of the CH model.

DOI: [10.1103/PhysRevE.98.020603](https://doi.org/10.1103/PhysRevE.98.020603)

Demixing phenomena in active, nonequilibrium systems currently attract great attention. Examples include cell polarization [1–12], chemotactically communicating cells [13–17], self-propelled particles [18–21], active matter models [22], mixtures of particles with different mobilities [23–26], models of ion-channel densities [27], or mussels in ecology [28]. All of these examples have three properties in common: First, they resemble classic equilibrium phase separation. Second, in contrast to classic phase separation, these are nonequilibrium transitions. Third, they are all subject to conservation constraints. Since these demixing phenomena take place in nonequilibrium systems, we call them *active phase separation*. Their (local) driving mechanisms are as different as the systems themselves. But do these systems nevertheless share fundamental properties described by a generic model? Here we provide a universal framework for the cross-system characteristics of a class of active phase separation phenomena.

A conceptual parallel to this idea are self-organized patterns in nature. Stripe, hexagonal, or traveling wave patterns are driven by mechanisms that are also as diverse as the systems in which they form [29–34]. Nevertheless, periodic patterns in these different nonequilibrium systems share well-known generic properties [33,34]. They are covered by unconserved order-parameter fields that describe the slowly varying amplitude(s) [envelope(s)]. Even though stripe patterns occur in very different systems, the envelope obeys the same fundamental (nonlinear) Ginzburg-Landau equation [33,34]. It can be derived from basic equations and provides the key to understanding the generic properties of stripe patterns [30,34–36].

In this work, we formulate a similar approach for active phase separation in nonequilibrium systems. We present a reduction scheme generalized to conserved order parameters. At leading order, we thereby obtain the Cahn-Hilliard model [37,38] as the generic model for active phase separation

in nonequilibrium systems. So far, it has typically been used to model liquid-liquid demixing in thermal equilibrium [37,38]. However, we show here that it also describes the system-spanning properties of phase separation in nonequilibrium. Thus, we manage to capture the essence of active phase separation in very different systems in one universal equation. At the same time we expose the underlying similarities between phase separation in and out of equilibrium. The reduction scheme we present here provides a direct mathematical link between the Cahn-Hilliard (CH) model and system-specific models. It also provides the criteria to identify candidates for this class of active phase separation. Our approach is explicitly demonstrated for two representative examples from living matter: a continuum model for cell polarization and a model for chemotactic cell communities.

Cell polarization is central to processes as diverse as cell motility, differentiation, and cell division [1–10]. The polarized cell has two distinct regions similar to the two phases of a separated liquid-liquid mixture. However, cell polarization in living systems is a nonequilibrium phenomenon driven by *dissipative* processes. The molecules that trigger cell polarization are conserved on the timescales of the self-organization. Models for cell polarization usually involve the nonlinear dynamics of several coupled concentration fields for regulating molecules (see, e.g., [4]). However, minimal models with only two concentration fields for the membrane-cytosol exchange already cover essential properties [5–10]. One concentration field $\tilde{u}(\mathbf{r}, t)$ thereby represents molecules bound to the membrane. The other concentration field $\tilde{v}(\mathbf{r}, t)$ describes molecules in the cytosol. Here, we use

$$\tilde{f}(\tilde{u}, \tilde{v}) = -b\tilde{v} + (\tilde{u} + \tilde{v})^2 - (\tilde{u} + \tilde{v})^3 \quad (1)$$

for the membrane to cytosol exchange in the one-dimensional equations for the fields \tilde{u} and \tilde{v} :

$$\partial_t \tilde{u} = D_u \partial_x^2 \tilde{u} + \tilde{f}(\tilde{u}, \tilde{v}), \quad (2a)$$

$$\partial_t \tilde{v} = D_v \partial_x^2 \tilde{v} - \tilde{f}(\tilde{u}, \tilde{v}) \quad (\text{model } P). \quad (2b)$$

*Corresponding author: walter.zimmermann@uni-bayreuth.de

Both fields are coupled via the conservation condition

$$M = \frac{1}{L} \int_0^L [\tilde{u}(x) + \tilde{v}(x)] dx. \quad (3)$$

Another variant of a nonequilibrium phase separation process is clustering of chemotactically communicating cells. They play, for instance, a central role on the route to multicellular fruiting bodies [39]. Here the number of cells is conserved on the timescale of the clustering, but the chemical density field for the cell-cell communication is not [13–17]. We describe a system of chemotactically communicating cells by an extended Keller-Segel model [13–16] with cell density $\tilde{\rho}(\mathbf{r}, t)$ and signal molecule density $\tilde{c}(\mathbf{r}, t)$:

$$\partial_t \tilde{\rho} = \partial_x^2 \tilde{\rho} - s \partial_x \left(\frac{\tilde{\rho}}{1 + \beta \tilde{\rho}} \partial_x \tilde{c} \right), \quad (4a)$$

$$\partial_t \tilde{c} = D_c \partial_x^2 \tilde{c} + \tilde{\rho} - \tilde{c} \quad (\text{model } C). \quad (4b)$$

Model *P* in Eqs. (1) and model *C* in Eqs. (4) have spatially homogeneous solutions u_h, v_h or ρ_h, c_h , respectively. These become unstable beyond critical values of the respective control parameters D_v and s . Immediately above these thresholds, a generic equation can in both cases describe the resulting active phase separation. In the following steps we develop this equation for the conserved order-parameter field.

For both models, we separate the inhomogeneous parts from the basic state, writing $\tilde{u} = u_h + u(x, t)$, etc. We first consider the instability of the homogeneous states with respect to small perturbations. The linear equations in u, v are then solved by the ansatz $u, v = \tilde{u}, \tilde{v} \exp(\sigma t + i q x)$ (or for ρ and c , respectively). We consider the case when one of two eigenvalues $\sigma_{1,2}$ is always negative close to the onset of phase separation. The other eigenvalue, expanded with respect to powers of q^2 , is of the form

$$\sigma = G_2 q^2 - G_4 q^4 + O(q^6) \quad (5)$$

with $G_4 > 0$. The leading order coefficients $G_2^{(P)}$ or $G_2^{(C)}$ include the control parameters D_v and s for models *P* and *C*, respectively. The homogeneous solutions become linearly unstable for $G_2 > 0$. $G_2 = 0$ thus defines the critical values of the control parameters:

$$D_v^c = D_u f_v / f_u, \quad s_c = (\rho_0 h)^{-1}, \quad (6)$$

where $f_{u,v} = \partial_{u,v} f$ and $h = (1 + \beta \rho_0)^{-1}$. As a measure for the distance from the onset of phase separation, we choose the dimensionless control parameter ε , where

$$D_v = D_v^c (1 + \varepsilon), \quad s = s_c (1 + \varepsilon). \quad (7)$$

Next, we consider the basic equations [cf. Eqs. (2) and (4)] in the range of small ε , i.e., $G_2 \propto \varepsilon$. With $G_4 = O(1)$ the growth rate σ becomes positive in a range of small $q^2 \propto \varepsilon$ and is of the order $\sigma \propto \varepsilon^2$. Therefore, we introduce the “slow” spatial scale $X = \sqrt{\varepsilon} x$ and the timescale $T = \varepsilon^2 t$, which is slower than for periodic patterns [34]. The nonlinear analysis demands the introduction of an additional slow timescale, $T_3 = \varepsilon^{3/2} t$ [40]. This leads to the operator replacements

$$\partial_x \rightarrow \sqrt{\varepsilon} \partial_X, \quad \partial_t \rightarrow \varepsilon^{3/2} \partial_{T_3} + \varepsilon^2 \partial_T. \quad (8)$$

In compact matrix form, Eqs. (2) and (4) are

$$\partial_t \mathbf{w} = \mathcal{L} \mathbf{w} + \mathbf{N}, \quad (9)$$

with the respective vectors $\mathbf{w} = (u, v)$ and $\mathbf{w} = (\rho, c)$. The right-hand side includes a linear part $\mathcal{L} \mathbf{w}$ and the nonlinear part \mathbf{N} . For both models we expand \mathbf{w} in orders of $\varepsilon^{1/2}$:

$$\mathbf{w} = \varepsilon^{1/2} \mathbf{w}_1 + \varepsilon \mathbf{w}_2 + \varepsilon^{3/2} \mathbf{w}_3 + O(\varepsilon^2), \quad (10)$$

leading to

$$\mathcal{L} = \mathcal{L}_0 + (\varepsilon \mathcal{L}_1 + \varepsilon^2 \mathcal{L}_2) \partial_X^2 + O(\varepsilon^3), \quad (11)$$

$$\mathbf{N} = \varepsilon \mathbf{N}_2 + \varepsilon^{3/2} \mathbf{N}_3 + \varepsilon^2 \mathbf{N}_4 + \varepsilon^{5/2} \mathbf{N}_5 + O(\varepsilon^3). \quad (12)$$

Inserting the new scalings and expansions into Eq. (9) requires a sorting of the basic equations up to two orders higher in $\varepsilon^{1/2}$ than for common spatial patterns [34]:

$$\varepsilon^{1/2} : \mathcal{L}_0 \mathbf{w}_1 = 0, \quad (13a)$$

$$\varepsilon : \mathcal{L}_0 \mathbf{w}_2 = -\mathbf{N}_2, \quad (13b)$$

$$\varepsilon^{3/2} : \mathcal{L}_0 \mathbf{w}_3 = -\mathcal{L}_1 \partial_X^2 \mathbf{w}_1 - \mathbf{N}_3, \quad (13c)$$

$$\varepsilon^2 : \mathcal{L}_0 \mathbf{w}_4 = \partial_{T_3} \mathbf{w}_1 - \mathcal{L}_1 \partial_X^2 \mathbf{w}_2 - \mathbf{N}_4, \quad (13d)$$

$$\varepsilon^{5/2} : \mathcal{L}_0 \mathbf{w}_5 = \partial_{T_3} \mathbf{w}_2 + \partial_T \mathbf{w}_1 - \mathcal{L}_1 \partial_X^2 \mathbf{w}_3 - \mathcal{L}_2 \partial_X^2 \mathbf{w}_1 - \mathbf{N}_5. \quad (13e)$$

For model *P*, we find at order $\varepsilon^{1/2}$ [41]

$$\mathbf{w}_1 = \tilde{A}(X, T) \begin{pmatrix} f_v \\ -f_u \end{pmatrix}. \quad (14)$$

Note that in contrast to the Ginzburg-Landau equation for stripes, $\tilde{A}(X, T)$ in our case is not the envelope of an underlying small-scale structure. An iterative solution of the hierarchy, Eqs. (13), leads to a dynamical equation for \tilde{A} via Fredholm alternatives at orders ε^2 and $\varepsilon^{5/2}$ [34]. After returning to the original coordinates x and t , and rescaling the amplitude $A = \sqrt{\varepsilon} \tilde{A}$, it takes the following form:

$$\partial_t A = -\partial_x^2 [\alpha_1 \varepsilon A + \alpha_2 \partial_x^2 A - \alpha_3 A^2 - \alpha_4 A^3]. \quad (15)$$

This is the Cahn-Hilliard model in one dimension [37] with a quadratic nonlinearity $\propto A^2$ (where $\alpha_1, \alpha_2, \alpha_4 > 0$). It corresponds to nonsymmetric mixtures of two liquids at thermal equilibrium. Equation (15) covers the approximate dispersion relation of the full model in Eq. (5) and nonlinearities up to third order in A . The derivation of the CH equation via the introduced reduction scheme automatically provides a mathematical link to the model for cell polarization in Eqs. (2). That is, the coefficients α_i are expressed by the parameters of the full model:

$$\alpha_1 = D_u f_v / b, \quad \alpha_2 = D_u^2 f_v / (b f_u), \quad (16a)$$

$$\alpha_3 = D_u b (3M - 1) / f_u, \quad \alpha_4 = D_u b^2 / f_u, \quad (16b)$$

with $f_u = -3M^2 + 2M - b$ and $f_v = -3M^2 + 2M$.

By application of the reduction scheme, the chemotaxis model *C* reduces to a similar equation for the density variation

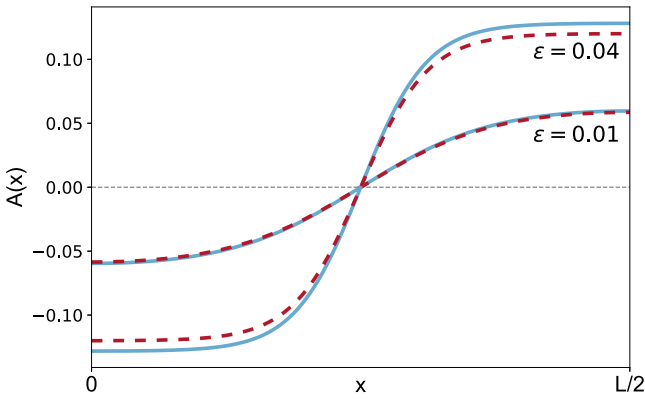


FIG. 1. Steady-state profiles $A(x)$ in the symmetric case ($M = 1/3$): Comparison of model P , Eqs. (2) (solid lines), to the corresponding solutions of the reduced CH model, Eq. (15) (dashed lines), for two values of the control parameter $\varepsilon = 0.01, 0.04$.

ρ , but with different coefficients [41]:

$$\partial_t \rho = -\partial_x^2 [\varepsilon \rho + D_c \partial_x^2 \rho + \frac{1}{2} s_c h^2 \rho^2 - \frac{1}{3} s_c \beta h^3 \rho^3]. \quad (17)$$

Note that the chemical signal c follows the cell density adiabatically.

The reduced models, Eqs. (15) and (17), capture the dynamics of the respective slow mode of phase separation [34]. Both CH models follow potential dynamics [38] even though the full Eqs. (2) and (4) do not. These qualities are a direct parallel to stripe patterns and their representation via the universal Ginzburg-Landau equation [30,34–36]. Thus, similar to the amplitude equation for stripes, we expect the CH model to play a generic role for active phase separation. Note that the reduced CH models, Eqs. (15) and (17), describe the behavior of a *conserved order parameter*—a reflection of the conservation constraints placed upon the original models P and C . The reduced models certainly cover the behavior of the full system near the (supercritical or weakly subcritical) bifurcation point. But in which parameter range further from the onset of phase separation does this agreement prevail? We will explore this by comparison of stationary solutions for the cell polarization model [cf. Eqs. (2)] and its approximation by the CH model in Eq. (15). We first study the special case $M = 1/3$, i.e., $\alpha_3 = 0$ and \pm symmetry of Eq. (15). This corresponds to the classic CH model [37]. For this case we compare in Fig. 1 steady-state solutions of the full model P to those of the related CH model for two different control parameter values ε (see Supplemental Material [41] for details on simulation methods). Due to the \pm symmetry in Eq. (15), the maximum and minimum of these profiles have the same absolute value. According to the conservation condition, the two phases with increased or decreased concentration each occupy half the system. With respect to both properties, the CH model covers the behavior of the full model. With increasing ε , the plateau values of the steady-state profiles increase and the coherence length decreases. Consequently, the profiles in Fig. 1 evolve toward a more steplike form. Note that in Figs. 1–5, the amplitude for the full model is calculated from the field v . The amplitude for u resembles the amplitude A from Eq. (15) even more closely.

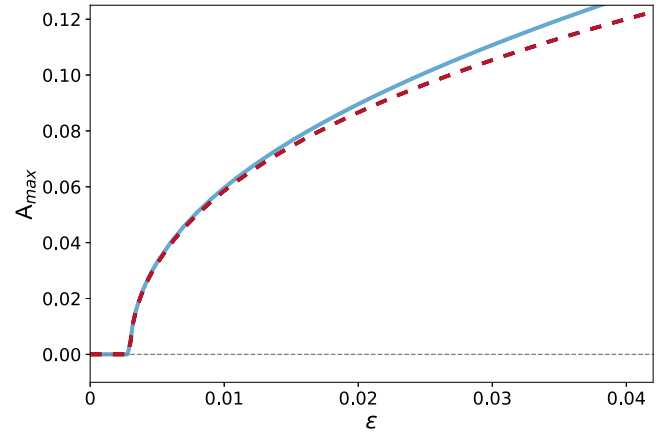


FIG. 2. Plateau values of the steady-state solutions in the symmetric case ($M = 1/3$): Comparison of model P , Eqs. (2) (solid line), to the corresponding values of the reduced CH model, Eq. (15) (dashed line), as a function of the control parameter ε .

Figure 2 shows the plateau values of the steady-state solutions as a function of ε . It thereby illustrates the validity range of the CH model—including the perfect agreement at onset, and the expected increasing deviations with increasing ε . Figure 2 also illustrates that the transition to active phase separation in the symmetric case occurs in a supercritical bifurcation. Note that the finite system size shifts the onset of phase separation to a positive value $\varepsilon_c = \alpha_2 \pi^2 / (L^2 \alpha_1)$ ($= 0.00296$ for the chosen parameters).

For $M \neq 1/3$, the quadratic term in Eq. (15) is finite. This leads to asymmetric phase separation, where the concentration deviates asymmetrically from its mean value. An example of this scenario is shown in Fig. 3 for $M = 0.3$. This corresponds to a small asymmetry parameter $\alpha_3 / \sqrt{\alpha_4} \simeq 0.055$. In this case, Eq. (15) captures the behavior of the full model very well. A comparison between the CH equation and the full model as a function of ε is presented in Fig. 4. In the presence of A^2 , the bifurcation from the homogeneous state

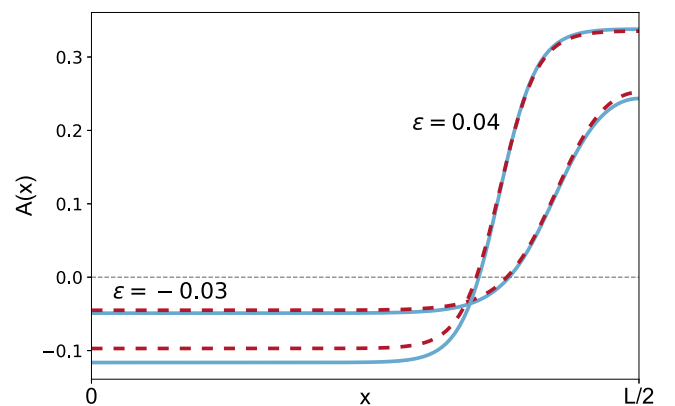


FIG. 3. Similar as in Fig. 1, but in the asymmetric case ($M = 0.3$), i.e., with the A^2 contribution in Eq. (15). Steady-state profiles of model P , Eqs. (2) (solid lines), compared to the corresponding solutions of the reduced CH model, Eq. (15) (dashed lines), for two values of the control parameter $\varepsilon = -0.03, 0.04$.

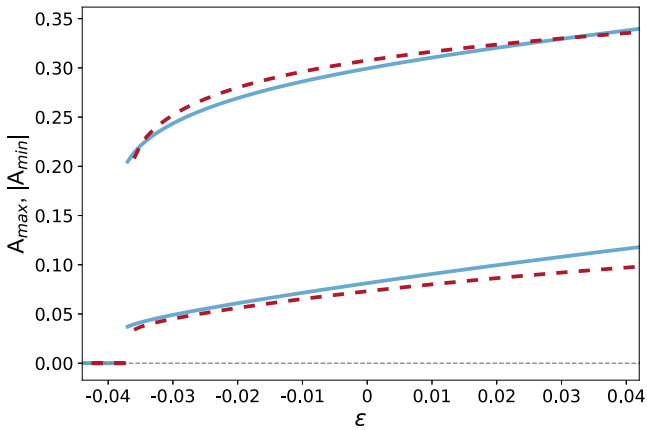


FIG. 4. Similar as in Fig. 2, but in the asymmetric case ($M = 0.3$). Upper and modulus of the lower plateau values of model P , Eqs. (2) (solid lines), compared to the corresponding values of the reduced CH model, Eq. (15) (dashed lines), as a function of the control parameter ε .

to phase separation is subcritical. That is, we find a jump from $A = 0$ to finite plateau values. Moreover, we observe the phase-separated state already for subcritical control parameter values. If the asymmetry parameter $\alpha_3/\sqrt{\alpha_4}$ is of $O(\sqrt{\varepsilon})$, both nonlinear terms in Eq. (15) are of the same order. As Fig. 5 shows, the reduced CH model is a good representation of the full model up to these moderate asymmetries. For stronger asymmetries, however, the full model may deviate strongly from its approximation [41]. That is, the full model may exhibit either for strong asymmetries or for large values of ε its own nongeneric “dialect” of active phase separation.

In this work, we identify a generic, system-spanning behavior for a number of very different demixing phenomena in active and living systems—a class of active phase separation. We have shown that this nonequilibrium transition is at leading order described by the CH equation [37,38]—the same equation that usually describes phase separation at thermal equilibrium. All models in this class have three central

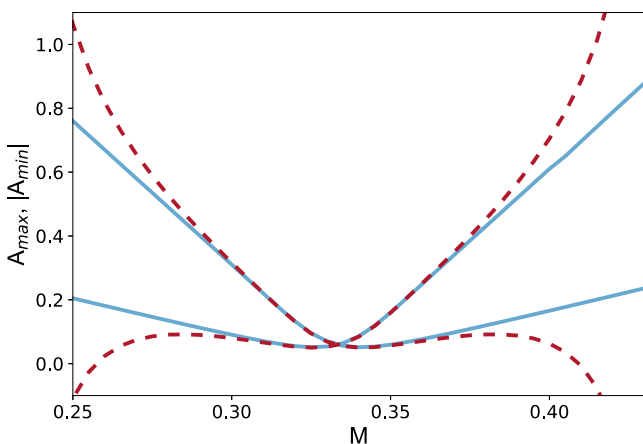


FIG. 5. Upper and modulus of the lower plateau values of the full (dashed lines) vs reduced model (solid lines) as a function of the asymmetry parameter M at a fixed control parameter value $\varepsilon = 0.01$.

properties in common: First, the slow mode growing out of a homogeneous basic state is conserved. Second, the slow mode follows the dispersion relation in Eq. (5). Third, nonlinearities up to third order in the order-parameter fields are sufficient near onset of active phase separation. These conditions ensure the correct signs of the coefficients α_i in the CH equation, Eq. (15). Furthermore, we introduced a perturbative reduction scheme that allows a direct derivation of the CH equation from system-specific nonequilibrium models. With this mathematical link, we can also determine the system-specific values of the coefficients in the CH model. This even allows for a quantitative comparison between the CH model and the original model equations. Note that the derived CH model follows potential dynamics [38], even though the system-specific equations—as the starting point of the reduction—are nonpotential systems.

We verified our generic approach by applying it explicitly to two active matter systems: a minimal model of cell polarization and a model for clustering in chemotactic cell communities. We found a convincing validity range of the generic CH equation as a representation of a cell polarization model near onset. Beyond the system-specific validity range of the CH model further interesting individual “dialects” of active phase separation may come into play. These include, for instance, the effects of higher-order nonlinearities covered by the full system-specific models. The so-called “active model B ,” for example, was recently introduced for modeling the nonequilibrium phenomenon “motility-induced phase separation” (MIPS) by a single mean field [42,43]. It includes the higher-order nonlinearity $\Delta[\nabla A(\mathbf{r})]^2 \propto \varepsilon^3$. This additional contribution renders the active model B nonintegrable [42] (see Supplemental Material [41] for a more detailed discussion of integrability with higher-order nonlinearities). However, this higher-order contribution becomes negligible near the onset of active phase separation, i.e., the validity range of the generic CH model. For some systems, fluctuations may also become relevant—especially for the coarsening dynamics in low spatial dimensions. This is similar to coarsening in equilibrium phase separation [38].

Our work also suggests the universality of phase separation processes—whether in or out of equilibrium. Their shared characteristics at leading order are reflected in the joint representation by the CH model. Our insights justify the recent usage of the CH equation as a phenomenological model for the clustering phenomenon observed for mussels [28] and further nonequilibrium demixing phenomena.

We expect our generic reduction to the CH model to work for further systems showing active phase separation. These include active colloids [18,21,43], active matter systems [22], or ion channels [27]. We anticipate these systems to also show the fingerprints of the class of active phase separation we introduced here for systems with a conserved order parameter. In this sense, our results are a conceptual parallel to the Ginzburg-Landau equation for an unconserved order parameter [30,34–36], which captures the essence of nonequilibrium stripe patterns near onset and also follows potential dynamics.

Our generic approach is a starting point for further investigations of nonequilibrium phenomena in systems with conserved quantities. Possible generalizations are order-parameter

models that also cover systems with more general dispersion relations than in Eq. (5) (see, e.g., Refs. [44,45]) or oscillatory phase separation phenomena.

Support by the Elite Study Program Biological Physics and inspiring exchanges with W. Pesch, I. Rehberg, and M. Weiss are gratefully acknowledged.

-
- [1] D. S. Johnston and J. Ahringer, *Cell* **141**, 757 (2010).
- [2] B. J. Thompson, *Development* **140**, 13 (2013).
- [3] N. W. Goehring and S. W. Grill, *Trends Cell Biol.* **23**, 72 (2013).
- [4] A. Jilkine, A. F. M. Marée, and L. Edelstein-Keshet, *Bull. Math. Biol.* **69**, 1943 (2007).
- [5] M. Otsuji, S. Ishihara, C. Co, K. Kaibuchi, A. Mochizuki, and S. Kuroda, *PLoS Comput. Biol.* **3**, e108 (2007).
- [6] Y. Mori, A. Jilkine, and L. Edelstein-Keshet, *Biophys. J.* **94**, 3684 (2008).
- [7] A. B. Goryachev and A. V. Pokhilko, *FEBS Lett.* **582**, 1437 (2008).
- [8] A. Jilkine and L. Edelstein-Keshet, *PLoS Comput. Biol.* **7**, e1001121 (2011).
- [9] B. Rubinstein, B. D. Slaughter, and R. Li, *Phys. Biol.* **9**, 045006 (2012).
- [10] P. K. Trong, E. M. Nicola, N. W. Goehring, K. V. Kumar, and S. W. Grill, *New J. Phys.* **16**, 065009 (2014).
- [11] S. Alonso and M. Bär, *Phys. Biol.* **7**, 046012 (2010).
- [12] N. W. Goehring, P. K. Trong, J. S. Bois, D. Chowdhury, E. M. Nicola, A. A. Hyman, and S. W. Grill, *Science* **334**, 1137 (2011).
- [13] E. F. Keller and L. A. Segel, *J. Theor. Biol.* **26**, 399 (1970).
- [14] E. F. Keller and L. A. Segel, *J. Theor. Biol.* **30**, 225 (1971).
- [15] M. J. Tindall, P. K. Maini, S. L. Porter, and J. P. Armitage, *Bull. Math. Biol.* **70**, 1570 (2008).
- [16] T. Hillen and K. J. Painter, *J. Math. Biol.* **58**, 183 (2009).
- [17] M. Meyer, L. Schimansky-Geier, and P. Romanczuk, *Phys. Rev. E* **89**, 022711 (2014).
- [18] J. Palacci, S. Sacanna, A. P. Steinberg, D. J. Pine, and P. M. Chaikin, *Science* **339**, 936 (2013).
- [19] I. Buttinoni, J. Bialké, F. Kümmel, H. Löwen, C. Bechinger, and T. Speck, *Phys. Rev. Lett.* **110**, 238301 (2013).
- [20] J. Stenhammar, A. Tiribocchi, R. J. Allen, D. Marenduzzo, and M. E. Cates, *Phys. Rev. Lett.* **111**, 145702 (2013).
- [21] T. Speck, J. Bialké, A. M. Menzel, and H. Löwen, *Phys. Rev. Lett.* **112**, 218304 (2014).
- [22] J. S. Bois, F. Jülicher, and S. W. Grill, *Phys. Rev. Lett.* **106**, 028103 (2011).
- [23] A. Y. Grosberg and J. F. Joanny, *Phys. Rev. E* **92**, 032118 (2015).
- [24] J. Stenhammar, R. Wittkowski, D. Marenduzzo, and M. E. Cates, *Phys. Rev. Lett.* **114**, 018301 (2015).
- [25] S. N. Weber, C. A. Weber, and E. Frey, *Phys. Rev. Lett.* **116**, 058301 (2016).
- [26] J. Smrek and K. Kremer, *Phys. Rev. Lett.* **118**, 098002 (2017).
- [27] P. Fromherz and B. Kaiser, *Europhys. Lett.* **15**, 313 (1991).
- [28] Q.-X. Liu, A. Doelman, V. Rottschäfer, M. de Jager, P. M. J. Herman, M. Rietkerk, and J. van de Koppel, *Proc. Natl. Acad. Sci. USA* **110**, 11905 (2013).
- [29] P. Ball, *The Self-Made Tapestry: Pattern Formation in Nature* (Oxford University Press, Oxford, 1998).
- [30] M. C. Cross and H. Greenside, *Pattern Formation and Dynamics in Nonequilibrium Systems* (Cambridge University Press, Cambridge, 2009).
- [31] S. Kondo and T. Miura, *Science* **329**, 1616 (2010).
- [32] E. Meron, *Nonlinear Physics of Ecosystems* (CRC Press, Boca Raton, FL, 2015).
- [33] I. Aranson and L. Kramer, *Rev. Mod. Phys.* **74**, 99 (2002).
- [34] M. C. Cross and P. C. Hohenberg, *Rev. Mod. Phys.* **65**, 851 (1993).
- [35] A. C. Newell and J. A. Whitehead, *J. Fluid Mech.* **38**, 279 (1969).
- [36] L. A. Segel, *J. Fluid Mech.* **38**, 203 (1969).
- [37] J. W. Cahn and J. E. Hilliard, *J. Chem. Phys.* **28**, 258 (1958).
- [38] A. J. Bray, *Adv. Phys.* **43**, 357 (1994).
- [39] L. Wolpert, *Principles of Development* (Oxford University Press, Oxford, 2002).
- [40] The introduction of two timescales is a mathematical necessity to solve the following hierarchy of Eqs. (13). There the solvability condition in the order ε^2 demands the introduction of an additional timescale T_3 . In the final Eqs. (15) and (17), this timescale leads to the additional quadratic term compared to the classical Cahn-Hilliard model.
- [41] See Supplemental Material at <http://link.aps.org/supplemental/10.1103/PhysRevE.98.020603> for more detailed calculations, simulation methods, and discussions about strong asymmetries and higher-order nonlinearities.
- [42] R. Wittkowski, A. Tiribocchi, J. Stenhammar, R. J. Allen, D. Marenduzzo, and M. E. Cates, *Nat. Commun.* **5**, 4351 (2013).
- [43] M. E. Cates and J. Tailleur, *Annu. Rev. Condens. Matter Phys.* **6**, 219 (2015).
- [44] S. M. Murray and V. Sourjik, *Nat. Phys.* **13**, 1006 (2017).
- [45] F. Meng, D. Matsunaga, and R. Golestanian, *Phys. Rev. Lett.* **120**, 188101 (2018).

Active Phase Separation - A Universal Approach

Supporting Information (SI)

Fabian Bergmann, Lisa Rapp, and Walter Zimmermann
Theoretische Physik I, Universität Bayreuth, 95440 Bayreuth, Germany

I. CH-MODEL FOR MINIMAL CELL POLARIZATION MODEL

A minimal model for a conserved reaction diffusion systems for with concentration fields, \tilde{u} and \tilde{v} is described in the main text. The two coupled equations are

$$\partial_t \tilde{u} = D_u \nabla^2 \tilde{u} + f(\tilde{u}, \tilde{v}), \quad (1a)$$

$$\partial_t \tilde{v} = D_v \nabla^2 \tilde{v} - f(\tilde{u}, \tilde{v}) \quad (1b)$$

with the reaction scheme

$$f(\tilde{u}, \tilde{v}) = -b\tilde{u} + (\tilde{u} + \tilde{v})^2 - (\tilde{u} + \tilde{v})^3. \quad (2)$$

The homogeneous basic states (u_h, v_h) are determined by

$$f(u_h, v_h) = 0.$$

and the conservation condition

$$M = \frac{1}{L} \int_0^L [u_h + v_h] dx = u_h + v_h.$$

Accordingly, the basic states are

$$u_h = \frac{M^2(1-M)}{b}, \quad (3a)$$

$$v_h = \frac{M(M^2 - M + b)}{b}. \quad (3b)$$

A linear stability analysis of the homogenous basic state leads to the the growth rate σ for a small perturbation:

$$\sigma_{\pm} = \frac{1}{2} \left[\gamma_1 \pm \sqrt{\gamma_1^2 - 2q^2\gamma_2 + q^4\gamma_3^2} \right], \quad (4)$$

where

$$\begin{aligned} \gamma_1 &= -(D_u + D_v)q^2 + f_u - f_v, \\ \gamma_2 &= -(f_u + f_v)(D_u - D_v), \\ \gamma_3 &= D_u - D_v, \end{aligned} \quad (5)$$

with

$$f_u = \left. \frac{\partial f}{\partial \tilde{u}} \right|_{\tilde{u}=u_h, \tilde{v}=v_h} = -3M^2 + 2M - b, \quad (6a)$$

$$f_v = \left. \frac{\partial f}{\partial \tilde{v}} \right|_{\tilde{u}=u_h, \tilde{v}=v_h} = -3M^2 + 2M. \quad (6b)$$

Expanding the maximum growth rate for small values of q in the case $f_v > f_u$, we find

$$\sigma_+ = G_2 q^2 - G_4 q^4 + \mathcal{O}(q^6) \quad (7)$$

with

$$\begin{aligned} G_2 &= \frac{D_v f_u - D_u f_v}{f_v - f_u}, \\ G_4 &= \frac{2(D_u - D_v)^2 f_u f_v}{(f_v - f_u)^2}. \end{aligned}$$

Note, for $f(\tilde{u}, \tilde{v})$ given by Eq. (2) we have $f_v - f_u = b$. This means for positive b , the inequality $f_v > f_u$ is fulfilled. Physical constraints, like $u_h, v_h > 0$ for the concentrations, lead to restrictions on the parameters. In our work, we choose $b = 0.3$, which restricts M to the interval $0.228 \lesssim M \lesssim 0.438$.

As in the main text Eqs. (1) can be written in a compact form as follows

$$\partial_t \mathbf{w} = \mathcal{L} \mathbf{w} + \mathbf{N}, \quad (8)$$

with $\mathbf{w} = (u, v)$, the linear part

$$\mathcal{L} = \begin{pmatrix} D_u \partial_x^2 + f_u & f_v \\ -f_u & D_v \partial_x^2 - f_v \end{pmatrix},$$

and the nonlinear part

$$\mathbf{N} = [(1 - 3M)(u + v)^2 - (u + v)^3] \begin{pmatrix} 1 \\ -1 \end{pmatrix}.$$

Applying the scalings and expansions of the perturbative reduction scheme as described in the main text, leads as in Eqs. (13) of main text to a hierarchy of equations. At the order $\sqrt{\varepsilon}$ of this hierarchy we find as solution

$$\mathbf{w}_1 = \tilde{A}(X, T_3, T) \begin{pmatrix} f_v \\ -f_u \end{pmatrix}. \quad (9)$$

At the order ε we find an equation for \mathbf{w}_2 :

$$f_u u_2 + f_v v_2 = -b(1 - 3M)\tilde{A}^2.$$

Since we have only one equation to determine u_2 and v_2 , we have an additional degree of freedom. We choose this in a way that the solution at order ε is

$$\mathbf{w}_2 = \tilde{A}^2 b(1 - 3M) \begin{pmatrix} 1 \\ -1 \end{pmatrix} + \tilde{B}(X, T_3, T) \begin{pmatrix} f_v \\ -f_u \end{pmatrix}, \quad (10)$$

with $\tilde{B}(X, T_3, T)$ reflecting the additional degree of freedom. In a similar way we solve the equation in order $\varepsilon^{3/2}$ with

$$\begin{aligned} \mathbf{w}_3 &= \left[D_u \frac{f_v}{b} \partial_X^2 \tilde{A} - b^2 \tilde{A}^3 + b(2 - 6M)\tilde{A}\tilde{B} \right] \begin{pmatrix} 1 \\ -1 \end{pmatrix} \\ &+ \tilde{C}(X, T_3, T) \begin{pmatrix} f_v \\ -f_u \end{pmatrix}. \end{aligned} \quad (11)$$

Finally, in the orders ε^2 and $\varepsilon^{5/2}$ the Fredholm alternative leads to two amplitude equations:

$$\partial_{T_3} \tilde{A} = -D_u \frac{b}{f_u} (1 - 3M) \partial_X^2 (\tilde{A}^2), \quad (12a)$$

$$\partial_T \tilde{A} = -\partial_X^2 \left[\frac{D_u f_v}{b} \tilde{A} + \frac{D_u^2 f_v}{b f_u} \partial_X^2 \tilde{A} - \frac{D_u b^2}{f_u} \tilde{A}^3 \right]. \quad (12b)$$

Returning to the original scales x and t finally leads to the amplitude equation

$$\begin{aligned} \partial_t A = & -D_u \partial_x^2 \left[\frac{f_v}{b} (\varepsilon \tilde{A} + \frac{D_u}{f_u} \partial_x^2 A) \right. \\ & \left. - \frac{b}{f_u} [(3M - 1)A^2 + bA^3] \right] \end{aligned} \quad (13)$$

as given by Eq. (14) of the main text.

II. CH-MODEL FOR CHEMOTACTICALLY COMMUNICATING CELLS

We start with a modified Keller-Segel model from the main text

$$\partial_t \tilde{\rho} = \partial_x^2 \tilde{\rho} - s \partial_x \left(\frac{\tilde{\rho}}{1 + \beta \tilde{\rho}} \partial_x \tilde{c} \right), \quad (14a)$$

$$\partial_t \tilde{c} = D_c \partial_x^2 \tilde{c} + \tilde{\rho} - \tilde{c}. \quad (14b)$$

The homogeneous basic state is given by

$$\rho_h = c_h. \quad (15)$$

Linear stability analysis of the homogeneous state results in two eigenvalues for the perturbation growth rate σ_{\pm} ,

$$\sigma_{\pm} = \frac{1}{2} \left[\gamma_1 \pm \sqrt{1 + 2q^2 \gamma_2 + q^4 \gamma_3^2} \right], \quad (16)$$

where

$$\begin{aligned} \gamma_1 = & -1 - q^2(1 + D_c), \\ \gamma_2 = & D_c - 1 + 2sh\rho_h, \\ \gamma_3 = & D_c - 1. \end{aligned} \quad (17)$$

The eigenvalue σ_- is always negative for small values of q . We expand σ_+ with respect to q^2 and find

$$\sigma_+ = G_2 q^2 - G_4 q^4 + \mathcal{O}(q^6), \quad (18)$$

where

$$\begin{aligned} G_2 = & sh\rho_h - 1, \\ G_4 = & sh\rho_h (sh\rho_h + D_c - 1). \end{aligned}$$

We apply the perturbative method as described in the main text and solve the equations hierarchically. The signaling field c follows the density ρ adiabatically. The

fields c_i in the different orders of ε are thus determined by

$$\begin{aligned} c_1 = & \rho_1, \\ c_2 = & \rho_2, \\ c_3 = & D_c \partial_x^2 c_1 + \rho_3. \end{aligned} \quad (19)$$

For the density we obtain in the lowest order $\mathcal{O}(\varepsilon^{3/2})$

$$0 = (1 - s_c h \rho_h) \partial_x^2 \rho_1. \quad (20)$$

Due to the instability criterion this equation is fulfilled trivially. In the next order $\mathcal{O}(\varepsilon^2)$, we find

$$\begin{aligned} \partial_{T_3} \rho_1 = & (1 - s_c h \rho_h) \partial_x^2 \rho_2 - s_c h^2 \left[\rho_1 (\partial_x^2 \rho_1) + (\partial_x \rho_1)^2 \right] \\ = & -\frac{1}{2} s_c h^2 \partial_x^2 (\rho_1^2), \end{aligned} \quad (21)$$

where we again applied the instability condition. At $\mathcal{O}(\varepsilon^{5/2})$ the relevant terms are

$$\begin{aligned} \partial_T \rho_1 = & -D_c s_c h \rho_h \partial_x^4 \rho_1 - s_c h \rho_h \partial_x^2 \rho_1 \\ & + s_c \beta h^3 \left[\rho_1^2 (\partial_x^2 \rho_1) + 2\rho_1 (\partial_x \rho_1)^2 \right] \\ = & -D_c \partial_x^4 \rho_1 - \partial_x^2 \rho_1 + \frac{1}{3} s_c \beta h^3 \partial_x^2 (\rho_1^3). \end{aligned} \quad (22)$$

Going back to the original time and spatial scales by setting $\partial_t \rho_1 = \varepsilon^{3/2} \partial_{T_3} \rho_1 + \varepsilon^2 \partial_T \rho_1$, and $\tilde{\partial}_x^2 = \varepsilon \partial_x^2$, and choosing $\rho = \sqrt{\varepsilon} \rho_1$ yields

$$\partial_t \rho = -\tilde{\partial}_x^2 \left[\varepsilon \rho + D_c \tilde{\partial}_x^2 \rho + \frac{1}{2} s_c h^2 \rho^2 - \frac{1}{3} s_c \beta h^3 \rho^3 \right]. \quad (23)$$

III. SIMULATION METHODS

We solve the cell polarization model (2) numerically by using a pseudo-spectral method. We calculate all spatial derivatives by transformation to a suitable function space depending on the boundary conditions. For periodic boundaries (i.e. $u|_{x=0} = u|_{x=L}$, $v|_{x=0} = v|_{x=L}$, where L is the system length), we use Fourier representations of the fields. For Figs. 1-5 in the main text, we use a system length $L = 200$ and $N = 256$ modes in Fourier space. As an initial condition, we use a step-like function of the form

$$u(x) = A(\tanh[x - x_l]/\delta] - \tanh[x - x_r]/\delta]) - C,$$

where we choose C such that $\int_0^L u(x) dx = 0$ to fulfill the conservation law. We let this initial condition relax to a steady state. These steady state solutions are shown in Fig. 1 and Fig. 3 and are also used to calculate the plateau values for different ε and M values in Fig. 3, Fig. 4 and Fig. 5, respectively (all references refer to the main text). Fig. 1 and Fig. 3 shows only one half of the system. The second half is axially symmetric and thus

does not contain additional information. Note that due to this inherent symmetry of the profiles, the result for periodic boundary conditions with a system size L are equivalent to those with no flux boundaries and half the system size.

IV. DISCUSSION: EFFECTS OF STRONG ASYMMETRIES

Fig. 5 in the main text shows a comparison between results of the full cell polarization model and its approximation via the CH model as a function of the parameter M (corresponding to the asymmetry). We found that the CH model deviates from the full model for stronger asymmetries. There are two main reasons for that: First, the amplitude calculated from the field v is defined as

$$A_v = \frac{v_h - v}{f_u}, \quad (24)$$

- compare also to Eq. (9). f_u according to Eq. (6a) has its maximum for the symmetric case $M = 1/3$ and decreases when M deviates from this value. These small values of f_u strongly amplify small differences between the field v and the CH model when calculating the amplitude via Eq. (24). A second problem causing deviations of the CH model at stronger asymmetries is illustrated in Fig. 1. For stronger asymmetries the homogeneous basic state of the full system deviates from the analytical calculation as given by Eqs. (3a) and (3b). Therefore, the homogeneous part of the solution in the full system does not match the v_h used to determine A_v . This even explains the seemingly contradictory negative values of the amplitude modulus in Fig. 5 of the main text. Note that the homogeneous parts deviate from the theoretical values for both fields u and v for strong asymmetries. However, the derivative f_v needed to calculate the amplitude from field u is an order of magnitude larger than f_u . Thus, small deviations are much more strongly amplified for the amplitude calculated from field v .

V. HIGHER ORDER NONLINEARITIES VERSUS INTEGRABILITY

In Ref. [41] the so-called ‘active model B’ was introduced as an expansion of the classic CH model for active particles. As mentioned in the main text, the additional nonlinearity $\Delta(\nabla A)^2 \propto \varepsilon^3$ is of higher order compared to the amplitude-limiting nonlinearity of the Cahn-Hilliard model, $\alpha_4 \Delta A^3 \propto \varepsilon^{5/2}$ (where $\alpha_4 > 0$ and $\alpha_4 \sim \mathcal{O}(1)$). This additional nonlinearity becomes negligible close to threshold and it is not generic.

Nevertheless, if this nonlinearity is taken into account, by systematic reasons one would also have to take into account the following second nonlinearity of the same order, $\Delta(A \Delta A) \propto \varepsilon^3$. The CH model extended by both

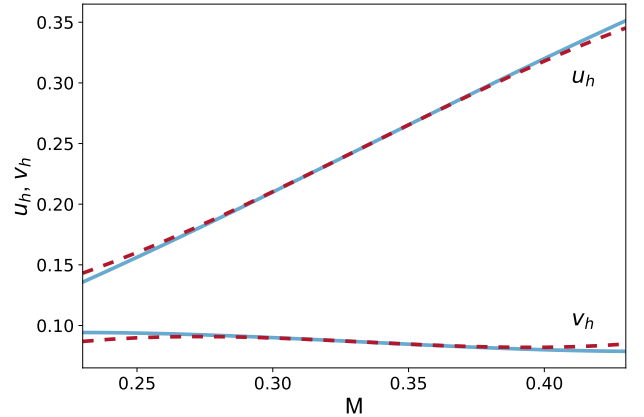


FIG. 1. Basic states u_h and v_h as a function of the asymmetry parameter M . The theoretical values (solid line) deviate from those of the full system (dashed line) for strong asymmetries.

nonlinearities takes the following form:

$$\partial_t A = -\partial_x^2 \left[\alpha_1 \varepsilon A + \alpha_2 \partial_x^2 A - \alpha_3 A^2 - \alpha_4 A^3 \right] - \partial_x^2 \left[\lambda_1 (\partial_x A)^2 + \lambda_2 (A \partial_x^2 A) \right]. \quad (25)$$

This equation can be derived from a potential via

$$\partial_t A = -\frac{\partial^2}{\partial x^2} \frac{\delta \mathcal{F}}{\delta A} \quad (26)$$

with

$$\mathcal{F} = \int dx \left\{ -\varepsilon \frac{\alpha_1 A^2}{2} + \frac{\alpha_3 A^3}{3} + \frac{\alpha_4 A^4}{4} + \frac{\alpha_2}{2} (\partial_x A)^2 + \gamma_1 A^2 \partial_x^2 A + \gamma_2 A (\partial_x A)^2 \right\} \quad (27)$$

and the following parameter combination:

$$\lambda_2 = 2\lambda_1 \quad \text{and} \quad \lambda_1 = 2\gamma_2 - \gamma_1. \quad (28)$$

Therefore, taking the next higher order nonlinearities into account in a systematic expansion (similar to the one we present in the main text) does not necessarily imply that the resulting model become nonintegrable. In addition, the two mentioned higher order nonlinearities are non-generic within a systematic expansion and vanish by approaching the onset of active phase separation.

Universal aspects of collective behavior in chemotactic systems

Lisa Rapp and Walter Zimmermann

Universal aspects of collective behavior in chemotactic systems

Lisa Rapp and Walter Zimmermann

Theoretische Physik I, Universität Bayreuth, 95440 Bayreuth, Germany

(Dated: March 29, 2019)

We investigate the collective dynamics of particles (e.g. microorganisms) interacting via chemotactic gradients. Specifically, we focus on continuum models for chemotaxis that include a damping of the chemical production with increasing local particle density and/or systems where the chemotactic sensitivity is reduced with increasing local concentration of the chemical. Using a recently introduced perturbative method [Phys. Rev. E 98, 020603 (2018)], we show that the onset of particle clustering in these systems is described by the universal Cahn-Hilliard (CH) model. On the one hand, this establishes particle-conserving models for chemotaxis as a further example for the universal class of non-equilibrium demixing phenomena we call active phase separation. On the other hand, the reduction to the CH model allows an analytical determination of suitable parameter ranges wherein, e.g., the transition to spatial density modulations is continuous and/or undesired blow-up solutions can be avoided. A comparison between the numerical solutions of the chemotaxis model and the derived CH model also provides the parameter range where the basic chemotaxis model behaves like other systems showing active phase separation, including the coarsening behavior in two spatial dimensions. Our approach highlights how basic principles of pattern formation theory allow the identification of common basic properties in different chemotaxis models.

I. INTRODUCTION

The directed motion of microorganisms and cells along concentration gradients of signal molecules is known as chemotaxis [1–3]. Chemotaxis plays a critical role in the life cycle of both bacteria and multicellular organisms: From foraging to wound healing and cancer growth [4] to the formation of fruiting bodies in the social amoeba *Dictyostelium discoideum* [5]. Chemotaxis is also mimicked in synthetic systems using catalytically active phoretic colloids (see e.g. Refs. [6, 7]). Microorganisms, cells or active autophoretic colloids produce and detect a chemical concentration field and communicate via this field.

Keller and Segel (KS) introduced a commonly used continuum model for the interplay between the particle density and a chemical concentration field [8, 9]. The KS model includes particle movement via a diffusive flux and an advective flux with the particle velocity depending on the gradient of the concentration field. The chemical signal production, in turn, is proportional to the cell density. With these ingredients, the model displays so-called 'auto-aggregation' and thus serves as a simple model for the onset of cell clustering. Beyond the onset of cell aggregation, however, the classic KS model can show unrealistic behavior. So-called blow-up solutions, for example, result in huge particle densities. That is why different extensions of the KS model incorporating additional aspects of cell clustering have been developed and explored in recent years (see e. g. [11, 12]). One extension is based on the idea of nonlinear signal molecule kinetics leading to saturation of the chemical signal production with increasing particle density [12, 13]. This prevents excessive chemoattractant production, thereby limiting the amplitudes of the involved fields. Another variant includes signal-dependent chemotactic sensitivity, i.e. a dependence of the particle velocity on the concentration of the chemical fields. The underlying as-

sumption based on experimental observations is that the chemotactic sensitivity saturates for high concentrations of signal molecules, e.g. due to receptor-signal binding [12]. Generalized models of chemotaxis have also recently been used to describe clustering dynamics in colloidal active matter systems [10]. This work used an extended KS variant with a contribution for anisotropic production of the chemical concentration field. Here, we investigate a generalized chemotaxis model that includes all three above-mentioned extensions of the classic KS model.

The cell density patterns described by these models usually arise and disappear in less than a generation time of the cells. Thus, the number of cells is roughly conserved during the pattern formation process. Additionally, the instability of homogeneous concentration fields is of the so-called type II [15], i.e. perturbations follow a growth rate dispersion of the form $\sigma = G_1 q^2 - G_2 q^4$. In particular, this means that long wavelength perturbations are not damped. With these two criteria fulfilled, chemotactic clustering is a suitable candidate for the recently introduced generic class of active phase separation [14]. In Ref. [14], we showed that the universal order parameter equation near the onset of active phase separation is the Cahn-Hilliard (CH) model [16, 17]. Other examples of these nonequilibrium demixing phenomena include cell polarization [18–21] or motility-induced phase separation (MIPS) of active colloidal particles [23–27]. For an exemplary cell polarization model [18] and a mean-field model for MIPS [27], we were recently able to show that these examples also belong to the class of active phase separation [22, 28]. Does - and if so under which circumstances - chemotactic cell clustering also belong to the class of active phase separation?

To answer this question, this work is organized as follows: We first introduce the continuum model of chemotactic clustering in Sec. II and analyze the linear stability of homogeneous particle/cell densities. In Section III, we

use a perturbative scheme to reduce the mean-field model to the universal CH equation for active phase separation and discuss suitable system parameters. Finally, in Section IV, we compare the numerical solutions of the basic chemotaxis model with the solutions of the derived CH model and estimate the validity range of the reduction to the CH model. We also compare exemplarily the typical coarsening behavior of clustering dynamics in two spatial dimensions.

II. A GENERALIZED CONTINUUM MODEL FOR CHEMOTAXIS

We investigate a generalized continuum model for chemotaxis (GCM) that merges three previously used extended Keller-Segel models [10–12]. It describes the dynamics of a density field $\tilde{\rho}(\mathbf{r}, t)$ representing the density of the chemotactic cells or active colloidal particles. Note that $\tilde{\rho}$ is a conserved quantity. The density field is coupled to the concentration \tilde{c} of a chemoattractant (or signal molecules):

$$\partial_t \tilde{\rho} = \partial_x^2 \tilde{\rho} - s \partial_x \left(\frac{\tilde{\rho}}{(1 + \beta \tilde{c})^2} \partial_x \tilde{c} \right), \quad (1a)$$

$$\partial_t \tilde{c} = D_c \partial_x^2 \tilde{c} + s \kappa \partial_x (\tilde{\rho} \partial_x \tilde{c}) + \frac{\tilde{\rho}}{1 + a \tilde{\rho}} - \tilde{c}. \quad (1b)$$

In the first equation, the diffusion constant is scaled to unity. D_c in the second equation thus describes the ratio between the diffusion constants of $\tilde{\rho}$ and \tilde{c} . The coefficient s is a measure for the chemotactic drift. For $\beta \neq 0$, the model takes into account the dependence of the effective chemotactic drift on the chemoattractant concentration (see Ref. [12] and references therein): For $\beta > 0$, the chemotactic sensitivity decreases with increasing density of the chemoattractant. For finite values of the parameter a , the model includes a reduction of the local signal production with increasing density $\tilde{\rho}$ [12, 13]. This essentially prevents further accumulation at high local particle densities. For $\kappa \neq 0$, the model also includes anisotropic production of the chemoattractant. This is considered important when chemotactic continuum models are used for modeling active colloids [10]. For $\kappa = a = \beta = 0$, Eqs. (1a) and (1b) reduce to the original Keller-Segel model [8, 9].

The homogeneous cell (colloid) density ρ_0 defines the chemoattractant concentration c_0 of the homogeneous basic state:

$$c_0 = \frac{\rho_0}{1 + a \rho_0}. \quad (2)$$

Next we separate the homogeneous part from the inhomogeneous parts of both concentrations:

$$\begin{aligned} \tilde{\rho}(x, t) &= \rho_0 + \rho(x, t), \\ \tilde{c}(x, t) &= c_0 + c(x, t). \end{aligned} \quad (3)$$

In the resulting equations we take the fields $\rho(x, t)$ and $c(x, t)$ up to their cubic power into account:

$$\begin{aligned} \partial_t \rho &= \partial_x^2 \rho - s \rho_0 \partial_x^2 c \\ &\quad - s h^2 \partial_x [(\rho - 2\beta h \rho_0 c + 3\beta^2 h^2 \rho_0 c^2 - 2\beta h \rho c) \partial_x c], \end{aligned} \quad (4a)$$

$$\begin{aligned} \partial_t c &= (D_c + s \kappa \rho_0) \partial_x^2 c + s \kappa \partial_x (\rho \partial_x c) \\ &\quad + g^2 (\rho - a g \rho^2 + a^2 g^2 \rho^3) - c, \end{aligned} \quad (4b)$$

where

$$g = \frac{1}{1 + a \rho_0} \quad \text{and} \quad h = \frac{1}{1 + \beta c_0}. \quad (5)$$

A. Linear stability of basic state

We assume small inhomogeneous perturbations $\rho(x, t)$ and $c(x, t)$ of the basic state and keep only linear contributions in Eqs. (4). For the resulting linear equations we choose the ansatz $\rho = \bar{\rho} \exp(\lambda t + i q x)$ and $c = \bar{c} \exp(\lambda t + i q x)$ with the growth rate λ and wavenumber q . This determines the growth rate λ :

$$\lambda_{\pm} = \frac{1}{2} \left[\gamma_1 \pm \sqrt{1 + 2q^2 \gamma_2 + q^4 \gamma_3^2} \right] \quad (6)$$

with the coefficients

$$\gamma_1 = -1 - q^2 (1 + D_c + s \kappa \rho_0), \quad (7)$$

$$\gamma_2 = D_c - 1 + s \rho_0 (2g^2 h^2 + \kappa), \quad (8)$$

$$\gamma_3 = D_c - 1 + s \rho_0 \kappa. \quad (9)$$

The second eigenvalue λ_{\pm}^{\approx} is always negative for small values of q . It is thus irrelevant to the question of linear stability of the homogeneous state. Expanding λ_{+} up to leading order of the wavenumber q , we find

$$\lambda_{+}^{\approx} = G_2 q^2 - G_4 q^4 + O(q^6) \quad (10)$$

with

$$G_2 = (s \rho_0 g^2 h^2 - 1), \quad (11a)$$

$$G_4 = s \rho_0 g^2 h^2 [s \rho_0 (g^2 h^2 + \kappa) + D_c - 1]. \quad (11b)$$

The coefficient G_2 vanishes for $s = s_c$, where

$$s_c = \frac{1}{\rho_0 g^2 h^2}. \quad (12)$$

If $s > s_c$, the coefficient G_2 also becomes positive and thus the growth rate λ_{+}^{\approx} becomes positive in a finite range of q . Furtheron s is chosen as the control parameter in this system. As the dimensionless control parameter, we choose ε with

$$s = s_c (1 + \varepsilon). \quad (13)$$

With this choice we obtain $G_2 = \varepsilon$. Therefore, the growth rate becomes positive for $\varepsilon > 0$ in a finite range $0 < q < q_0$ with $q_0^2 = \varepsilon / G_4$.

Figure 1 shows the growth rates - both the full growth rate λ_+ as given in Eq. (6), as well as its approximation in Eq. (10). To simplify the following calculations, we determined the onset of clustering from the approximated growth rate. Figure 1 suggests that close to the transition - when the growth rate first becomes positive - the approximation is in good agreement with the full growth rate as given in Eq. (6).

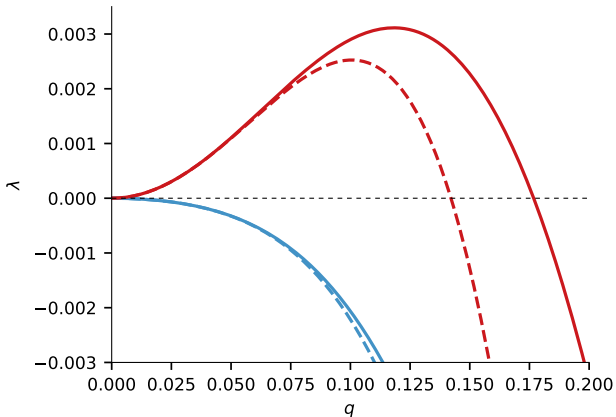


FIG. 1. Comparison of the growth rate $\lambda_+(q)$ given by Eq. (6) (solid lines) and its approximation λ_+^{\approx} up to 4th order in q as given by Eq. (10) (dashed lines). The growth rate is negative for $s < s_c$ and positive for $s > s_c$ within a finite range of wavenumbers.

III. DERIVATION OF THE CAHN-HILLIARD MODEL

In this section, we first derive in Sec. (III A) the Cahn-Hilliard model from the basic equations (4) in the neighborhood of the threshold s_c . In Sec. IIIB, we then discuss the obtained results including certain aspects of its possible solutions.

A. Perturbative expansion

In order to further describe the clustering process beyond s_c often simulations of the coupled equations (1) are used. Here, we proceed analytically and derive an order parameter equation near the onset s_c via a recently introduced perturbative expansion [14]. Immediately beyond onset s_c , the growth rate is only positive in a range of small values of the wavenumber q , specifically for $[0 < q < q_0]$ with $q_0 \propto \sqrt{\epsilon}$. In this range the growth rate is also small, more specifically $\sigma \propto \epsilon^2$. Accordingly the spatial variations take place on large length scales and the temporal dynamics are slow. Therefore, we introduce a the new spatial scale $X = \epsilon x$, as well as the slow time scales $T_1 = \epsilon^{3/2}t$ and $T = \epsilon^2t$. This gives rise

to the following replacements for the spatial and temporal derivatives [15, 29]:

$$\begin{aligned} \partial_x &\rightarrow \sqrt{\epsilon} \partial_X, \\ \partial_t &\rightarrow \epsilon^{3/2} \partial_{T_1} + \epsilon^2 \partial_T. \end{aligned} \quad (14)$$

We assume that the transition from the homogeneous to the phase separated state is continuous. Accordingly, we choose the following expansion for the density and concentration fields:

$$\rho = \epsilon^{1/2} \rho_1 + \epsilon \rho_2 + \epsilon^{3/2} \rho_3 + \dots, \quad (15)$$

$$c = \epsilon^{1/2} c_1 + \epsilon c_2 + \epsilon^{3/2} c_3 + \dots. \quad (16)$$

Usually the chemoattractant diffuses much faster than the particles or cells. The chemoattractant concentration c thus essentially follows the density ρ adiabatically. In this case, we can express the densities c_i as functions of the densities ρ_i by solving the successive orders $\epsilon^{1/2}, \epsilon, \epsilon^{3/2}$ of Eq. (4b) as follows:

$$c_1 = g^2 \rho_1, \quad (17a)$$

$$c_2 = g^2 \rho_2 - a g^3 \rho_1^2, \quad (17b)$$

$$c_3 = \tilde{D} \tilde{\partial}_x^2 c_1 + g^2 \rho_3 - 2a g^3 \rho_1 \rho_2 + a^2 g^4 \rho_1^3. \quad (17c)$$

Note that $\tilde{\partial}_x$ denotes the derivation to the slow spatial variables X and Y , and $\tilde{D} = D_c + s_c \kappa \rho_0$.

Next we consider the successive orders $\sqrt{\epsilon}^n$ in Eq. (4a). At order $\epsilon^{3/2}$, we find

$$0 = (1 - s_c \rho_0 g^2 h^2) \tilde{\partial}_x^2 \rho_1. \quad (18)$$

Due to the instability condition in Eq. (12), this equation is trivially fulfilled. Hence, ρ_1 and c_1 are both undetermined at this order. At order ϵ^2 we have

$$\begin{aligned} \partial_{T_1} \rho_1 &= (1 - s_c \rho_0 g^2 h^2) \tilde{\partial}_x^2 \rho_2 \\ &+ \frac{1}{2} s_c g^2 h^2 (2\beta \rho_0 g^2 h + 2a \rho_0 g - 1) \tilde{\partial}_x^2 (\rho_1^2). \end{aligned} \quad (19)$$

Using again the instability condition in Eq. (12), we gain an equation for the time development of ρ_1 on the slow time scale T_1 that is determined by the quadratic non-linearity,

$$\partial_{T_1} \rho_1 = \alpha_3 \tilde{\partial}_x^2 (\rho_1^2), \quad (20)$$

where

$$\alpha_3 = \frac{1}{2} s_c g^2 h^2 (2\beta \rho_0 g^2 h + 2a \rho_0 g - 1). \quad (21)$$

At the next higher order $\epsilon^{5/2}$ we obtain

$$\begin{aligned} \partial_{T_1} \rho_2 + \partial_T \rho_1 &= (1 - s_c \rho_0 g^2 h^2) \tilde{\partial}_x^2 \rho_3 - \tilde{D} \partial_x^4 \rho_1 - \tilde{\partial}_x^2 \rho_1 \\ &- s_c g^3 h^2 (a + \beta g h) \left(\beta \rho_0 g^2 h + a \rho_0 g - \frac{2}{3} \right) \tilde{\partial}_x^2 (\rho_1^3) \\ &+ \mathcal{F}(\rho_1, \rho_2). \end{aligned} \quad (22)$$

Omitting any terms including ρ_2 since they should become irrelevant near threshold, we end up with

$$\partial_T \rho_1 = -\tilde{D} \partial_x^4 \rho_1 - \tilde{\partial}_x^2 \rho_1 + \alpha_4 \tilde{\partial}_x^2 (\rho_1^3), \quad (23)$$

where

$$\alpha_4 = s_c g^3 h^2 (a + \beta gh) \left(\frac{2}{3} - \beta \rho_0 g^2 h - a \rho_0 g \right). \quad (24)$$

Going back to the original time and spatial scales by setting $\partial_t \rho_1 = \varepsilon^{3/2} \partial_{T1} \rho_1 + \varepsilon^2 \partial_T \rho_1$, and $\partial_x^2 = \varepsilon \tilde{\partial}_x^2$, and choosing $\rho = \sqrt{\varepsilon} \rho_1$ yields

$$\partial_t \rho = -\partial_x^2 \left[\varepsilon \rho + \tilde{D} \partial_x^2 \rho - \alpha_3 \rho^2 - \alpha_4 \rho^3 \right]. \quad (25)$$

This equation has the form of the Cahn-Hilliard model [16, 17] with an additional quadratic nonlinearity.

B. Discussion of the derived Cahn-Hilliard equation

Linear stability analysis similar as described in Sec. II A shows that perturbations with respect to the homogeneous state $\rho = 0$ in Eq. (25) grow according to the growth rate

$$\lambda_{CH} = \varepsilon q^2 - \tilde{D} q^4, \quad (26)$$

where $\tilde{D} = D_c + s_c \kappa \rho_0$. Comparing this to Eq. (10), the growth rate for the full generalized chemotaxis model (GCM), the quadratic contributions are in agreement. The contribution G_4 in the full model tends to \tilde{D} for $\varepsilon \rightarrow 0$. Thus, the CH model is able to reproduce the linear growth behavior of the full model in the limit of small ε .

Equation (25) results in stationary solutions with finite amplitudes if the saturation coefficient α_4 is positive. In the absence of dampings, $a = \beta = 0$, we find $\alpha_4 = 0$. This opens up the possibility of numerical blow-up solutions. The saturation coefficient already becomes positive if the model includes a small finite damping term in either the signal production or the chemotactic sensitivity. Thus, in order to avoid blow-up, we should demand $\alpha_4 > 0$ by choosing at least one of the damping terms a or β to be finite. However, for increasing values a, β , the saturation coefficient is only positive in the range

$$\rho_0 g (a + \beta gh) < \frac{2}{3}. \quad (27)$$

With the definitions in Eq. (2) and Eq. (5), this simplifies to

$$(a + \beta) \rho_0 < 2. \quad (28)$$

If this condition is not fulfilled, the amplitudes of the density ρ are not limited by the cubic nonlinearity. Thus,

description of the demixing phenomena via the CH model becomes invalid if the mean density ρ_0 exceeds a certain value (which depends on the damping parameters a, β). Alternatively, the damping parameters a or β need to be sufficiently small - corresponding to a finite but sufficiently weak damping.

If $\alpha_4 < 0$, the CH model is obviously not a good representation of the full system dynamics. Since the solution does not saturate at leading order in this case, higher order nonlinearities will quickly become important. They can be taken into account by continuing the perturbative expansion presented here to the higher orders ε^3 or $\varepsilon^{7/2}$ (see also [28]). Note that these higher order nonlinearities could potentially serve as saturating terms. This could prevent blow-up even if $\alpha_4 < 0$. However, systems of this type do not belong to the class of active phase separation we discuss here.

Equation (25) is $\pm\rho$ -symmetric if the quadratic nonlinearity vanishes, i.e. if $\alpha_3 = 0$. Using Eq. (21), this condition is fulfilled if

$$2\rho_0 g (a + \beta gh) = 1, \quad (29)$$

which simplifies to

$$(a + \beta) \rho_0 = 1. \quad (30)$$

For given damping parameters a, β there is thus a specific mean density

$$\rho_{sym} = \frac{1}{a + \beta} \quad (31)$$

that leads to symmetric phase separation. In this case, the condition in Eq. 28 is fulfilled and thus $\alpha_4 > 0$. Consequently, Eq. 31 is the condition for a continuous transition to active phase separation with finite steady-state amplitudes. Note that the symmetric case cannot be achieved if $a = \beta = 0$, i.e. in the classic KS model.

In the symmetric case ($\alpha_3 = 0$) and in long systems, a possible steady state solution of Eq. (25) is the domain wall solution

$$\rho(x) = \sqrt{\frac{\varepsilon}{\alpha_4}} \tanh\left(\frac{x}{\sqrt{2}\ell}\right), \quad (32)$$

with the coherence length ℓ

$$\ell = \frac{\xi_0}{\sqrt{\varepsilon}}, \quad \xi_0 = \sqrt{D_c + s_c \kappa \rho_0}. \quad (33)$$

This solution again requires $\alpha_4 > 0$.

IV. NUMERICAL RESULTS

In this section we determine steady state solutions of the full GCM in Eqs. (4), and the reduced CH model in Eq. (25) (see Appendix A for simulation details). As discussed in the previous section, we choose the system

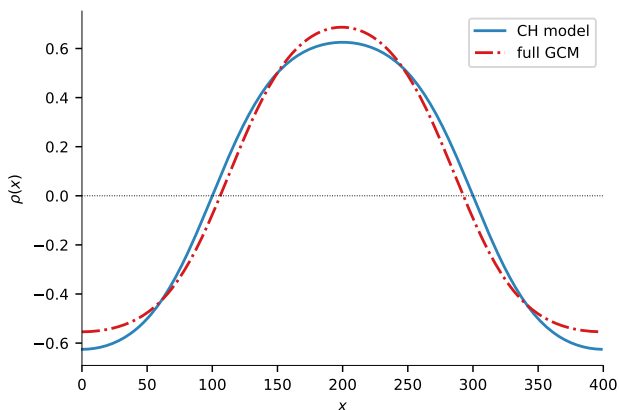


FIG. 2. The steady state cell-density $\rho(x)$ is shown very close to threshold at $\varepsilon = 0.01$ for the full GCM in Eqs. (4) (dashed-dotted line) and for the symmetric case of the reduced model in Eq. (25) (solid line).

parameters such that $\alpha_4 > 0$. This can be achieved by either a reduction of the signal production, i.e. $a > 0$, or by a reduction of the drift sensitivity with increasing density of the chemoattractant, i.e. $\beta > 0$ (or a combination of both damping mechanisms). In the following, we will thus consider exemplarily the case of a reduction of the chemoattractant production with $a = 0.5$ and $\beta = 0$. Other system parameters used are $\kappa = 1.0$ and $D_c = 10.0$. Note that we use a large (relative) diffusion coefficient (i.e. $D_c \gg 1$), as the small chemical molecules usually diffuse much faster than the cells. This also justifies the adiabatic approximation used in the previous chapter.

A. Symmetric phase separation

We first investigate the case $\rho_0 = 2$ where the quadratic nonlinearity in Eq. (25) vanishes, i.e., $\alpha_3 = 0$ for $a = 0.5$ and $\beta = 0$. The CH equation then has solutions that are symmetric around the average density ρ_0 .

Figures 2 and 3 show the steady state solutions of both the full GCM (dashed-dotted line) and the reduced CH model (solid line) for two different supercritical values of the control parameter, $\varepsilon = 0.01$ and $\varepsilon = 0.1$, respectively. The CH model shows a symmetric separation into two phases ρ_{min} and ρ_{max} . I.e. the extremal values of the density, ρ_{min} and ρ_{max} , deviate equally from the mean density ρ_0 with each phase occupying about half of the system. Close to the onset of phase separation at $\varepsilon = 0.01$, the solution resembles a cosine where the wavelength equals the system size. As Fig. 2 shows, the solution of the full model is very similar to the reduced model. However, the solution is already slightly asymmetric. Further from the onset of phase separation ($\varepsilon = 0.1$, Fig. 3), the transition between the two

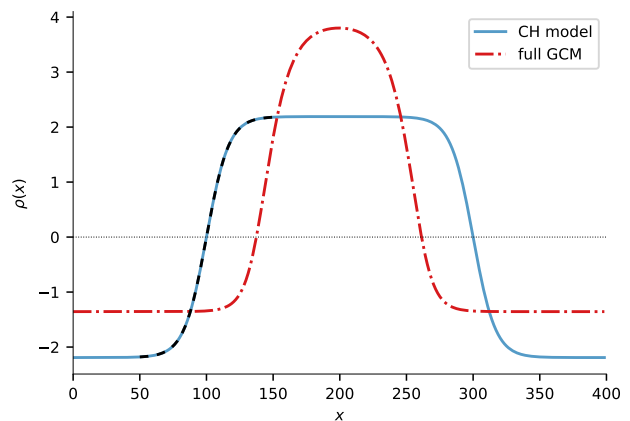


FIG. 3. The steady state cell-density $\rho(x)$ is shown further beyond threshold at $\varepsilon = 0.1$ for the full GCM in Eqs. (4) (dashed-dotted line) and the symmetric case of the reduced model given by Eq. (25) (solid line). The solution of the CH model is nearly identical to the domain wall solution given by Eq. (32) (dashed line).

phases becomes more step-like. The solution of the CH model remains symmetric with the transition between the two phases following the domain wall solution given by Eq. (32). The full model, however, becomes more asymmetric with increasing ε , thus deviating more from the CH model. These deviations have its origin in the approximations used for the derivation of the CH model: we only took contributions up to cubic power in ρ and c in the basic equations into account. In the limit $\alpha_3 = 0$ the contributions of ρ^2 and c^2 vanish by construction. However, with increasing values of ε higher order contributions such as ρ^4 and c^4 may become increasingly relevant for the full model in Eq. (1). Higher order terms of even power break the \pm -symmetry, i.e. deviations of $\rho_{min,max}$ from ρ_0 are not symmetric anymore (see dashed-dotted lines in Fig. 2 and Fig. 3).

For smaller values of the control parameter ε , approaching the onset of phase separation, the solutions of the GCM and the CH model become nearly indistinguishable. The full model then also approaches symmetric solutions. This is indicated in Fig. 4 that shows the deviations ρ_{max} and $|\rho_{min}|$ from ρ_0 as a function of the control parameter ε . On the one hand, this tells us that the CH model is an excellent approximation of the full Keller-Segel model in the range of small ε . This is further proof that the full model belongs to the class of active phase separation described by the CH model at onset. On the other hand, the numerical solutions confirm the prediction that the transition to clustering is continuous for $\alpha_4 > 0$ and $\alpha_3 = 0$. Note that in an infinite system the onset of the clustering is at $\varepsilon = 0$. However, in a confined system, as shown here for $L = 400$, the clustering onset is slightly increased.

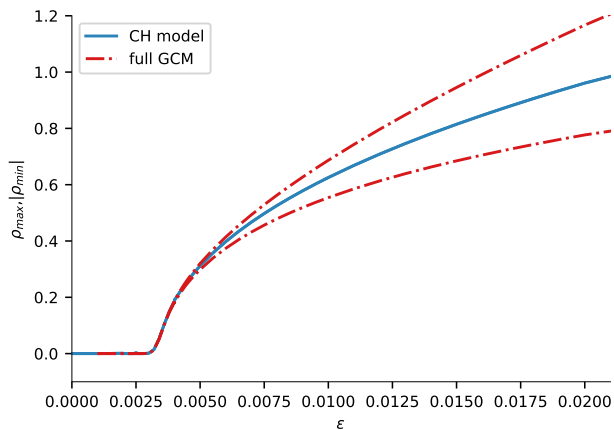


FIG. 4. Comparison of the maximum and modulus of the minimum amplitude in the full GCM (dashed-dotted line) to the reduced CH equation (solid line) in the symmetric case ($\rho_0 = 2$).

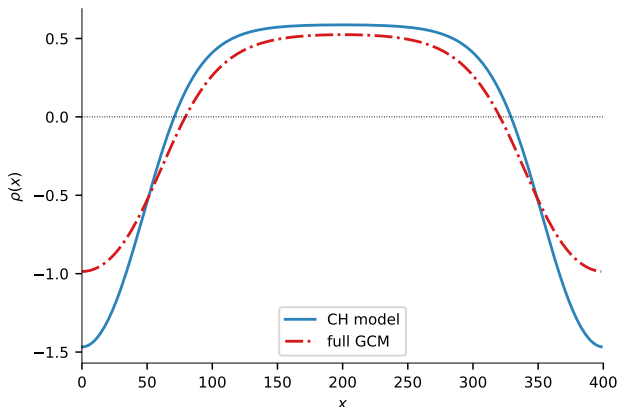


FIG. 5. Typical steady state solutions $\rho(x)$ in the case of asymmetric phase separation, i.e. $\alpha_3 \neq 0$. Solution of the full GCM in Eqs. (4) (dashed-dotted line) compared to the derived CH model (solid line) for $\varepsilon = 0.003$, $\rho_0 = 2.5$.

B. Asymmetric phase separation

For $\rho_0 \neq 2$, the quadratic nonlinearity in Eq. (25) is finite. Thus, the \pm -symmetry of the CH model is broken. As a result, we expect an asymmetric phase separation process where $\rho_{max} \neq |\rho_{min}|$. Figure 5 shows these asymmetric solutions for the full KS model, as well as the CH model for $\varepsilon = 0.003$ and $\rho_0 = 2.5$. The solutions are very clearly asymmetric with $\rho_{max} < |\rho_{min}|$ and the area where $\rho(x) > 0$ now occupying about two thirds of the system. Comparing the full model to its description via the reduced CH model, we find that the CH model is able to predict ρ_{max} fairly well. However, it significantly overestimates $|\rho_{min}|$ even for this rather small control parameter of $\varepsilon = 0.003$.

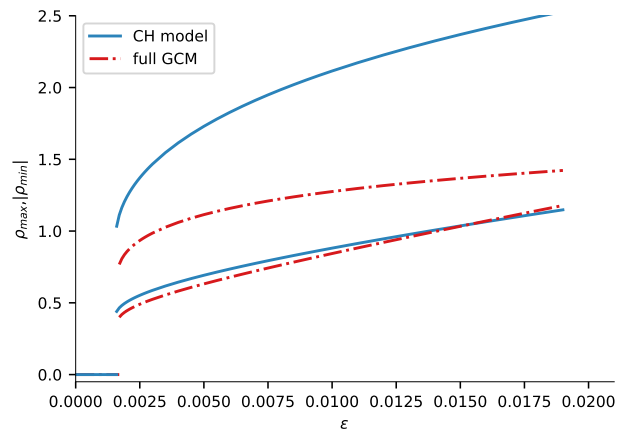


FIG. 6. Comparison of ρ_{max} and $|\rho_{min}|$ in the full model (dashed-dotted line) to the reduced CH equation (solid line) as a function of ε in the case of strongly asymmetric phase separation ($\rho_0 = 2.5$).

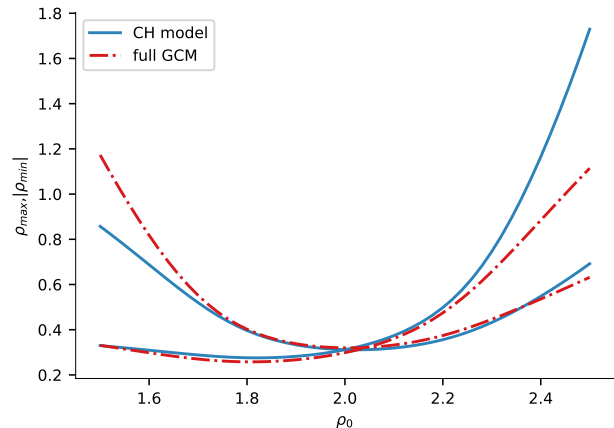


FIG. 7. Maximum and modulus of the minimum amplitude at $\varepsilon = 0.005$ as a function of the mean density ρ_0 for the full model (dashed-dotted line) and the reduced CH model (solid line). The mean density ρ_0 defines the asymmetry of the phase separation via the asymmetry parameter α_3 in Eq. (21).

This observation is consistent when investigating ρ_{max} and $|\rho_{min}|$ as a function of the control parameter (Fig. 6): The smaller deviation from the mean density (in this case ρ_{max}) is similar for both the full model and the reduced CH model. The larger density variation $|\rho_{min}|$, however, is significantly overestimated by the CH model. Most notably, however, the transition to the phase separated state is not continuous anymore. Instead, there is a jump to finite values of ρ_{max} and $|\rho_{min}|$ at the onset. Note that the onset of phase separation is decreased compared to the symmetric case.

Figure 7 shows the variations from the mean density ρ_0 for a fixed value of the control parameter ($\varepsilon = 0.005$) as a function of the mean density ρ_0 . In accordance with pre-

vious results, the minimum and maximum density variation become similar, i.e. the steady state solution becomes symmetric, around $\rho_0 = 2$. In this region, the steady state solutions of the reduced CH model is in good agreement with the results for the full model. As can be calculated analytically, the perfectly symmetric solution in the reduced CH model is reached for $\rho_0 = 2$. The solution for the full model is symmetric for $\rho_0 \approx 2.05$, thus slightly deviating from the reduced model for this finite value of the control parameter ε . For increasing or decreasing values of the mean density ρ_0 , the steady state solution becomes more and more asymmetric. While full model and reduced CH model are in good agreement up to moderate asymmetries. Only for very strong asymmetries do the two solutions deviate more clearly.

The fact that the quality of the approximation via the CH model decreases for strong asymmetries is actually not surprising. In fact, we can estimate the range of ρ_0 values for which we assume the approximation to still be in good agreement with the full model. In order to do so, we assume stationary, spatially homogeneous solutions $\rho = A$ of Eq. (25):

$$\varepsilon - \alpha_3 A - \alpha_4 A^2 = 0. \quad (34)$$

We rescale the amplitude by setting $A = B/\sqrt{\alpha_4}$ in order to get

$$\varepsilon - \frac{\alpha_3}{\sqrt{\alpha_4}} B - B^2 = 0. \quad (35)$$

In the stationary case, the saturation term should balance the first term, suggesting $B^2 \propto \mathcal{O}(\varepsilon)$. If we want to keep the second term of the same order than the other two terms, we have to demand

$$\frac{\alpha_3}{\sqrt{\alpha_4}} \lesssim \sqrt{\varepsilon}. \quad (36)$$

If this condition is fulfilled, we would assume the CH model to be a good approximation for asymmetric phase separation. For the given system parameters, this corresponds to mean densities ρ_0 in a range of about [1.84, 2.16]. As Fig. 7 clearly shows, deviations of the CH approximation from the full model only become apparent well beyond this region of moderate asymmetries.

C. Coarsening in two dimensions

Starting from random initial conditions in two spatial dimensions, both the full GCM in Eqs. (4) and the CH model in Eq. (25) show coarsening dynamics as they are characteristic for phase separation phenomena. The snapshots shown in Fig. 8 at different times are obtained for $\varepsilon = 0.1$, i.e. quite far from phase separation onset. In Fig. 8a) and Fig. 8b), we considered the symmetric case at onset, i.e., $\alpha_3 = 0$. However, the full model is already strongly asymmetric at $\varepsilon = 0.1$ since higher order nonlinearities break the up/down-symmetry in the system. For

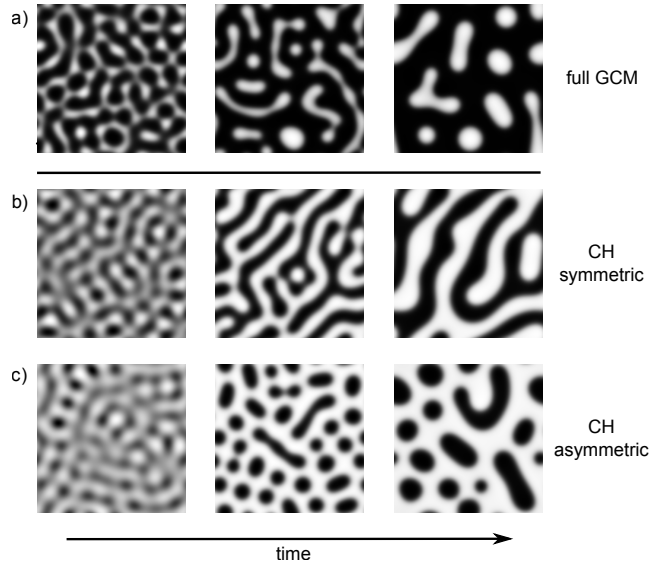


FIG. 8. Simulation results in two dimensions at $\varepsilon = 0.1$ and times $t_1 = 6 \cdot 10^4$, $t_2 = 1.2 \cdot 10^5$ and $t_3 = 3 \cdot 10^5$ (system size: 800×800). In a) snapshots for the full model and in b) for the CH model are shown in the symmetric case, i.e., $\alpha_3 = 0$. Part c) shows the CH model in the asymmetric case $\rho_0 = 2.5$.

comparison, Fig. 8b) shows simulations of the CH model for the same parameters. In this symmetric case, the system shows typical labyrinth-like patterns. Figure 8c) shows simulations of the CH model in the asymmetric case for $\rho_0 = 2.5$. The spot-like patterns seen both here and the full model in Fig. 8a) are typical for asymmetric phase separation.

D. Both dampings

Both damping parameters a and β contribute to the amplitude limitation parameter α_4 and the asymmetry parameter α_3 in Eq. (25). The condition for saturation of the amplitude, $\alpha_4 > 0$, can already be fulfilled by one of both damping parameters. Therefore, we focused in the previous section on a finite $a \neq 0$, as well as an anisotropic signal production, i.e. $\kappa \neq 0$, in order to keep the comparisons between the full and the reduced CH model straightforward. The anisotropy κ only contributes by varying the diffusion constant D_c [see $\tilde{D} = D_c + s_c \kappa \rho_0$ in Eq. (25)]. It thus does not qualitatively influence the stationary solutions obtained in the model. Taking a signal-dependent sensitivity into account ($\beta \neq 0$) - in addition to the nonlinear signal production we already considered in the previous chapter - will change the parameter sets that fulfill the conditions outlined in Section III. Besides these quantitative changes to the CH model and its validity range as an approximation of the full model, $\beta \neq 0$ does not change the qualitative results described in the previous section. Numerical simulations for the parameters $a = 3$, $\beta = 1$,

$D_c = 5$, $\kappa = 0$ confirmed this (see Appendix B).

V. SUMMARY AND CONCLUSIONS

In this work we have analyzed a continuum model for chemotaxis with a globally conserved particle density that is coupled to an unconserved concentration field of a chemoattractant. Compared to the original Keller-Segel (KS) model for chemotaxis, our generalized chemotaxis model (GCM) also saturation of the chemoattractant production with increasing particle density, as well as reduction of the drift sensitivity with increasing chemoattractant density [12]. The model also allows for anisotropic chemical production as used for autophoretic colloids [10]. We showed here that this model belongs to a recently introduced class of active phase separation that can be reduced near onset to the Cahn-Hilliard model.

To obtain this result, we applied a recently introduced perturbation method for mass-conserved systems, cf. Ref. [14], to the continuum model for the collective particle chemotaxis used in this work. Due to the systematic perturbative approach, the coefficients of the CH model are mathematically linked to the system parameters of the GCM, i.e. the coefficients of the CH model are expressed in terms of parameters of the basic model. This direct link also allows us to analytically predict suitable parameter ranges. We can, for example, predict where the transition from homogeneous particle and chemoattractant densities to clustering becomes continuous. We can also show when the cubic nonlinearity in the CH equation limits the amplitude of the density field. This can only be the case if at least one of the included damping effects considered in this work become sufficiently strong. These damping effects thus are obviously able to eliminate undesired blow-up solutions known from the

original Keller-Segel model. This information is useful, for example, when using chemotactic models to describe active colloidal systems. Recently, a Keller-Segel-type model has been used to describe clustering in these systems [10]. As our analysis showed, including some form of damping in these models can help avoiding blow-up solutions and thus more realistically describe particle-based observations.

With this work we can include chemotactic clustering into the class of active phase separation. Other examples in this class include cell polarization [14, 22] and motility-induced phase separation (MIPS) [28]. The coefficients of the CH model for these systems are different than for the chemotactic system considered here. However, since the coefficients of the CH equation can be rescaled to unity by rescaling time, space and the field amplitudes, all these systems show the same universal behavior near onset active phase separation, including the typical coarsening behavior known from equilibrium phase separation [17].

Our presented perturbation approach from Ref. [14] and applied here is a systematic extension of pattern formation theory. It can be applied to further variants of models for chemotactic particles with particle conservation in order to reveal system-spanning properties for further models as well. It can also be extended to include higher order nonlinearities as demonstrated in Ref. [28] for MIPS. Analyzing the influence of these higher order nonlinearities in the context of cell clustering is an interesting future task.

ACKNOWLEDGMENTS

Support by the Elite Study Program Biological Physics is gratefully acknowledged.

-
- [1] M. Eisenbach. *Chemotaxis*. Imperial College Press, London, 2004.
 - [2] G. H. Wadhams and J. P. Armitage. Making Sense of it all: Bacterial Chemotaxis. *Nat. Rev. Mol. Cell Biol.*, 5:1024, 2004.
 - [3] H. C. Berg. *E. coli in Motion*. Springer, New York, 2004.
 - [4] E. T. Roussos, J. S. Condeelis, and A. Patsialou. chemotaxis in cancer. *Nat. Rev. Cancer*, 11:573, 2011.
 - [5] D. Dormann, B. Vasiev, and C. J. Weijer. The control of chemotactic cell movement during *dictyostelium* movement. *Phil. Trans. R. Soc. Lond. B*, 355:983, 2000.
 - [6] R. Soto and R. Golestanian. Self-assembly of active colloidal molecules with dynamic function. *Phys. Rev. E*, 91:052304, 2015.
 - [7] R. Niu, T. Palberg, and T. Speck. Self-Assembly of Colloidal Molecules due to Self-Generated Flow. *Phys. Rev. Lett.*, 119:028001, 2017.
 - [8] E. F. Keller and L. A. Segel. Initiation of slime mold aggregation viewed as an instability. *J. Theor. Biol.*, 26:399, 1970.
 - [9] E. F. Keller and L. A. Segel. Model for chemotaxis. *J. Theor. Biol.*, 30:225, 1971.
 - [10] B. Liebchen, D. Marenduzzo, I. Pagonabarraga, and M. E. Cates. Clustering and pattern formation in chemorepulsive active colloids. *Phys. Rev. Lett.*, 115:258301, 2015.
 - [11] M. J. Tindall, P. K. Maini, S. L. Porter, and J. P. Armitage. Overview of Mathematical Approaches Used to Model Bacterial Chemotaxis II: Bacterial Populations. *Bull. Math. Biol.*, 70:1570, 2008.
 - [12] T. Hillen and K. J. Painter. A user's guide to pde models for chemotaxis. *J. Math. Biol.*, 58:183, 2009.
 - [13] M. R. Myerscough, P. K. Maini, and K. J. Painter. Pattern formation in a generalized chemotaxis model. *Bull. Math. Biol.*, 60:1, 1998.
 - [14] F. Bergmann, L. Rapp, and W. Zimmermann. Active phase separation: A universal approach. *Phys. Rev. E*, 98:072001(R), 2018.
 - [15] M. C. Cross and P. C. Hohenberg. Pattern formation outside of equilibrium. *Rev. Mod. Phys.*, 65:851, 1993.

- [16] J. W. Cahn. On spinodal decomposition. *Acta Metallurgica*, 9:795, 1961.
- [17] A. J. Bray. Theory of phase-ordering kinetics. *Adv. Phys.*, 43:357, 1994.
- [18] M. Otsuji, S. Ishihara, C. Co, K. Kaibuchi, A. Mochizuki, and S. Kuroda. A mass conserved reaction-diffusion system captures properties of cell polarity. *PLoS Comp. Biol.*, 3:e108, 2007.
- [19] A. Jilkine, A. F. M. Marée, and L. Edelstein-Keshet. Mathematical Model for Spatial Segregation of the Rho-Family GTPases Based on Inhibitory Crosstalk. *Bull. Math. Biol.*, 69:1943, 2007.
- [20] Y. Mori, A. Jilkine, and L. Edelstein-Keshet. Wave-Pinning and Cell Polarity from a Bistable Reaction-Diffusion System. *Biophys. J.*, 94:3684, 2008.
- [21] P. K. Trong, E. M. Nicola, N. W. Goehring, K. V. Kumar, and S. W. Grill. Parameter-space topology of models for cell polarity. *New J. Phys.*, 16:065009, 2014.
- [22] F. Bergmann and W. Zimmermann. On system-spanning demixing properties of cell polarization. submitted, 2019.
- [23] J. Palacci, S. Sacanna, A. P. Steinberg, D. J. Pine, and P. M. Chaikin. Living crystals of light-activated colloidal surfers. *Science*, 339:936, 2013.
- [24] I. Buttinoni, J. Bialké, F. Kümmel, H. Löwen C. Bechinger, and T. Speck. Dynamical Clustering and Phase Separation in Suspensions of Self-Propelled Colloidal Particles. *Phys. Rev. Lett.*, 110:238301, 2013.
- [25] J. Stenhammer, A. Tiribocchi, R. J. Allen, D. Marenduzzo, and M. E. Cates. Continuum Theory of Phase Separation Kinetics for Active Brownian Particles. *Phys. Rev. Lett.*, 111:145702, 2013.
- [26] T. Speck, J. Bialké, A. M. Menzel, and H. Löwen. Cahn-Hilliard equation for the phase separation of active Brownian particles. *Phys. Rev. Lett.*, 112:218304, 2014.
- [27] T. Speck, A. M. Menzel, J. Bialke, and H. Löwen. Dynamical mean-field theory and weakly non-linear analysis for the phase separation of active Brownian particles. *J. Chem. Phys.*, 142:224109, 2015.
- [28] L. Rapp, F. Bergmann, and W. Zimmermann. Systematic extension of the Cahn-Hilliard model for motility-induced phase separation. arXiv:1901.03203, 2019.
- [29] M. C. Cross and H. Greenside. *Pattern Formation and Dynamics in Nonequilibrium Systems*. Cambridge Univ. Press, Cambridge, 2009.

Systematic extension of the Cahn-Hilliard model for motility-induced phase separation

Lisa Rapp, Fabian Bergmann and Walter Zimmermann

Eur. Phys. J. E **42**, 57 (2019)
(DOI: 10.1140/epje/i2019-11825-8)

Reprinted with permission from The European Physical Journal (EPJ)
©EDP Sciences / Società Italiana die Fisica / Springer-Verlag GmbH Germany 2019

Systematic extension of the Cahn-Hilliard model for motility-induced phase separation

Lisa Rapp, Fabian Bergmann, and Walter Zimmermann^a

Theoretische Physik I, Universität Bayreuth, 95440 Bayreuth, Germany

Received 10 January 2019 and Received in final form 9 April 2019

Published online: 16 May 2019

© EDP Sciences / Società Italiana di Fisica / Springer-Verlag GmbH Germany, part of Springer Nature, 2019

Abstract. We consider a continuum model for motility-induced phase separation (MIPS) of active Brownian particles (ABP) (J. Chem. Phys. **142**, 224149 (2015)). Using a recently introduced perturbative analysis (Phys. Rev. E **98**, 020604(R) (2018)), we show that this continuum model reduces to the classic Cahn-Hilliard (CH) model near the onset of MIPS. This makes MIPS another example of the so-called active phase separation. We further introduce a generalization of the perturbative analysis to the next higher order. This results in a generic higher-order extension of the CH model for active phase separation. Our analysis establishes the mathematical link between the basic mean-field ABP model on the one hand, and the leading order and extended CH models on the other hand. Comparing numerical simulations of the three models, we find that the leading-order CH model agrees nearly perfectly with the full continuum model near the onset of MIPS. We also give estimates of the control parameter beyond which the higher-order corrections become relevant and compare the extended CH model to recent phenomenological models.

1 Introduction

Active matter systems are non-equilibrium systems which consume fuel and dissipate energy locally. These systems are full of fascinating phenomena and have recently attracted increasing attention in the scientific community [1–8]. Examples range from active molecular processes which are driven by chemical free energy provided by metabolic processes [9] up to flocks of birds and schools of fish [1, 2]. Various active matter systems also show collective non-equilibrium transitions. On the time scale of these transitions, the number of involved entities such as proteins, cells or even birds is conserved. Examples include cell polarization [10–16], chemotactically communicating cells [17–20], self-propelled colloidal particles [21–27], as well as mussels in ecology [28].

Self-propelling colloidal particles undergo a non-equilibrium phase transition into two distinct phases—a denser liquid-like phase and a dilute gas-like phase [21–23]—if their swimming speed decreases with increasing local density. This is known as motility-induced phase separation (MIPS) [4, 24, 26]. It strikingly resembles well-known phase separation processes at thermal equilibrium such as the demixing of a binary fluid. We recently introduced a class of such non-equilibrium demixing phe-

nomena we call active phase separation [16]. Among the phenomena identified as members of this class are cell polarization or chemotactically communicating cells. For this class we have shown that the similarities between equilibrium and non-equilibrium demixing phenomena are in fact not coincidental. We have generalized a classical weakly nonlinear analysis near a supercritical bifurcation with unconserved order parameter fields [29] to the case of active phase separation with a conserved order parameter field [16]. The generic equation describing active phase separation systems turned out to be the classic Cahn-Hilliard (CH) model—the same generic model that also describes equilibrium phase separation. The class of active phase separation thus defines non-equilibrium demixing phenomena whose conserved order parameter is close to onset described by the Cahn-Hilliard model.

In this work, we raise the question whether the recently introduced nonlinear perturbation approach in ref. [16] is also directly applicable to MIPS. We employ this reduction approach to a mean-field description of active Brownian particles (ABP) showing MIPS provided by Speck *et al.* [27, 30] and show how the ABP model reduces to the CH model at leading order.

Recently, several phenomenological extensions of the CH model have also been considered as continuum models of MIPS [31, 32]. These are extensions of the CH model to the next higher order of nonlinear contributions. In this

^a e-mail: walter.zimmermann@uni-bayreuth.de

work, we therefore also introduce an extension of our perturbative scheme that allows us to systematically derive higher-order nonlinearities directly from the continuum model for MIPS. Due to our systematic approach, the extended CH model we derive is not a phenomenological model. Instead, we directly map the continuum model for ABP to the extended CH model. Note that we concentrate on the example of MIPS in this work. However, the extension introduced here can be applied to any system in the class of active phase separation. We thus show in general how both the leading-order CH model and its extension describe active phase separation as a non-equilibrium phenomenon.

This work is organized as follows: We first present the mean-field ABP model and calculate the onset of phase separation in the system. We then introduce the perturbative scheme we use to reduce the ABP model to the classic CH equation near the onset of phase separation. In the next step, we extend the previous approach to include nonlinearities at the next higher order. Section 5 is an in-depth discussion of the derived leading-order and extended CH models including their connection to the mean-field ABP model and other phenomenological descriptions of MIPS. Finally, in sect. 6, we present numerical simulations comparing leading-order and extended CH to the full mean-field ABP model to assess validity and accuracy of the reduced models.

2 Model

On a mean-field level, phase separation of active Brownian particles (ABP) can be described by two coupled equations for the particle density $\tilde{\rho}(\mathbf{r}, t)$ and a polarization $\mathbf{p}(\mathbf{r}, t)$ [23, 30]. The evolution of the particle density $\tilde{\rho}$ is determined by

$$\partial_t \tilde{\rho} = -\nabla \cdot [v(\tilde{\rho})\mathbf{p} - D_e \nabla \tilde{\rho}], \quad (1)$$

where D_e is the effective diffusion coefficient of the active Brownian particles. $v(\tilde{\rho})$ is the density-dependent particle speed given by

$$v(\tilde{\rho}) = v_0 - \tilde{\rho}\zeta + \lambda^2 \nabla^2 \tilde{\rho}; \quad (2)$$

v_0 is the speed of a single self-propelled particle. With increasing particle density, the velocity is reduced by $\zeta\tilde{\rho}$ due to interactions with other particles. ζ is related to the pair distribution function of the individual particles and assumed to be spatially homogeneous [23]. The nonlocal contribution in eq. (2) was earlier introduced in refs. [25, 33] and later incorporated into the model by Speck *et al.* [30]. It incorporates the effect that active Brownian particles sample the neighboring particle density on a length scale λ larger than the particle spacing. Equation (2) is coupled to a dynamical equation for the polarization [23, 30],

$$\partial_t \mathbf{p} = -\nabla P(\tilde{\rho}) + D_e \nabla^2 \mathbf{p} - \mathbf{p}, \quad (3)$$

with the ‘‘pressure’’

$$P(\tilde{\rho}) = \frac{1}{2}v(\tilde{\rho})\tilde{\rho}. \quad (4)$$

3 Onset of phase separation

A stationary solution of eq. (1) and eq. (3) is any constant density $\bar{\rho}$ and $\mathbf{p} = 0$. Therefore, we decompose the particle density into its homogeneous part $\bar{\rho}$ and the inhomogeneous density variation ρ :

$$\tilde{\rho} = \bar{\rho} + \rho. \quad (5)$$

Accordingly, we investigate the following dynamical equations for ρ and p in one spatial dimension:

$$\partial_t \rho = -\partial_x [\alpha - \zeta\rho + \lambda^2 \partial_x^2 \rho] p + D_e \partial_x^2 \rho, \quad (6a)$$

$$\begin{aligned} \partial_t p = & -\partial_x \left[\beta\rho - \frac{1}{2}\zeta\rho^2 + \frac{\lambda^2}{2}(\bar{\rho} + \rho)\partial_x^2 \rho \right] \\ & + D_e \partial_x^2 p - p, \end{aligned} \quad (6b)$$

where

$$\alpha = v_0 - R, \quad \beta = \frac{1}{2}(v_0 - 2R), \quad (7)$$

with the density parameter

$$R = \zeta\bar{\rho}. \quad (8)$$

We assume ζ and D_e to be constant [30].

The homogeneous basic solution $\rho = 0, p = 0$ is unstable if the perturbations $\rho, p = \hat{\rho}, \hat{p} \exp(\sigma t + iqx)$ grow, *i.e.* if the growth rate σ is positive. Solving the linear parts of eqs. (6) with this perturbation ansatz, the largest eigenvalue gives us the dispersion relation

$$\begin{aligned} \sigma(q) = & -\frac{1}{2} - D_e q^2 + \frac{1}{2}\sqrt{1 - 4\alpha\beta q^2 + 2\lambda^2\alpha\bar{\rho}q^4}, \\ = & D_2 q^2 - D_4 q^4 + \mathcal{O}(q^6), \end{aligned} \quad (9)$$

where

$$D_2 = -(D_e + \alpha\beta), \quad (10)$$

$$D_4 = \left(\alpha^2 \beta^2 - \frac{\lambda^2 R}{2} \alpha \right). \quad (11)$$

D_2 changes its sign as a function of v_0 . Assuming $D_4 > 0$, the growth rate σ becomes positive in a finite range of $q = [0, q_{max}]$, when $D_2 > 0$. Note that the range of wavenumbers q with positive growth rate extends down to $q = 0$. The related instability condition

$$D_e + \alpha\beta = 0 \quad (12)$$

provides a quadratic polynomial for the critical mean density $\bar{\rho}$ (represented by the density parameter R) and the respective particle speed $v_0(R)$:

$$\frac{1}{2}v_0^2 - \frac{3}{2}Rv_0 + D_e + R^2 = 0. \quad (13)$$

For particle speeds $v_0 > v_*$, where

$$v_* = 4\sqrt{D_e}, \quad (14)$$

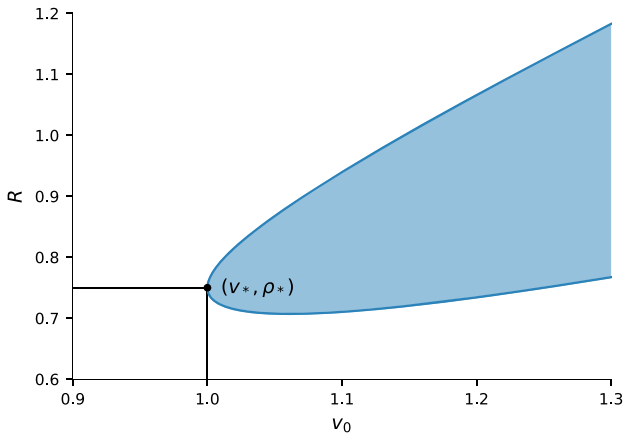


Fig. 1. Instability curve $R_{\pm}(v_0)$ as given by eq. (15). The minimum of the parabolic function is at $(v_*, R_*) = (1.0, 0.75)$, assuming $\zeta = 1$, $D_e = 1/16$. For $v_0 > v_*$, the homogeneous solution is unstable for mean densities within the shaded region.

this polynomial has two real solutions

$$R_{\pm} = \frac{1}{4} \left[3v_0 \pm \sqrt{v_0^2 - 16D_e} \right]. \quad (15)$$

This corresponds to a critical value R_* of the density parameter:

$$R_* = R(v_*) = \frac{3}{4}v_*. \quad (16)$$

Note that the assumption $D_4 > 0$ is fulfilled if $\lambda^2 < 2\zeta\alpha\beta^2/R$, *i.e.* for sufficiently small λ . At the critical point, $v_0 = v_*$ and $R = R_*$, this condition simplifies to

$$\lambda^2 < \zeta v_*^2/24. \quad (17)$$

For particle velocities below v_* , the homogeneous solution is stable for any value of the density parameter $R = \zeta\bar{\rho}$. For $v > v_*$ and $R_- < R < R_+$ (shaded region in fig. 1) the homogeneous particle density becomes unstable with respect to perturbations.

4 Derivation of Cahn-Hilliard models

In this section, we will apply the systematic perturbative scheme introduced recently in ref. [16] to the mean-field model, eqs. (6), and reduce them near onset to the well-known Cahn-Hilliard (CH) model. In a second step, we will then expand the perturbative scheme to include higher-order contributions.

The transition from the homogenous state of eqs. (1) and (3) to MIPS is either supercritical or slightly subcritical. In both cases, cubic nonlinearities limit the growth of density modulations —as we also confirm in this work *a posteriori*. Therefore, the amplitudes of the density modulations near MIPS are small and we write

$$\rho = \sqrt{\varepsilon}\rho_1 \quad (18)$$

with a small parameter ε and $\rho_1 \sim O(1)$. Thereby ε measures the distance from the critical velocity v_* :

$$v_0 = v_*(1 + \varepsilon). \quad (19)$$

This also allows an expansion of $R_{\pm}(v_0)$ in eq. (15) near R_* . At leading order, we find $R_{\pm} \simeq R_*(1 \pm \eta\sqrt{\varepsilon})$ with $\eta = \sqrt{2}/3$. This suggests the following parameterization of R in the ranges $v_0 > v_*$ and $R_- < R < R_+$ near R_* :

$$R = R_*(1 + r_1), \quad \text{with } r_1 = \sqrt{\varepsilon}\tilde{r}_1. \quad (20)$$

According to the dispersion relation in eq. (9), the fastest growing mode is given by $q_e^2 = D_2/(2D_4)$. The largest growing wavenumber q_{max} (calculated from $\sigma = 0$) is $q_{max}^2 = D_2/D_4$. Thus, both q_e^2 and q_{max}^2 scale with the factor D_2/D_4 . Using the previously introduced definitions and expanding for small values of the control parameter ε , we find $D_2/D_4 \propto \varepsilon$ at leading order. Thus, both q_e and q_{max} are of the order $\sqrt{\varepsilon}$, *i.e.* perturbations of the homogeneous basic state vary on a large length scale. Accordingly, we introduce the new scaling $\tilde{x} = \sqrt{\varepsilon}x$, resulting in the following replacement of the differential operator:

$$\partial_x \rightarrow \sqrt{\varepsilon}\tilde{\partial}_x. \quad (21)$$

From q^2 of order $O(\varepsilon)$ and $D_2 \propto \varepsilon$ follows that $\sigma \propto \varepsilon^2$ according to eq. (9). Thus, the growth of these long wavelength perturbations is very slow. Accordingly, we introduce the slow time scale $T_1 = \varepsilon^2 t$. In order to capture the dynamics at the next higher order of $\varepsilon^{1/2}$, we also introduce a second slow time scale $T_2 = \varepsilon^{5/2} t$. This suggests the following replacement of the time derivatives:

$$\partial_t \rightarrow \varepsilon^2 \partial_{T_1} + \varepsilon^{5/2} \partial_{T_2}. \quad (22)$$

Since we expressed the density ρ as a multiple of $\sqrt{\varepsilon}$, see eq. (18), we also expand the polarization field p in orders of $\sqrt{\varepsilon}$:

$$p = \sqrt{\varepsilon}p_0 + \varepsilon p_1 + \varepsilon^{3/2}p_2 + \varepsilon^2 p_3 + \varepsilon^{5/2}p_4 + \dots \quad (23)$$

We insert these scalings into the dynamic equations (6) and collect terms of the same order $\sqrt{\varepsilon}^n$. The polarization follows the density field adiabatically. Thus, the contributions to the polarization in increasing orders up to $\varepsilon^{5/2}$ are

$$p_0 = 0, \quad (24)$$

$$p_1 = -\beta_* \tilde{\partial}_x \rho_1, \quad (25)$$

$$p_2 = R_* \tilde{r}_1 \tilde{\partial}_x \rho_1 + \frac{\zeta}{2} \tilde{\partial}_x (\rho_1^2), \quad (26)$$

$$p_3 = -\frac{v_*}{2} \tilde{\partial}_x \rho_1 - \left(D_e \beta_* + \frac{\lambda^2 R_*}{2\zeta} \right) \tilde{\partial}_x^3 \rho_1, \quad (27)$$

$$p_4 = D_e \tilde{\partial}_x^3 \left(\tilde{r}_1 R_* \rho_1 + \frac{\zeta}{2} \rho_1^2 \right) - \frac{\lambda^2}{2} \tilde{\partial}_x (\tilde{r}_1 \rho_* + \rho_1) \tilde{\partial}_x^2 \rho_1. \quad (28)$$

With these solutions, we can systematically solve the equations for the density ρ_1 in the successive orders of $\sqrt{\varepsilon}$. In the lowest order $\mathcal{O}(\varepsilon^{3/2})$, we find

$$0 = (\alpha_*\beta_* + D_e)\tilde{\partial}_x^2\rho_1. \quad (29)$$

This equation, however, is trivially satisfied due to the instability condition $\alpha_*\beta_* + D_e = 0$.

At order $\mathcal{O}(\varepsilon^2)$, we get

$$0 = -(\alpha_* + \beta_*) \left[R_*\tilde{r}_1\tilde{\partial}_x^2\rho_1 + \zeta\tilde{\partial}_x \left(\rho_1\tilde{\partial}_x\rho_1 \right) \right]. \quad (30)$$

With the definition of R_* in eq. (16) it follows that $\alpha_* + \beta_* = 0$. Thus, eq. (30) is again trivially fulfilled.

At order $\mathcal{O}(\varepsilon^{5/2})$, we finally get a dynamic equation for ρ_1 :

$$\begin{aligned} \partial_{T_1}\rho_1 = & -\tilde{\partial}_x^2 \left[\left(\frac{1}{8}v_*^2 - \frac{9}{16}v_*^2\tilde{r}_1^2 \right) \rho_1 \right. \\ & + \left(\frac{1}{256}v_*^4 - \frac{3}{32\zeta}\lambda^2v_*^2 \right) \tilde{\partial}_x^2\rho_1 \\ & \left. - \frac{3}{4}\zeta v_*\tilde{r}_1\rho_1^2 - \frac{1}{3}\zeta^2\rho_1^3 \right]. \end{aligned} \quad (31)$$

Note that we used the expressions in eq. (14) and eq. (16) to eliminate R_* and D_e . Equation (31) has the form of the well-known Cahn-Hilliard (CH) equation [34, 35]. This shows that MIPS is a further example of the non-equilibrium demixing phenomenon which shares the universal CH model with classic phase separation. Recently, the notion *active phase separation* was coined for these types of non-equilibrium phenomena [16]. Other recently discussed examples of active phase separation are cell polarization or chemotactically communicating cell colonies [16]. All of these very different systems can be reduced to the same universal equation near the onset of phase separation. They thus share generic features as expressed in their common representation via the CH equation.

In the next step, we extend the reduction scheme introduced in ref. [16] to include higher-order nonlinearities. Continuing the expansion above to the next order $\mathcal{O}(\varepsilon^3)$, we obtain:

$$\begin{aligned} \partial_{T_2}\rho_1 = & -\tilde{\partial}_x^2 \left[\frac{9}{8}v_*^2\tilde{r}_1\rho_1 + \frac{3}{16\zeta}\lambda^2v_*^2\tilde{r}_1 \left(\tilde{\partial}_x^2\rho_1 \right) + \frac{3}{4}\zeta v_*\rho_1^2 \right. \\ & + \left(\frac{3}{128}\zeta v_*^3 - \frac{5}{16}\lambda^2v_* \right) \left(\tilde{\partial}_x\rho_1 \right)^2 \\ & \left. + \frac{\lambda^2}{8}v_*\tilde{\partial}_x^2\rho_1^2 \right]. \end{aligned} \quad (32)$$

We will discuss these new contributions in detail in sect. 5.2 below.

Equations (31) and (32) can be combined into a single equation by reconstituting the original time scale via $\partial_{t\rho_1} = \varepsilon^2\partial_{T_1}\rho_1 + \varepsilon^{5/2}\partial_{T_2}\rho_1$. In addition, we go back to the original spatial scaling by setting $\tilde{\partial}_x = \partial_x/\sqrt{\varepsilon}$, to the original density ρ via eq. (18), and r_1 as defined in eq. (20).

The complete extended amplitude equation for the density variations ρ then reads:

$$\begin{aligned} \partial_t\rho = & -\partial_x^2 \left[(\alpha_1 + \beta_1)\rho + (\alpha_2 + \beta_2)\partial_x^2\rho \right. \\ & + (\alpha_3 + \beta_3)\rho^2 - \alpha_4\rho^3 \\ & \left. + \beta_5(\partial_x\rho)^2 + \beta_6\partial_x^2\rho^2 \right]. \end{aligned} \quad (33)$$

In this equation, contributions with the coefficients α_i originate from the leading order and are given by

$$\alpha_1 = \frac{1}{8}v_*^2\varepsilon - \frac{9}{16}v_*^2r_1^2, \quad (34a)$$

$$\alpha_2 = \frac{1}{256}v_*^4 - \frac{3}{32\zeta}\lambda^2v_*^2, \quad (34b)$$

$$\alpha_3 = -\frac{3}{4}\zeta v_*r_1, \quad (34c)$$

$$\alpha_4 = \frac{1}{3}\zeta^2. \quad (34d)$$

In other words, eq. (33) with $\beta_i = 0$ is the rescaled version of eq. (31). The coefficients β_i signal the new contributions from the next higher order. They are given by

$$\beta_1 = \frac{9}{8}v_*^2r_1\varepsilon, \quad (35a)$$

$$\beta_2 = \frac{3}{16\zeta}\lambda^2v_*^2r_1, \quad (35b)$$

$$\beta_3 = \frac{3}{4}\zeta v_*\varepsilon, \quad (35c)$$

$$\beta_5 = \frac{3}{128}\zeta v_*^3 - \frac{5}{16}\lambda^2v_*, \quad (35d)$$

$$\beta_6 = \frac{\lambda^2}{8}v_*. \quad (35e)$$

5 Discussion of the derived Cahn-Hilliard models

In this section, we will discuss the results obtained in the previous sect. 4. At first we consider the classic CH equation that resulted at leading order of our perturbative analysis. We then take a closer look at the higher-order corrections $\propto \beta_i$ in eq. (33). We also focus on the relation of the higher-order coefficients β_i to the parameters of recently introduced phenomenological extensions of the CH model for MIPS [31, 32, 36].

5.1 Classic CH equation at leading order

For $\beta_i = 0$, the leading order of eq. (33),

$$\partial_t\rho = -\partial_x^2 \left[\alpha_1\rho + \alpha_2\partial_x^2\rho + \alpha_3\rho^2 - \alpha_4\rho^3 \right], \quad (36)$$

corresponds to the asymmetric version of the Cahn-Hilliard (CH) equation, see *e.g.* refs. [34, 35]. The coefficients α_i are given in eqs. (34). Note that the quadratic

nonlinearity implies a broken $\pm\rho$ -symmetry. This is usually not included in the classic representation of the CH equation since it can be removed by adding a constant to the density: $\rho \rightarrow \rho + \rho_h$. In any case, the quadratic nonlinearity vanishes for $\alpha_3 = 0$. For the ABP model, this is fulfilled for $r_1 = 0$, or $\bar{\rho} = \rho_*$ accordingly. This special case has also been considered in [30] where they found a CH equation with coefficients consistent with α_i above.

Equation (36) can be derived from the energy functional

$$F = \int \left[-\frac{\alpha_1}{2} + \frac{\alpha_2}{2}(\partial_x \rho)^2 - \frac{\alpha_3}{3}\rho^3 + \frac{\alpha_4}{4}\rho^4 \right] dx \quad (37)$$

via

$$\partial_t \rho = \partial_x^2 \frac{\delta F}{\delta \rho}. \quad (38)$$

At first glance this is a surprising result since the two initial dynamical equations for the density, eq. (1), and the polarization, eq. (3), do not follow potential dynamics and therefore cannot be derived from a functional. Nevertheless, this specific property has been seen for other non-equilibrium systems: The evolution equation for the envelope of spatially periodic patterns also follows potential dynamics while the dissipative starting equations do not [29, 37].

5.2 Extended CH model

We now take a closer look at the CH model extended to the next higher order, eq. (33) with coefficients β_i given in eqs. (35). The contributions β_1 , β_2 and β_3 are corrections to the coefficients α_1 , α_2 and α_3 of the leading-order CH equation. Note, however, that according to eqs. (35a) and (35c), β_1 and β_3 are functions of ε and thus both increase with the distance ε from phase separation onset. Notably, β_3 —the correction to the quadratic nonlinearity—is not a function of the relative deviation r_1 from the critical density parameter R_* . Thus, while for $r_1 = 0$ the CH model at leading order is $\pm\rho$ -symmetric, the symmetry is always broken at higher order.

The coefficients β_5 and β_6 are the prefactors of higher-order nonlinearities. These new contributions $\propto \partial_x^2(\partial_x \rho)^2$ and $\propto \partial_x^4 \rho^2$ are structurally different compared to the terms in the leading-order CH model. In general, an additional nonlinearity $\propto \partial_x^2 \rho^4$ is of the same order as these two contributions. However, in the exemplary case of ABP we analyze here this term does not appear. Note, however, that the higher-order extension of the CH model presented here can also be applied to other active phase separation systems. We expect the additional nonlinearity of the form $\propto \partial_x^2 \rho^4$ to be relevant in other examples such as cell polarization or chemotaxis.

In the context of MIPS, a contribution $\propto \partial_x^2(\partial_x \rho)^2$ has been introduced via a phenomenological approach in ref. [31]. The CH model extended by this term has been called *Active Model B*. It was considered as a non-equilibrium extension of the CH model and minimal model for MIPS. We would like to reiterate that the CH model as

given by eq. (36) (without any additional nonlinear terms) is the leading-order description of the *non-equilibrium* phenomenon of active phase separation [16]. As we have shown here, this also includes MIPS. All higher-order nonlinearities vanish for $\varepsilon \rightarrow 0$ (see also the discussion in sect. 5.4). In that respect *Active Model B* is a nonlinear extension of the CH model—not an extension of the CH model to non-equilibrium systems. Our systematic approach reveals the existence of the additional higher nonlinearity $\propto \partial_x^4 \rho^2 = 2\partial_x^2[(\partial_x \rho)^2 + \rho \partial_x^2 \rho]$. It includes the nonlinear correction to the CH model, $\propto \partial_x^2(\partial_x \rho)^2$, that leads to the *Active Model B* [4, 31]. The second part of the new nonlinear correction term, $\propto \partial_x^2(\rho \partial_x^2 \rho)$, has recently been included in a further CH extension for MIPS called *Active Model B+* [32, 36]. Note that the contribution $\propto \beta_6$ in eq. (33) vanishes for $\lambda = 0$. *Active Model B* and *Active Model B+* also do not include the quadratic nonlinearity $\propto \beta_3 \rho^2$. Our analysis shows, however, that the coefficients β_i in general are not independent of each other and β_2 in fact always appears simultaneously with the nonlinearity $\propto \beta_5$. The broken \pm -symmetry and the resulting asymmetric phase separation profiles depend on the distance ε from threshold (see β_3 in eq. (35c)). It is an important qualitative feature of the system behavior above threshold.

As discussed in sect. 5.1, the leading-order CH model can be derived from an energy potential. For the extended CH model, eq. (33), the existence of an energy functional depends on the coefficients of the additional higher-order contributions: for arbitrary values of β_5 and β_6 , the extended CH model is non-potential. In the special case $\beta_6 = -\beta_5$, however, eq. (33) can be derived from the energy functional

$$F = \int \left[\frac{-\alpha_1 + \beta_1}{2} \rho^2 + \frac{\alpha_2 + \beta_2}{2} (\partial_x \rho)^2 - \frac{\alpha_3 + \beta_3}{3} \rho^3 - \frac{\alpha_4}{4} \rho^4 + \frac{\beta_5}{2} \rho^2 \partial_x^2 \rho \right] dx. \quad (39)$$

For the ABP model, eqs. (6), this condition is fulfilled for

$$\lambda^2 = \frac{\zeta v_*^2}{8}. \quad (40)$$

Note, however, that the linear stability analysis in sect. 3 introduced a condition for λ : $\lambda^2 < \zeta v_*^2/24$ in eq. (17). This condition and eq. (40) cannot be fulfilled simultaneously. Thus, whether the extended CH model can be derived from an energy functional depends on the exact parameter choices. For the ABP continuum model we investigate here, there do not seem to be suitable parameter choices. But note again that our approach can be applied to other systems showing active phase separation. For these other models, the coefficients of the extended CH model could allow for the existence of a suitable potential.

5.3 Comparison of linear stability

As a first step to assess the quality of our derived reduced equation, eq. (33), we analyze the linear stability of the

homogeneous basic state $\rho = 0$, and compare to the stability of the full ABP model. As discussed in sect. 3, the instability condition for the full ABP system is given by eq. (12). Using $v_0 = v_*(1 + \varepsilon)$, $R = R_*(1 + r_1)$ and the definitions of D_e and R_* as given by eqs. (14) and (16), we find

$$\begin{aligned} \varepsilon_c &= \frac{1}{8} (1 + 9r_1) - \frac{1}{8} \sqrt{1 + 18r_1 + 9r_1^2} \\ &\approx \frac{9}{2} r_1^2 - \frac{81}{2} r_1^3 + \frac{891}{2} r_1^4 + \mathcal{O}(r_1^5) \end{aligned} \quad (41)$$

for the onset of phase separation. Thus, in the symmetric case $r_1 = 0$ the threshold is $\varepsilon_c = 0$. For $r_1 \neq 0$ the onset of phase separation is shifted to larger values of ε . Larger particle velocities v_0 are thus required to trigger the demixing process.

Similarly, we can analyze the linear stability of both the leading-order CH equation, eq. (36), and its higher-order extension, eq. (33). The threshold calculated from the linear parts of eq. (36) is given by

$$\varepsilon_{c,\text{lead}} = \frac{9}{2} r_1^2. \quad (42)$$

Comparing this to ε_c in eq. (41), we find that the shifting of the threshold due to finite r_1 is represented up to leading order of r_1 . Assuming $r_1 > 0$, $\varepsilon_{c,\text{lead}}$ significantly overestimates the real threshold ε_c . For the extended CH equation, eq. (33), we find the threshold

$$\begin{aligned} \varepsilon_{c,\text{ext}} &= \frac{9r_1^2}{2(1 + 9r_1^2)} \\ &\approx \frac{9}{2} r_1^2 - \frac{81}{2} r_1^3 + \frac{729}{2} r_1^4 + \mathcal{O}(r_1^5). \end{aligned} \quad (43)$$

This is in agreement with the threshold for the full model, eq. (41), up to the order $\mathcal{O}(r_1^3)$. The threshold is therefore only slightly underestimated compared to the full model. Keeping these different threshold values in mind is particularly important for the numerical comparison of the ABP model, eqs. (1) and (3), to its two reductions, eqs. (36) and (33) in sect. 6. All three equations only provide the exact same threshold, namely $\varepsilon_c = 0$, in the special case $r_1 = 0$.

The linear stability analysis also provides the dispersion relation for the perturbation growth rate σ . For the full model, it is given by eq. (9). Expanding for small perturbation wavenumbers q , the general form of the growth rate is

$$\sigma = D_2 q^2 - D_4 q^4 + \mathcal{O}(q^6). \quad (44)$$

The coefficients D_2 and D_4 are given in eqs. (10) and (11), respectively. Using the definitions introduced in the course of the perturbative expansion, D_2 can be rewritten to

$$D_2 = \frac{1}{8} v_*^2 \varepsilon - \frac{9}{16} v_*^2 r_1^2 + \frac{9}{8} v_*^2 r_1 \varepsilon - \frac{1}{2} v_*^2 \varepsilon^2. \quad (45)$$

Good agreement between the full ABP model and its reduction to eq. (33) can only be expected if the reduced equations are able to reproduce the basic form of this

growth rate. The linear part of eq. (33) leads to a growth rate of the form

$$\sigma(q) = G_2 q^2 - G_4 q^4, \quad (46)$$

where

$$G_2 = \frac{1}{8} v_*^2 \varepsilon - \frac{9}{16} v_*^2 r_1^2 + \frac{9}{8} v_*^2 r_1 \varepsilon, \quad (47)$$

$$G_4 = \frac{1}{256} v_*^4 - \frac{3}{32\zeta} \lambda^2 v_*^2 + \frac{3}{16\zeta} \lambda^2 v_*^2 r_1. \quad (48)$$

G_2 is in agreement with D_2 of the full model equations up to linear order in ε . D_2 only includes an additional term of order $\mathcal{O}(\varepsilon^2)$: $D_2 = G_2 - v_*^2 \varepsilon^2 / 2$. G_4 exactly reduces to D_4 in the case $\varepsilon = r_1 = 0$. In the limit $\varepsilon \rightarrow 0$ but $r_1 \neq 0$, the two terms agree up to linear order in r_1 . As discussed in sect. 3, the coefficient D_4 has to be positive for the instability condition to hold and to ensure damping of short wavelength perturbations. The same applies to the coefficient G_4 . The condition $G_4 > 0$ is fulfilled if

$$\lambda^2 < \frac{1}{24} v_*^2 \zeta \frac{1}{1 - 2r_1}. \quad (49)$$

Note the similarity to the previously derived condition in eq. (17).

5.4 Significance of nonlinear corrections

In this section, we discuss the importance of the higher-order nonlinearities compared to the leading-order terms of the classic Cahn-Hilliard model in eq. (36). For this comparison we focus on the case with \pm -symmetry at leading order, *i.e.* $r_1 = 0$. We rescale time, space and amplitude in eq. (33) via $t' = \tau_0 \varepsilon^2 t$, $x' = \xi_0 \sqrt{\varepsilon} x$ and $\rho' = \rho_0 \rho / \sqrt{\varepsilon}$, respectively, where

$$\tau_0 = \frac{4\zeta v_*^2}{v_*^2 \zeta - 24\lambda^2}, \quad (50a)$$

$$\xi_0^2 = \frac{32\zeta}{v_*^2 \zeta - 24\lambda^2}, \quad (50b)$$

$$\rho_0 = \frac{2\sqrt{6}}{3} \frac{\zeta}{v_*}. \quad (50c)$$

This allows us to rewrite eq. (33) in the following form:

$$\begin{aligned} \partial_{t'} \rho' &= -\partial_{x'}^2 [\rho' + \partial_{x'}^2 \rho' - \rho'^3] \\ &\quad - \sqrt{\varepsilon} \partial_{x'}^2 [\gamma_1 \rho'^2 + \gamma_2 \partial_{x'}^2 \rho'^2 + \gamma_3 (\partial_{x'} \rho')^2], \end{aligned} \quad (51)$$

where

$$\gamma_1 = \frac{3\sqrt{6}}{2}, \quad (52a)$$

$$\gamma_2 = \frac{8\sqrt{6}\lambda^2}{v_*^2 \zeta - 24\lambda^2}, \quad (52b)$$

$$\gamma_3 = \frac{\sqrt{6}(3v_*^2 \zeta - 40\lambda^2)}{2(v_*^2 \zeta - 24\lambda^2)}. \quad (52c)$$

The first line in eq. (51) is the parameter-free, $\pm\rho$ -symmetric version of the Cahn-Hilliard model as described, *e.g.*, in refs. [34, 35]. The additional three contributions are the first higher-order corrections as gained above via a systematic reduction of the continuum model for MIPS. These three corrections are proportional to $\sqrt{\varepsilon}$ and thus vanish when approaching the onset of active phase separation ($\varepsilon \rightarrow 0$). In the limit $\varepsilon \rightarrow 0$ the classic CH model thus fully describes the non-equilibrium mean-field dynamics of MIPS. With increasing ε , the higher-order contributions become more and more important.

Note that eq. (51) was derived under the assumption $r_1 = 0$. As discussed in sect. 5.1, the CH model at leading order is $\pm\rho$ -symmetric in this case. The three higher-order contributions in eq. (51), however, break the $\pm\rho$ -symmetry with increasing ε . Moreover, in the case of the ABP model we analyze here, the coefficient γ_1 does not depend on any of the system parameters at all. Thus, there is in fact no special case in which this contribution can be neglected.

The coefficients of the other two higher-order nonlinearities, γ_2 and γ_3 , are functions of the system parameters, especially of λ . Typical parameter choices for the continuum model in eq. (6) are such that v_* and ζ are of order $\mathcal{O}(1)$. Accordingly, λ has to be small to fulfill the condition in eq. (17). Therefore, an expansion of γ_2 and γ_3 in terms of small λ is appropriate:

$$\gamma_2 = \frac{8\sqrt{6}}{v_*^2\zeta}\lambda^2 + \mathcal{O}(\lambda^4), \quad (53)$$

$$\gamma_3 = \gamma_1 + 2\gamma_2 + \mathcal{O}(\lambda^4). \quad (54)$$

In the limit $\lambda = 0$ the coefficient γ_2 vanishes, *i.e.* $\gamma_2 = 0$, and γ_3 simplifies to $\gamma_3 = \gamma_1$. For finite λ , γ_2 also becomes finite. But since according to eq. (53) γ_2 is proportional to λ^2 , it will be much smaller than γ_3 for small λ . For MIPS as described by the mean-field model in eqs. (6), the impact of the nonlinearity $\propto \partial_x^2(\partial_x\rho)^2$ thus seems to overshadow the term $\propto \partial_x^4\rho^2$. This predominance of γ_3 , however, is specific to MIPS as described by the ABP model. For other examples of active phase separation such as cell polarization or chemotactically communicating cells, we expect that the nonlinearities described by γ_1 or γ_2 can be of similar order as γ_3 . As mentioned earlier, for both examples of active phase separation we also expect an additional higher-order correction $\propto \partial_x^2\rho^4$ which is completely absent in the ABP model.

6 Numerical comparison

In this section, we compare numerical simulations of the full ABP model, eqs. (6), to both the leading-order CH equation, eq. (36), as well as the extended version including higher nonlinearities, eq. (33). On the one hand, this allows us to assess the quality and validity range of our reduction scheme in general. On the other hand, comparing the leading-order and the extended CH model also gives us information about the importance of higher-order nonlinearities in MIPS.

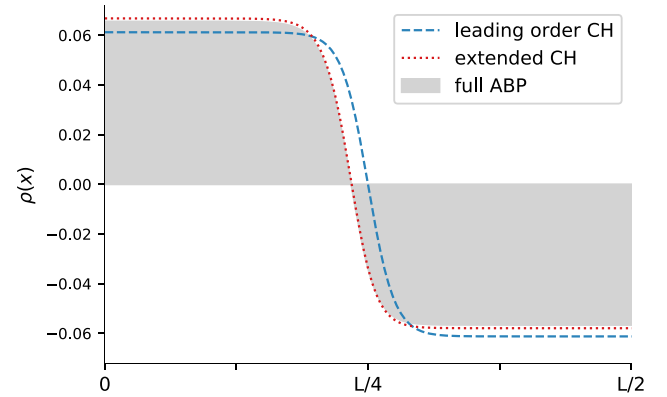


Fig. 2. Comparison of the steady-state profiles in the “symmetric” case ($\bar{\rho} = \rho_*$) at $\varepsilon = 0.01$: full ABP model (shaded grey) *vs.* leading-order CH equation (dashed line) *vs.* extended CH equation (dotted line). Other parameters: $\zeta = v_* = 1$.

All simulations were performed using a spectral method with a semi-implicit Euler time step. The system size was $L = 100$ with periodic boundary conditions and $N = 256$ Fourier modes were used.

We first analyze the special case $r_1 = 0$, *i.e.* $\bar{\rho} = \rho_*$. This is the case in which the \pm -symmetry-breaking quadratic nonlinearity vanishes at leading order. We choose $v_* = 1$ and $\zeta = 1$ throughout all of the following simulation results. As discussed in sect. 5.4, λ has to be small and is thus not expected to significantly influence the results. We thus set $\lambda = 0$.

Figure 2 shows the steady-state profiles for the three models (full ABP model, leading-order CH and extended CH) at $\varepsilon = 0.01$. The profiles are typical for phase separation solutions: We find two distinct regions where the mean density is either increased ($\rho > 0$) or decreased ($\rho < 0$). In each of the regions ρ is essentially spatially constant, creating two distinct density plateaus ρ_{\min} and ρ_{\max} . The two plateaus are smoothly connected at their boundary, resembling a hyperbolic tangent function. Note that the mean density in the system is conserved. Thus, the areas under the positive and negative parts of $\rho(x)$ are equal.

The solution for the full system is represented as the outline of the grey shaded area. We first compare this to the leading-order CH equation (dashed line). As predicted, the leading-order CH equation results in a symmetric phase separation profile, *i.e.* the two plateaus have the same absolute value: $\rho_{\max} = |\rho_{\min}|$. This does not accurately represent the solution for the full system, which is already slightly asymmetric. However, the leading-order CH equation gives a good approximation of the plateau values with a deviation of less than 7% from the real value. Extending the CH equation to the next higher order (dotted line in fig. 2), we can almost perfectly reproduce the profile for the full ABP model. It accurately represents the asymmetry of the phase separation profile. The deviation in the plateau values shrinks to less than 2%.

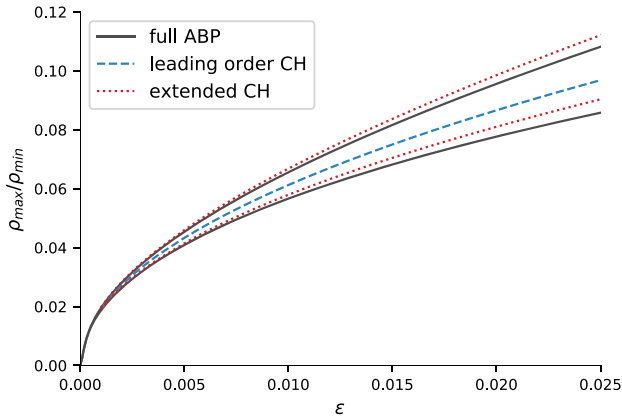


Fig. 3. Comparison of plateau values $|\rho_{\min}|$ and ρ_{\max} as a function of the control parameter ε for $\bar{\rho} = \rho_*$ (*i.e.*, $r_1 = 0$): full ABP model (solid line) *vs.* leading-order CH equation (dashed line) *vs.* extended CH equation (dotted line).

Figure 3 shows the absolute plateau values $|\rho_{\min}|$ and ρ_{\max} as a function of ε —the distance from the phase separation onset. The bifurcation to active phase separation is supercritical in this case: starting at $\varepsilon_c = 0$, the plateau values increase monotonically. Considering only the leading-order approximation (dashed line), we again find the system to be symmetric for all values of ε . In reality, the full system (solid lines) becomes more and more asymmetric for increasing ε . This is very accurately represented by the higher-order approximation (dotted lines). It only starts to deviate from the full model further from threshold. Importantly though, close to the onset of mobility-induced phase separation, as ε becomes smaller, the full model becomes more and more symmetric. All three models then are in increasingly good agreement. This again underlines the fact that the classic CH model is the simplest generic model for active phase separation. All active phase separation phenomena of this type can be reduced to the CH model close to onset. Higher-order nonlinearities only come into play further from threshold.

If we allow $r_1 \neq 0$, phase separation is asymmetric even at leading order. This can be seen in fig. 4 which shows the steady-state profiles for the full ABP model, leading-order CH and extended CH at $\varepsilon = 0.02$. Here, the leading-order CH equation (dashed line) results in an asymmetric solution. However, the predicted plateau values deviate about 20% from the full system (outlines of shaded grey region). The extended CH model, meanwhile, is still able to accurately predict the full system solution with a deviation of less than 6%.

Looking at the plateau values as a function of ε (see fig. 5) solidifies this impression: the leading-order CH model gives a good qualitative representation of the full system. Going to the extended CH model provides very good quantitative agreement with the full model even for larger values of ε . As discussed earlier in sect. 5.3, the onset of phase separation (*i.e.* the ε -value at which the homogeneous solution $|\rho_{\min}| = \rho_{\max} = 0$ becomes unstable) is shifted to finite values of ε in the case $r_1 \neq 0$.

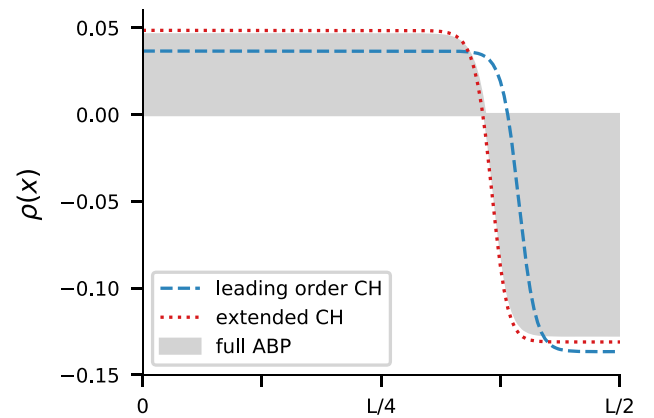


Fig. 4. Comparison of the steady-state profiles for $\bar{\rho} = 0.8$ at $\varepsilon = 0.02$: full ABP model (shaded grey) *vs.* leading-order CH equation (dashed line) *vs.* extended CH equation (dotted line).

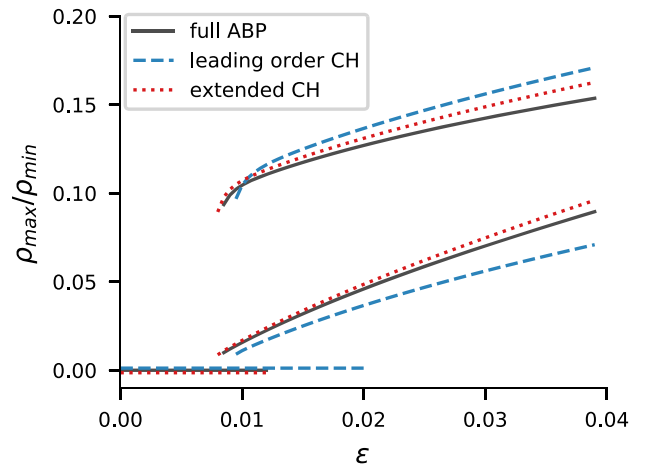


Fig. 5. Comparison of plateau values $|\rho_{\min}|$ and ρ_{\max} as a function of the control parameter ε for $\bar{\rho} = 0.8$ (or $r_1 = 1/15$): full ABP model (solid line) *vs.* leading-order CH equation (dashed line) *vs.* extended CH equation (dotted line).

For the given system parameters, the threshold for the full system is shifted to $\varepsilon_c \approx 0.013$. The leading-order CH model significantly overestimates this threshold, shifting to $\varepsilon_c \approx 0.02$. The extended CH model only very slightly underestimates the real threshold. Note that above this threshold, the plateau values immediately jump to finite values. Thus, the transition from the homogeneous to the phase-separated state is no longer smooth. On the other hand, fig. 5 also shows that the branches of finite density plateau values extend below the thresholds noted above. This creates a range of bistability—a range of control parameter values in which both the homogeneous and the phase-separated state are stable simultaneously. All of these characteristics indicate that bifurcation from the homogeneous state to active phase separation is now subcritical.

7 Conclusion

Starting from the mean-field model for active Brownian particles in refs. [23, 30], we applied a perturbative approach introduced in ref. [16]. We showed that the non-equilibrium phenomenon motility-induced phase separation (MIPS) is described near its onset at leading order by the Cahn-Hilliard (CH) model [34, 35, 38, 39]. This is in agreement with a recent observation that the CH model describes the system-spanning behavior of a number of very different demixing phenomena in active and living systems far from thermal equilibrium [16]. The results in this work show that MIPS also belongs to this class of active phase separation. Thus, even though the CH model was originally introduced to describe phase separation of binary mixtures in thermal equilibrium, our analysis shows that it is also the generic leading-order description of active phase separation —a non-equilibrium phenomenon.

We also extended the perturbative scheme introduced in ref. [16] beyond the CH model to next higher-order nonlinearities. In this work, we used the continuum ABP model as a framework to establish this concept. The extension of our nonlinear expansion, however, can also be applied to other systems showing active phase separation (with a conserved order parameter field) such as cell polarization and clustering of chemotactically communicating cells. Having a \pm -symmetric CH model at the onset of active phase separation, we find that in general four nonlinear terms come into play at the next higher order. Two of them have the same form as contributions suggested in previous phenomenological extensions of the CH model for MIPS [4, 31, 32, 36]. These phenomenological models are thus related to the extended CH model that our perturbative scheme provides. Our approach, however, is non-phenomenological: it establishes a direct mathematical link between the coefficients of the extended CH model and the full mean-field description of ABPs (or any other basic model of active phase separation in general). It shows in addition, that the coefficients of the additional contributions in the extended CH model are in general not independent of each other, as often assumed in phenomenological approaches. Furthermore, these coefficients are system-specific and cannot be removed by rescaling as in the case of the leading-order CH model. It is also important to reiterate that these nonlinear extensions become negligible when approaching the onset of MIPS or other examples of active phase separation. Therefore, the leading-order CH model already covers the universal behavior of MIPS (as a non-equilibrium phenomenon) near its onset. Higher-order nonlinearities mainly improve accuracy and become relevant further from threshold. They should thus not be seen as the key to expand the CH model to non-equilibrium systems.

Within the systematics of the pattern formation theory, the work we introduced in ref. [16] and extended here is a weakly nonlinear analysis and reduction method for active phase separation described by conserved order parameter fields. It can be seen as a yet unexplored counterpart to the weakly nonlinear analysis of (non-oscillatory)

spatially periodic patterns with unconserved order parameter fields and its numerous applications [29, 37, 40–42].

Our generic approach for active phase separation opens up several pathways for further system-spanning investigations. Coarsening dynamics in large systems, and especially the role of higher nonlinearities in this context, have already been of particular interest to the scientific community (see, *e.g.*, ref. [32] for MIPS). Other active phase separation phenomena such as cell polarization, on the other hand, take place in very small systems where coarsening plays a less important role [43]. For these systems, spatial constraints may significantly influence the behavior instead. Studies on spatially periodic patterns have already shown that confinement may trigger various interesting generic effects (see *e.g.* [44]) and even induce patterns in small systems which are unstable in larger systems (see [45] and references therein). On the basis of our results, it will be interesting to investigate finite size effects on non-equilibrium phase transitions with conservation constraints.

Support by the Elite Study Program Biological Physics is gratefully acknowledged.

Author contribution statement

All authors contributed to the design of the research, to calculations, the interpretation of results and the writing of the manuscript. LR performed numerical simulations.

Availability of data and materials

The simulation datasets used in this article are available from the corresponding author on request.

Publisher's Note The EPJ Publishers remain neutral with regard to jurisdictional claims in published maps and institutional affiliations.

References

1. T. Vicsek, A. Zafeiris, *Phys. Rep.* **517**, 71 (2012).
2. A. Cavagna, I. Giardina, *Annu. Rev. Condens. Matter Phys.* **5**, 183 (2014).
3. A.A. Hyman, C.A. Weber, F. Jülicher, *Annu. Rev. Cell Dev. Biol.* **30**, 39 (2014).
4. M.E. Cates, J. Tailleur, *Annu. Rev. Condens. Matter Phys.* **6**, 219 (2015).
5. S. Zhou, A. Sokolov, O.D. Lavrentovich, I.S. Aranson, *Proc. Natl. Acad. Sci. U.S.A.* **111**, 1265 (2014).
6. C. Bechinger, R. Di Leonardo, H. Löwen, C. Reichardt, G. Volpe, G. Volpe, *Rev. Mod. Phys.* **88**, 045006 (2016).
7. Y. Shin, C.P. Brangwynne, *Science* **357**, 4382 (2017).
8. F. Jülicher, S.W. Grill, G. Salbreux, *Rep. Prog. Phys.* **81**, 076601 (2018).

9. B. Alberts, A. Johnson, J. Lewis, M. Raff, K. Roberts, P. Walter, *Molecular Biology of the Cell* (Garland Science, New York, 2002).
10. A. Jilkine, A.F. Marée, L. Edelstein-Keshet, *Bull. Math. Biol.* **69**, 1943 (2007).
11. M. Otsuji, S. Ishihara, C. Co, K. Kaibuchi, A. Mochizuki, S. Kuroda, *PLoS Comput. Biol.* **3**, e108 (2007).
12. N.W. Goehring, S.W. Grill, *Trends Cell Biol.* **23**, 72 (2013).
13. P.K. Trong, E.M. Nicola, N.W. Goehring, K.V. Kumar, S.W. Grill, *New J. Phys.* **16**, 065009 (2014).
14. S. Alonso, M. Bär, *Phys. Biol.* **7**, 046012 (2010).
15. N.W. Goehring, P.K. Trong, J.S. Bois, D. Chowdhury, E.M. Nicola, A.A. Hyman, S.W. Grill, *Science* **334**, 1137 (2011).
16. F. Bergmann, L. Rapp, W. Zimmermann, *Phys. Rev. E* **98**, 020603(R) (2018).
17. M.J. Tindall, P.K. Maini, S.L. Porter, J.P. Armitage, *Bull. Math. Biol.* **70**, 1570 (2008).
18. T. Hillen, K.J. Painter, *J. Math. Biol.* **58**, 183 (2009).
19. M. Meyer, L. Schimansky-Geier, P. Romanczuk, *Phys. Rev. E* **89**, 022711 (2014).
20. B. Liebchen, D. Marenduzzo, I. Pagonabarraga, M.E. Cates, *Phys. Rev. Lett.* **115**, 258301 (2015).
21. I. Theurkauff, C. Cottin-Bizonne, J. Palacci, C. Ybert, L. Bocquet, *Phys. Rev. Lett.* **108**, 268303 (2012).
22. J. Palacci, S. Sacanna, A.P. Steinberg, D.J. Pine, P.M. Chaikin, *Science* **339**, 936 (2013).
23. I. Buttinoni, J. Bialké, F. Kümmel, H. Löwen, C. Bechinger, T. Speck, *Phys. Rev. Lett.* **110**, 238301 (2013).
24. Y. Fily, M.C. Marchetti, *Phys. Rev. Lett.* **108**, 235702 (2012).
25. J. Stenhammer, A. Tiribocchi, R.J. Allen, D. Marenduzzo, M.E. Cates, *Phys. Rev. Lett.* **111**, 145702 (2013).
26. G.S. Redner, M.F. Hagan, A. Baskaran, *Phys. Rev. Lett.* **110**, 055701 (2013).
27. T. Speck, J. Bialké, A.M. Menzel, H. Löwen, *Phys. Rev. Lett.* **112**, 218304 (2014).
28. Q.-X. Liu, A. Doelman, V. Rottschäfer, M. de Jager, P.M. Herman, M. Rietkerk, J. van de Koppel, *Proc. Natl. Acad. Sci. U.S.A.* **110**, 11905 (2013).
29. M.C. Cross, P.C. Hohenberg, *Rev. Mod. Phys.* **65**, 851 (1993).
30. T. Speck, A.M. Menzel, J. Bialke, H. Löwen, *J. Chem. Phys.* **142**, 224109 (2015).
31. R. Wittkowski, A. Tiribocchi, J. Stenhammer, R.J. Allen, D. Marenduzzo, M.E. Cates, *Nat. Commun.* **5**, 4351 (2014).
32. E. Tjhung, C. Nardini, M.E. Cates, *Phys. Rev. X* **8**, 031080 (2018).
33. J. Tailleur, M.E. Cates, *Phys. Rev. Lett.* **100**, 218103 (2008).
34. A.J. Bray, *Adv. Phys.* **43**, 357 (1994).
35. R.C. Desai, R. Kapral, *Dynamics of Self-Organized and Self-Assembled Structures* (Cambridge University Press, Cambridge, 2009).
36. A.P. Solon, J. Stenhammer, M.E. Cates, Y. Kafri, J. Tailleur, *Phys. Rev. E* **97**, 020602(R) (2018).
37. M.C. Cross, H. Greenside, *Pattern Formation and Dynamics in Nonequilibrium Systems* (Cambridge University Press, Cambridge, 2009).
38. J.W. Cahn, J.E. Hilliard, *J. Chem. Phys.* **28**, 258 (1958).
39. J.W. Cahn, *Acta Metall.* **9**, 795 (1961).
40. L.M. Pismen, *Patterns and Interfaces in Dissipative Dynamics* (Springer, Berlin, 2006).
41. E. Meron, *Nonlinear Physics of Ecosystems* (CRC Press, Boca Raton, Florida, 2015).
42. C. Misbah, *Complex Dynamics and Morphogenesis* (Springer, Berlin, Germany, 2016).
43. L. Edelstein-Keshet, W.R. Holmes, M. Zajac, M. Dutot, *Philos. Trans. R. Soc. B* **368**, 20130003 (2013).
44. L. Rapp, F. Bergmann, W. Zimmermann, *EPL* **113**, 28006 (2016).
45. F. Bergmann, L. Rapp, W. Zimmermann, *New J. Phys.* **20**, 072001 (2018).

Spatially periodic patterns succeed active phase separation

Lisa Rapp and Walter Zimmermann

Spatially periodic patterns succeed active phase separation

LISA RAPP, WALTER ZIMMERMANN

Theoretische Physik I, Universität Bayreuth, 95440 Bayreuth, Germany

PACS 89.75.Kd – Pattern Formation

Abstract – We investigate a model equation for a conserved order-parameter field that covers as special cases the conserved Swift-Hohenberg model and the extended Cahn-Hilliard model for active phase separation. This model has a primary bifurcation from a homogeneous state to large-scale phase separation. We show here that further from the onset of phase separation, there is a secondary bifurcation which triggers a transition to spatially periodic patterns. This is a first example of pattern formation phenomena which can occur beyond active phase separation. We present phase diagram, bistability between phase separation and periodic patterns,...

Introduction. – There is a great variety of patterns occurring in the animate and inanimate world [1–5] (etc.). Many of these spatially periodic patterns are described by unconserved order parameter fields. On the other hand there is a variety of demixing phenomena in active, non-equilibrium systems which may be described by conserved order parameter fields. Examples include cell polarization [6–17], chemotactically communicating cells [18–22], self-propelled particles [23–26], or active matter models [27]. We recently named this class active phase separation [28].

There are, however, also systems described by a conserved order parameter field that show spatially periodic patterns [29]. We know from active phase separation systems that the range of unstable wavenumbers increases with the distance from phase separation onset. Therefore, one may raise the question, whether these increasing possibilities for instabilities eventually give rise to a secondary bifurcation from a phase-separated state to a spatially periodic pattern.

Model. – To investigate this question we suggest a model that covers on the one hand the conserved Swift-Hohenberg model [29, 30] as a limiting case, as well as the extended Cahn-Hilliard model for active phase separation [31]. We thus suggest and investigate the following non-linear equation for a real conserved order-parameter field $\psi(x, t)$:

$$\partial_t \psi = -\partial_x^2 [\varepsilon \psi + D_4 \partial_x^2 \psi - D_6 \partial_x^4 \psi - \psi^3] - \partial_x^2 [\varepsilon \beta_1 \psi^2 + \beta_2 \psi \partial_x^2 \psi + \beta_3 (\partial_x \psi)^2 + \beta_4 \psi^4], \quad (1)$$

For $\beta_i = 0$ ($i = 1, 2, 3, 4$), $D_6 = 1$, $D_4 = -2$ and $\varepsilon \rightarrow r - 1$ this model reduces to the $\pm\psi$ -symmetric conserved Swift-

Hohenberg model suggested in Ref. [29]. For $D_6 = 0$ and $D_4 = 1$ the model equation (1) reduces to the extended Cahn-Hilliard model for active phase separation described in Ref. [31]. The four contributions including the parameters β_i ($i = 1, 2, 3, 4$) are the generic next higher order corrections to the Cahn-Hilliard model [31] and cover the contribution of the so-called active model B [32] and active model B+ [33]. Using in this case the scaling $X = \sqrt{\varepsilon}x$ and $\psi = \sqrt{\varepsilon}\varphi$ the parameters β_i become multiplied by the factor $\sqrt{\varepsilon}$ [31]. This shows that the contributions including the coefficients β_i ($i = 1, 2, 3, 4$) are next higher order corrections to the leading order Cahn-Hilliard model for active phase separation and vanish by approaching the threshold, i.e. $\varepsilon \rightarrow 0$.

Phase separation solutions. – In the following, we only consider one of the symmetry-breaking higher nonlinearities and thus set $\beta_1 = \beta_3 = \beta_4 = 0$. This simplifies Eq. (1) to

$$\partial_t \psi = -\partial_x^2 [\varepsilon \psi + D_4 \partial_x^2 \psi - D_6 \partial_x^4 \psi - \psi^3 + \beta_2 \psi \partial_x^2 \psi]. \quad (2)$$

We assume all parameters to be positive and real-valued. In the special case $D_6 = \beta_2 = 0$ this equation reduces to the classic Cahn-Hilliard model where a stationary phase separation solution is given by

$$\psi(x) = \sqrt{\varepsilon} \tanh \left(\sqrt{\frac{\varepsilon}{2D_4}} x \right). \quad (3)$$

We assume that this is still a reasonable approximation for $D_6, \beta_2 \neq 0$. If we consider a long system with only a single domain wall, there are large parts of the system with nearly constant solutions $\psi_0 = \pm\sqrt{\varepsilon}$ (see also Fig. 1a). We

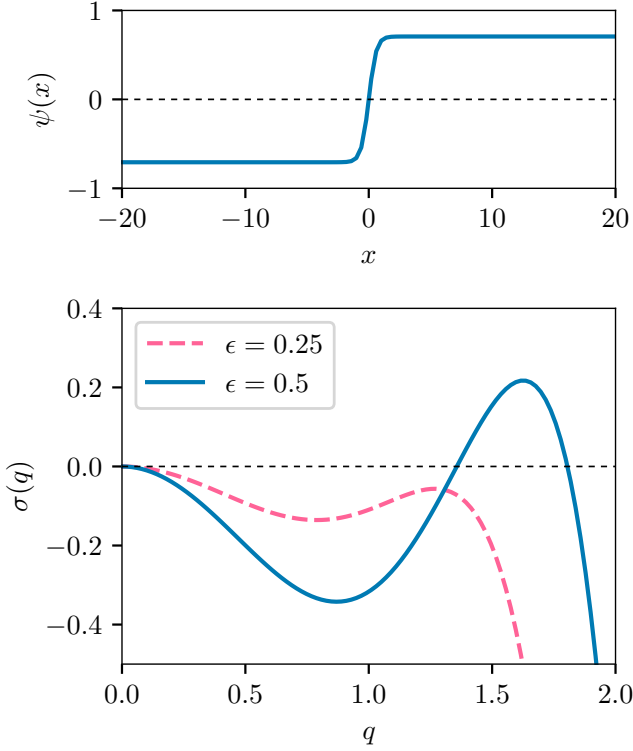


Fig. 1: a) Typical stationary phase separation solution as given by Eq. (3). b) Growth rate dispersion relation for perturbations of homogeneous solutions $\psi_0 = \pm\sqrt{\varepsilon}$ in Eq. (2). Parameters: $D_4 = 0.15$, $D_6 = 1/6$, $\beta_2 = \sqrt{2}$.

analyze the stability of these constant regions with respect to small perturbations $\psi_1(x, t)$ by choosing the ansatz

$$\psi = \psi_0 + \psi_1, \quad (4)$$

which we plug into Eq. (2) and linearize with respect to ψ_1 :

$$\partial_t \psi_1 = -\partial_x^2 [-2\varepsilon\psi_1 + (D_4 \pm \beta_2\sqrt{\varepsilon}) \partial_x^2 \psi_1 - D_6 \partial_x^4 \psi]. \quad (5)$$

Using the ansatz $\psi_1 = F \exp(\sigma t + iqx)$, we find the dispersion relation

$$\sigma = -2\varepsilon q^2 - (D_4 \pm \beta_2\sqrt{\varepsilon}) q^4 - D_6 q^6. \quad (6)$$

In the case of the negative sign, the contribution $\propto q^4$ can become positive for sufficiently large β_2 (see Fig. 1b). In addition to $q = 0$, the dispersion relation has a maximum at

$$q_{max}^2 = \frac{1}{3D_6} \left[\beta_2\sqrt{\varepsilon} - D_4 + \sqrt{(\beta_2\varepsilon - D_4)^2 - 6D_6\varepsilon} \right] \quad (7)$$

if $\beta_2\sqrt{\varepsilon} > D_4$. The growth rate $\sigma(q_{max})$ first becomes positive at the critical control parameter value given by

$$\varepsilon_q = \frac{D_4^2}{(2\sqrt{2D_6} - \beta_2)^2}. \quad (8)$$

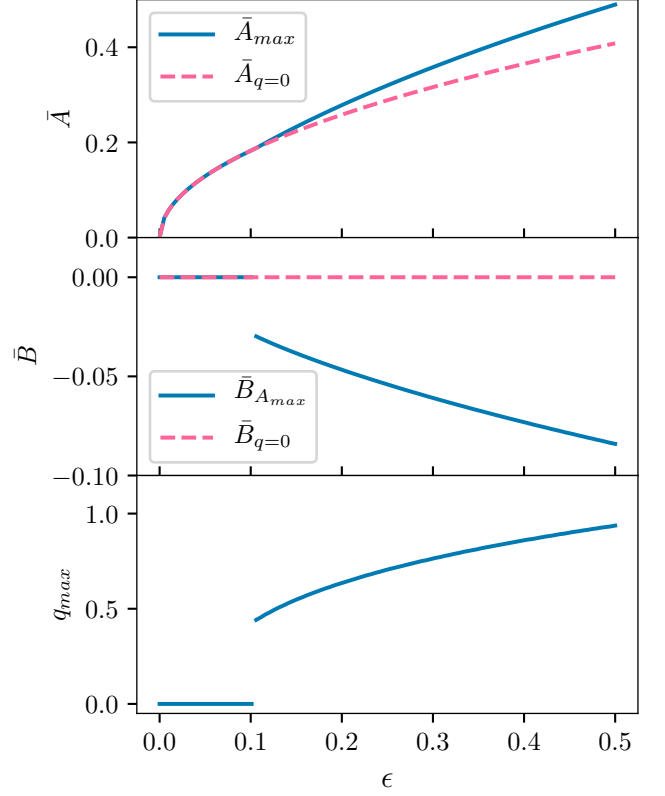


Fig. 2: Amplitudes of the two-mode solution as a function of ε . a) Amplitudes \bar{A} for $q = 0$ and the wavenumber that results in the largest value for \bar{A} . b) Corresponding values of the amplitude \bar{B} . c) Wavenumber resulting in the largest amplitude \bar{A} . Parameters: $D_4 = 0.15$, $D_6 = 1/6$, $\beta_2 = \sqrt{2}$.

Thus, there is an upper limit of the control parameter above which constant solutions become unstable. By extension this should also be a good approximation for phase-separated solutions which consist of large regions of constant concentration.

Two-periodic solutions. – From the shape of the dispersion relation in Eq. (6), we can predict a transition from the phase-separated state to spatially periodic patterns. Due to the broken $\pm\psi$ -symmetry in the system, a typical periodic pattern is a two-mode solution of the form

$$\psi = A(t)e^{iqx} + A^*(t)e^{-iqx} + B(t)e^{2iqx} + B^*(t)e^{-2iqx}. \quad (9)$$

Projecting onto the modes $\propto \exp(iqx)$ and $\propto \exp(2iqx)$, we find coupled equations for the amplitudes A and B :

$$\dot{A} = q^2 \left[(\varepsilon - D_4 q^2 - D_6 q^4 - 3|A|^2 - 6|B|^2) A - 5\beta_2 q^2 A^* B \right], \quad (10)$$

$$\dot{B} = 4q^2 \left[(\varepsilon - 4D_4 q^2 - 16D_6 q^4 - 3|B|^2 - 6|A|^2) B - \beta_2 q^2 A^2 \right]. \quad (11)$$

Assuming stationary solutions, we set: $A = \bar{A}$ and $B = \bar{B} \exp(i\phi)$. The imaginary parts of Eqs. (10) and (11) are

solved by $\sin \phi = 0$, i.e. $\phi = 0, \pi, 2\pi, \dots$, from which follows $\cos \phi = \pm 1$. The real parts lead to the coupled equations

$$0 = \mathcal{L}_A - 3\bar{A}^2 - 6\bar{B}^2 \mp 5\beta_2 q^2 \bar{B}, \quad (12)$$

$$0 = \mathcal{L}_B \bar{B} - 3\bar{B}^3 - 6\bar{A}^2 \bar{B} \mp \beta_2 q^2 \bar{A}^2, \quad (13)$$

where

$$\mathcal{L}_A = \varepsilon - D_4 q^2 - D_6 q^4, \quad (14)$$

$$\mathcal{L}_B = \varepsilon - 4D_4 q^2 - 16D_6 q^4. \quad (15)$$

From Eq. (12), we find

$$\bar{A}^2 = \frac{1}{3} [\mathcal{L}_A - 6\bar{B}^2 \mp 5\beta_2 q^2 \bar{B}]. \quad (16)$$

Substituting this into Eq. (13), we find the following polynomial for the amplitude \bar{B} :

$$0 = 9\bar{B}^3 \pm 12\beta_2 q^2 \bar{B}^2 \mp \frac{1}{3}\beta_2 q^2 \mathcal{L}_A + \left(\mathcal{L}_B - 2\mathcal{L}_A + \frac{5}{3}\beta_2^2 q^4 \right) \bar{B} \quad (17)$$

The polynomial can be solved numerically. From the up to three solutions, only real-valued solutions are relevant. Additionally, the amplitude \bar{A} as calculated from \bar{B} via Eq. (16) has to be real-valued as well. Note that in addition to the system parameters, the solutions also depend on the wavenumber q .

The amplitudes of two-mode periodic solutions as a function of the control parameter ε are shown in Fig. 2. The other system parameters in this case are fixed. They were calculated numerically from Eqs. (17) and (16) for different values of the wavenumber q . Figure 2a shows the largest amplitude A_{max} (maximized as a function of q) in comparison to the amplitude of a homogeneous perturbation ($q = 0$). The corresponding amplitude \bar{B} is shown in Fig. 2b. Figure 2c shows the wavenumber q that results in the largest amplitude A_{max} . For small values of the control parameter ε , the solution with the largest amplitude is homogeneous (i.e. $q = 0$). At a critical value ε_c , however, a periodic solution with a finite wavenumber q results in a higher stationary amplitude. This periodic solution has a finite higher harmonic contribution \bar{B} . This, again, indicates a transition from a phase-separated state to a spatially periodic pattern.

The predicted transition to spatially periodic patterns also depends on the other system parameters. Phase diagrams of the expected solutions in the ε - β_2 -, as well as ε - D_4 phase space are shown in Figure 3a and b, respectively. The color code in these images shows whether the largest amplitude \bar{A} is given for $q = 0$ or a finite wavenumber - representing homogeneous or periodic solutions, respectively. The predicted secondary bifurcation to periodic solutions is shifted to larger values of ε for smaller values of β_2 , i.e. for a weaker symmetry-breaking nonlinearity, or for larger values of D_4 . In fact, no transition is expected if β_2 is too small or D_4 too large. This is in accordance with the condition $\beta_2 \varepsilon > D_4$ for a growth rate dispersion with a maximum at finite wavenumber [see Eq. (7)].

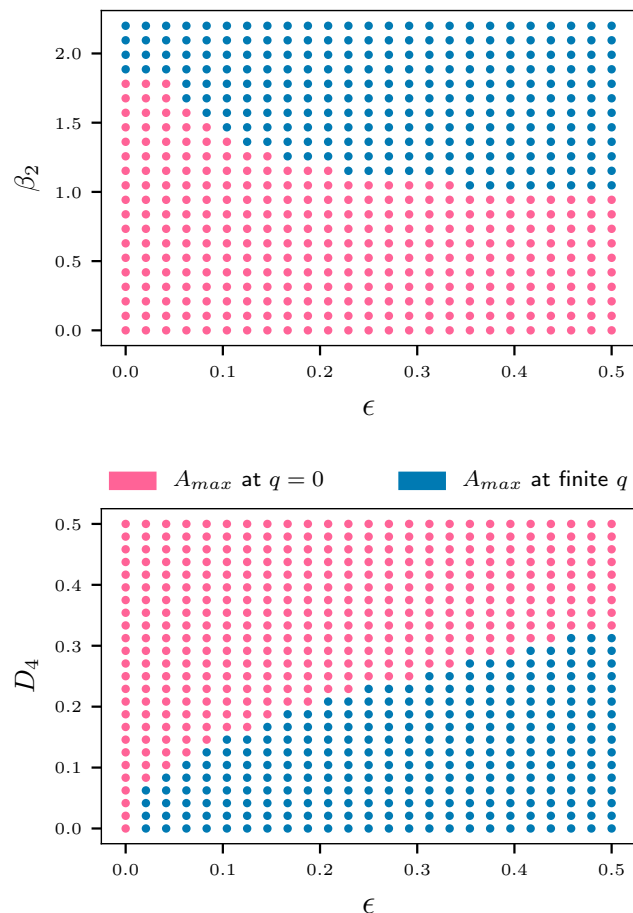


Fig. 3: Phase diagrams for periodic solutions in the a) ε - β_2 -plane and the b) ε - D_4 -plane, respectively. Pink dots indicate parameter combinations where the homogeneous solution ($q = 0$) results in the largest amplitude A , while a periodic solution with finite wavenumber q has a higher amplitude for blue dots.

Numerical simulations. – Simulations of Eq. (2) confirm the predictions from linear stability analysis. For small values of the control parameter ε , we find a phase-separated solution similar as given in Eq. (3). With increasing ε , the solution starts to deviate from this classic kink solution. Due to the higher order symmetry-breaking nonlinearity, characteristic overshoots start to appear (see Fig. 4, left). If ε is further increased, the phase-separated solution finally becomes unstable and changes into a spatially periodic solution (see Fig. 4).

Figure 5 shows this transition from a phase-separated state to periodic solutions as a function of ε : Starting from small ε we first find phase-separated solutions with increasing plateau values as a function of ε . The transition to spatially periodic solutions takes place at about $\varepsilon \approx 0.065$. The periodic pattern stays stable for increasing ε with increasing amplitude. If ε is decreased starting from larger values, the spatially periodic state stays stable down to values of $\varepsilon \approx 0.05$, before the solution changes to the

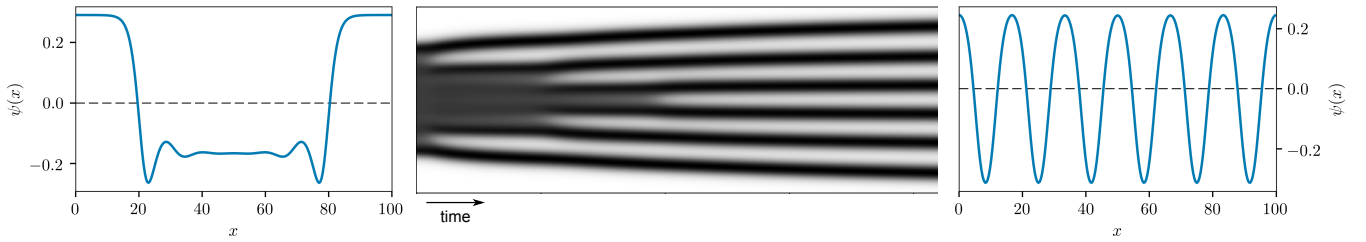


Fig. 4: Transition from a phase-separated solution to a periodic pattern as a space-time plot (center). Profiles of the respective solutions (left: phase separation, right: periodic pattern). Parameters: $D_4 = 0.15$, $D_6 = 1/6$, $\beta_2 = \sqrt{2}$. (LR: ϵ angeben)

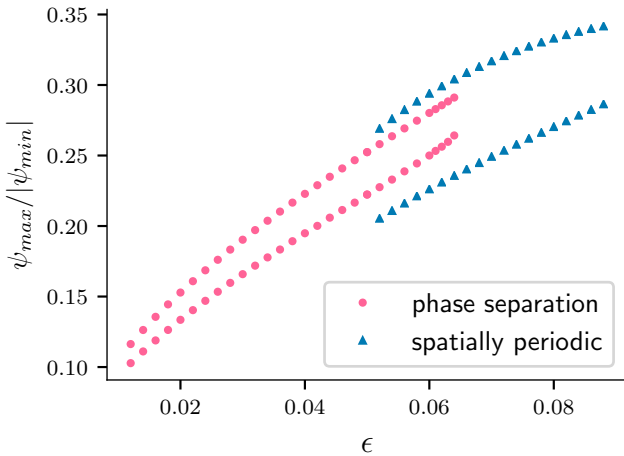


Fig. 5: Maximum value ψ_{max} and magnitude of minimal value $|\psi_{min}|$ of steady state solutions in simulations of Eq. (2) as a function of ϵ . Transition from phase separation to periodic solutions at around $\epsilon \approx 0.065$. Hysteresis when decreasing ϵ starting from periodic solutions: Transition back to phase separation around $\epsilon \approx 0.05$.

phase-separated state again. Thus, there is a bistability region in the range $0.05 \lesssim \epsilon \lesssim 0.065$ where both the phase-separated and the spatially periodic solution are stable. In fact, in the bistability parameter region, hybrid solutions with local coexistence of the two solution types are stable as well (see Fig. 6).

Conclusions. – In this work, we explored a possible pattern formation scenario happening beyond active phase separation. We studied a generic model that includes both the conserved Swift-Hohenberg model (known for spatially periodic patterns) and the extended Cahn-Hilliard model for active phase separation. Analytical considerations predict and numerical simulations confirm that in this model, phase-separated states can transition to spatially periodic patterns in a secondary bifurcation further from the onset of active phase separation.

Exploring the phase space for this model, we found that the secondary instability to periodic patterns appears for sufficiently low interfacial energy and sufficiently strongly broken up-down-symmetry via a higher nonlinearity. We

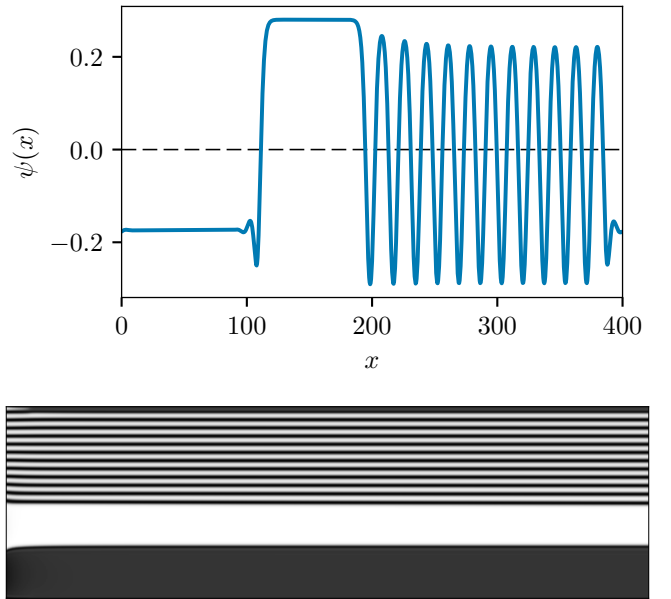


Fig. 6: Hybrid solution of phase separation and periodic pattern in the bistability region. a) Profile of the solution $\psi(x, t)$, b) Time development of the solution depicted in a). Parameters: $D_4 = 0.15$, $D_6 = 1/6$, $\beta_2 = \sqrt{2}$, $\epsilon = 0.06$.

also found a region of bistability between phase-separated states and spatially periodic solutions. This also allows for hybrid states with local coexistence between the two solution types.

The work we present here is a first proof for the generic existence of spatially periodic patterns in active phase separation systems. This is especially interesting since periodic patterns have been observed in different potential active phase separation systems. Among these are self-propelled particles showing motility-induced phase separation [33], chemorepulsive active colloids [34], active particles with long-range interactions [35] or binary mixtures of active and passive particles [36]. This work should thus be seen as a first step to further explore periodic patterns in active matter systems with conserved order parameters. Similar to active phase separation as a nonequilibrium parallel to the classic equilibrium phase separation, there could be a generic class of active

microphase separation which can be explored in more detail in the future.

Acknowledgments. We gratefully acknowledge fruitful discussions with T. Speck.

REFERENCES

- [1] BALL P., *The Self-Made Tapestry: Pattern Formation in Nature* (Oxford Univ. Press, Oxford) 2001.
- [2] CROSS M. C. and HOHENBERG P. C., *Rev. Mod. Phys.*, **65** (1993) 851.
- [3] CROSS M. C. and GREENSIDE H., *Pattern Formation and Dynamics in Nonequilibrium Systems* (Cambridge Univ. Press, Cambridge) 2009.
- [4] ARANSON I. and KRAMER L., *Rev. Mod. Phys.*, **74** (2002) 99.
- [5] KONDO S. and MIURA T., *Science*, **329** (2010) 1616.
- [6] JOHNSTON D. S. and AHRINGER J., *Cell*, **141** (2010) 757.
- [7] THOMPSON B. J., *Development*, **140** (2013) 13.
- [8] A. JILKINE AND A. F. M. MARÉE AND L. EDELSTEIN-KESHET, *Bull. Math. Biol.*, **69** (2007) 1943.
- [9] OTSUJI M., ISHIHARA S., CO C., KAIBUCHI K., MOCHIZUKI A. and KURODA S., *PLoS Comp. Biol.*, **3** (2007) e108.
- [10] MORI Y., JILKINE A. and EDELSTEIN-KESHET L., *Biophys. J.*, **94** (2008) 3684.
- [11] GORYACHEV A. B. and POKHILKO A. V., *FEBS Lett.*, **582** (2008) 1437.
- [12] GOEHRING N. W. and GRILL S. W., *Trends Cell Biol.*, **23** (2013) 72.
- [13] JILKINE A. and EDELSTEIN-KESHET L., *PLoS Comput. Biol.*, **7** (2011) e1001121.
- [14] RUBINSTEIN B., SLAUGHTER B. D. and LI R., *Phys. Biol.*, **9** (2012) 045006.
- [15] TRONG P. K., NICOLA E. M., GOEHRING N. W., KUMAR K. V. and GRILL S. W., *New J. Phys.*, **16** (2014) 065009.
- [16] ALONSO S. and BÄR M., *Phys. Biol.*, **7** (2010) 046012.
- [17] GOEHRING N. W., TRONG P. K., BOIS J. S., CHOWDURY D., NICOLA E. M., HYMAN A. A. and GRILL S. W., *Science*, **334** (2011) 1137.
- [18] KELLER E. F. and SEGEL L. A., *J. Theor. Biol.*, **26** (1970) 399.
- [19] KELLER E. F. and SEGEL L. A., *J. Theor. Biol.*, **30** (1971) 225.
- [20] TINDALL M. J., MAINI P. K., PORTER S. L. and ARMITAGE J. P., *Bull. Math. Biol.*, **70** (2008) 1570.
- [21] HILLEN T. and PAINTER K. J., *J. Math. Biol.*, **58** (2009) 183.
- [22] MEYER M., SCHIMANSKY-GEIER L. and ROMANCZUK P., *Phys. Rev. E*, **89** (2014) 022711.
- [23] PALACCI J., SACANNA S., STEINBERG A. P., PINE D. J. and CHAIKIN P. M., *Science*, **339** (2013) 936.
- [24] BIALKÉ J., LÖWEN H. and SPECK T., *EPL*, **103** (2013) 30008.
- [25] STENHAMMER J., TIRIBOCCHI A., ALLEN R. J., MAREN-
DUZZO D. and CATES M. E., *Phys. Rev. Lett.*, **111** (2013) 145702.
- [26] SPECK T., BIALKÉ J., MENZEL A. M. and LÖWEN H., *Phys. Rev. Lett.*, **112** (2014) 218304.
- [27] BOIS J. S., JÜLICHER F. and GRILL S. W., *Phys. Rev. Lett.*, **106** (2011) 028103.
- [28] BERGMANN F., RAPP L. and ZIMMERMANN W., *Phys. Rev. E*, **98** (2018) 072001(R).
- [29] MATTHEWS P. C. and COX S. M., *Nonlinearity*, **13** (2000) 1293.
- [30] KNOBLOCH E., *Phys. Rev. A*, **40** (1989) 1549
- [31] RAPP L. and BERGMANN F. and ZIMMERMANN W., *arXiv:1901.03203*, (2019) .
- [32] WITTKOWSKI R., TIRIBOCCHI A., STENHAMMAR J., ALLEN R., MAREN-
DUZZO D. and CATES M. E., *Nat. Comm.*, **5** (2013) 4351.
- [33] TJHUNG E., NARDINI C. and CATES M.E., *Phys. Rev. X*, **8** (2018) 031080.
- [34] LIEBCHEN B., MAREN-
DUZZO D., PAGONABARRAGA I. and CATES M.E., *Phys. Rev. Lett.*, **115** (2015) 258301.
- [35] TUNG C., HARDER J., VALERIANI C. and CACCIUTO A., *Soft Matter*, **12** (2016) 555.
- [36] REICHHARDT C. and REICHHARDT C.J.O., *J. Chem. Phys.*, **150** (2019) 064905.

Acknowledgements

First and foremost, I thank my supervisor Prof. Dr. Walter Zimmermann for giving me the opportunity to work in his group, for his research suggestions, guidance and the opportunities to present my work at international conferences and workshops. I especially appreciate the fact that he allowed us to have passionate discussions about our research and beyond.

Many thanks to my collaborator and good friend Fabian Bergmann. He has been a huge part of this journey throughout my studies up to this doctorate and I am thankful that we got to walk this road together.

I thank the whole group of Theoretical Physics I for creating a fun work environment. I am especially indebted to Markus Hilt for his technical support (and for keeping everyone up-to-date on the latest gossip and international breaking news).

I am deeply grateful for the love and support of my family.

And lastly, thank you to my Bayreuth friends (including those who have already left town). I cannot wait to see what the future holds for all of us and hope we will be in each others lives for many years to come.

Take it easy, Bayreuth. It has been totally awesome.